STUDIES IN THE DECAY OF $Hg^{195,195m}$

A Thesis

Submitted to

the Faculty of Graduate Studies

University of Manitoba

In Partial Fulfillment

of the Requirements for the Degree

DOCTOR OF PHILOSOPHY

---

by

Morton John Canty

September 1969

ABSTRACT

An experimental study of the electron capture decay of 9.5 hour Hg^{195} and 40 hour Hg^{195m} has been carried out using sodium iodide scintillation detectors and high resolution solid state detectors operating in both singles and coincidence modes. Emphasis has been placed on the properties of the levels and isomeric transitions in the daughter nucleus Au^{195}.

The level structure of Au^{195} suggested in the recent literature is confirmed, while three new levels at 653 keV, 1250 keV and 1605 keV excitation and some 15 new gamma rays are suggested. The relative photon intensities of the new and of the previously accepted transitions have been accurately measured with four separate Ge(Li) spectrometers. On the basis of absolute K- and L- shell internal conversion coefficients as measured in a solid state spectrometer the multipolarities of 22 gamma rays ranging in energy up to 1240 keV have been assigned. Electron capture branching ratios and log ft values have been inferred from the gamma ray and conversion coefficient data. In addition to the previously accepted spins and parities of levels in Au^{195} five additional assignments have been made: 242 keV level $\frac{3}{2}^+$, 525 keV level $\frac{7}{2}^-$, 894 keV level $\frac{9}{2}^-$, 1083 keV level $\frac{3}{2}^+$, 1111 keV level $\frac{5}{2}^+$. The parities of most of the remaining levels have been fixed and narrow ranges of possible spins have been assigned to many of them.

It is shown that the lowest lying states in Au^{195} are described by the core excitation model of de-Shalit while the possibility of extending the model to levels of higher excitation is discussed.

ACKNOWLEDGEMENTS

The author wishes to express his sincere gratitude to Professor R. D. Connor for the patient supervision and enthusiastic support afforded throughout the course of this work.

Dr. P. H. Barker offered his kind and valuable assistance in getting the experimental work under way and aided in the analysis of much of the experimental data. The author had many valuable discussions with Dr. T. D. Nguyen on the interpretation of the data and Dr. Nguyen himself performed many of the theoretical calculations.

Many aspects of this work would have been impossible without the generous loan of equipment, for which the author owes his appreciation to Dr. S. K. Sen, Dr. E. Tomchuck, Mr. D. L. Sqlie and Mr. W. Teoh.

The cooperation of the cyclotron staff in the production of sources is greatfully acknowledged. Particular thanks are due to Messrs. W. H. Mulholland, P. Bonsor, R. Taylor, and G. Busby.

The author received personal support throughout his studies in the form of a studentship from the National Research Council of Canada.

The typing of the manuscript was graciously done by Mrs. Mandy Watson.

TABLE OF CONTENTS

LIST OF FIGURES

INTRODUCTION

The study of radiations from the atomic nucleus has long been a powerful tool for examining nuclear structure, being matched in importance only by nuclear reaction experiments involving charged particle accelerators and neutron fluxes from atomic piles. The observation of the discrete electromagnetic spectrum of nuclei was the first indication of a nuclear energy level structure and has enabled a systematic classification of nuclear levels as to lifetime, spin and parity. Fundamental changes in our concepts of strong and weak interactions have arisen from the study of nuclear β-disintegration, and it is safe to say that the existing models of nuclear structure can be tested most severely through the construction and analysis of nuclear decay schemes.

A revolution in the instrumentation available to the nuclear spectroscopist has occured in the last six or seven years. It has resulted from the merging of the most recent developments in fast, accurate data acquisition with the invention of high resolution solid state detectors. The full potential of such solid state detectors when used in conjunction with the digital computer is just now being realized. In this thesis several such high resolution devices are described and applied to the problem of deciphering the level structure of Au^{195} by examining the electron capture decay of Hg^{195} and Hg^{195m}. The first two chapters are concerned purely with

instrumentation. In chapter I the Ge(Li) gamma spectrometer in its singles and coincidence configurations is discussed as well as a gamma-gamma angular correlation table employing a Ge(Li) detector and three fixed NaI detectors. Chapter II concerns itself with the design and performance of a solid state internal conversion coefficient spectrometer. The experiments on Au^{195}, their results and interpretation are described in chapters III and IV.

Igal Talmi has emphasized the importance of being able to extract from the shell model its essential features--general rules which must be obeyed independently of the detailed assumptions about nucleon interactions. Thus, for example, in the extended single particle model with residual two-body forces, the fundamental idea is that the nucleons in closed shells move in a spherically symmetric potential independently of one another and that the energy degeneracies of partially filled orbitals are removed, to first order, by residual two-body interactions between the nucleons occupying unfilled shells. If one assumes an explicit form for the residual force and chooses some configuration space consisting of nucleon configurations expected to contribute to the observed level structure, then it is often not clear whether a poor agreement with experiment can be attributed to an incorrect residual force, an incorrect choice of nucleon configurations, or a failure of the model as a whole. Thus a test of the validity of the model itself should involve comparison with experiment

of only the general relations which follow from its basic assumptions. The weak coupling picture as developed by Amos de Shalit in his "core excitation" model is in this spirit. The essential assumption is that an even-even core of nucleons with a bound energy level spectrum generated by some completely unspecified internal motion, is weakly coupled to a single nucleon in its lowest available jj-coupling shell model orbital by a force which is, again, completely unspecified. The core excitation model is discussed extensively in chapter V of this thesis. The equations derived from it for comparison with the observations on Au^{195} are valid (a) if the model is a good approximation of reality and (b) if the core-particle configurations chosen are correct. We shall see that, at least for the levels of lowest excitation, Au^{195} does indeed seem to be described by this model.

CHAPTER I

GAMMA RADIATION SPECTROMETERS

(i) Ge(Li) Detectors

Lithium drifted germanium gamma ray detectors were used extensively in the experiments described in this work. Conventional pulse height analysis was employed to determine photon energies and intensities, while coincidence and directional correlation experiments aided the placing of levels and the assignment of spins and parities.

The advantages of germanium detectors over the older scintillation, diffraction, and electron conversion techniques are now well known and will not be gone into here. We shall confine the discussion to the performance of the detectors used, the methods of energy and efficiency calibration, and their behaviour in coincidence and directional correlation arrangements.

Table 1.1 lists the four Ge(Li) spectrometers involved in this study, along with their operating characteristics as observed in our laboratory.

The two Ortec detectors and the Nuclear Diodes detector employed charge sensitive preamplifiers with cooled FET first stages. (ORTEC model #116 with the Ortec detectors, and Tennelec TC135 with the Nuclear Diodes detector) The Princeton Gamma Tech detector was coupled to a conventional

TABLE 1.1 Ge(Li) DETECTORS

MANUFACTURER	ACTIVE VOLUME	WINDOW	RESOLUTION (PHOTON ENERGY)
ORTEC	0.25 cc	0.25 mm Be	0.5 keV (14.4 keV), 0.7 keV (100 keV
ORTEC	35 cc	0.5 mm Al	2.9 keV (1333)
NUCLEAR DIODES	0.5 cc	0.020" Al*	2.4 keV (662)
PRINCETON GAMMA TECH	20 cc	0.020" Al	5 keV (1333)

*Also encapsulated in 0.020" Al

field effect preamplifier supplied by Conuclear Ltd., Winnipeg. The resolutions reported in Table 1.1 were obtained using a Tennelec TC200 linear amplifier with the pulse shaping time constants recommended by the manufacturer. Cryostat vacuum was maintained in all cases by means of cryosorption pumping.

(ii) Pulse Height Analysis

The high resolution and high counting rates obtainable with the spectrometers described above require very sophisticated pulse height analysis systems. Analogue to digital converters with high linearity and a range of at least 1000 channels are indispensable. Two units were used throughout the present work:

- A Nuclear Data 160 analyzer with a 1024 channel dual ADC capable of 2-parameter analysis and a 4096 channel memory.
- A Nuclear Data 2200 analyzer with three 4096 channel ADC's interfaced to a 4096 channel memory via a digiplex unit. This instrument could be used either as a single 4096

channel analyzer or as 2 or 3 independent analyzers of smaller conversion gain.

A typical counting configuration is shown in Fig. 1.1.

(iii) Calibration

A counting set up such as that shown in Fig. 1.1 cannot of course be used to measure in an absolute sense the energies of X-rays and γ-rays. One must resort to a comparison of the pulse height distributions of the unknown radiations with those of certain standard radiations whose energies have been measured by other independent means (for example from conversion electron data or from crystal diffraction measurements). The reliability of comparison depends basically on the linearity and stability of the system as a whole, from detector to ADC, since the comparison usually involves interpolation between two or more points on an energy vs. channel number plot. Various degrees of sophistication have been employed to locate the full energy line or photopeak corresponding to a monoenergetic γ-ray in Ge(Li) spectra and energies have been reported to an accuracy of $\pm$ 0.02 keV[1]. However, if the number of radiations is large and if many of them are of low intensity, elaborate techniques become prohibitive. In the present work the desired end is to construct a decay scheme and to make some comparison with existing theories of nuclear structure. No attempt has been made to measure photon energies to better than about $\pm$0.3 keV--an accuracy adequate to these ends.

Figure 1.1

"Typical singles gamma ray spectrometer."

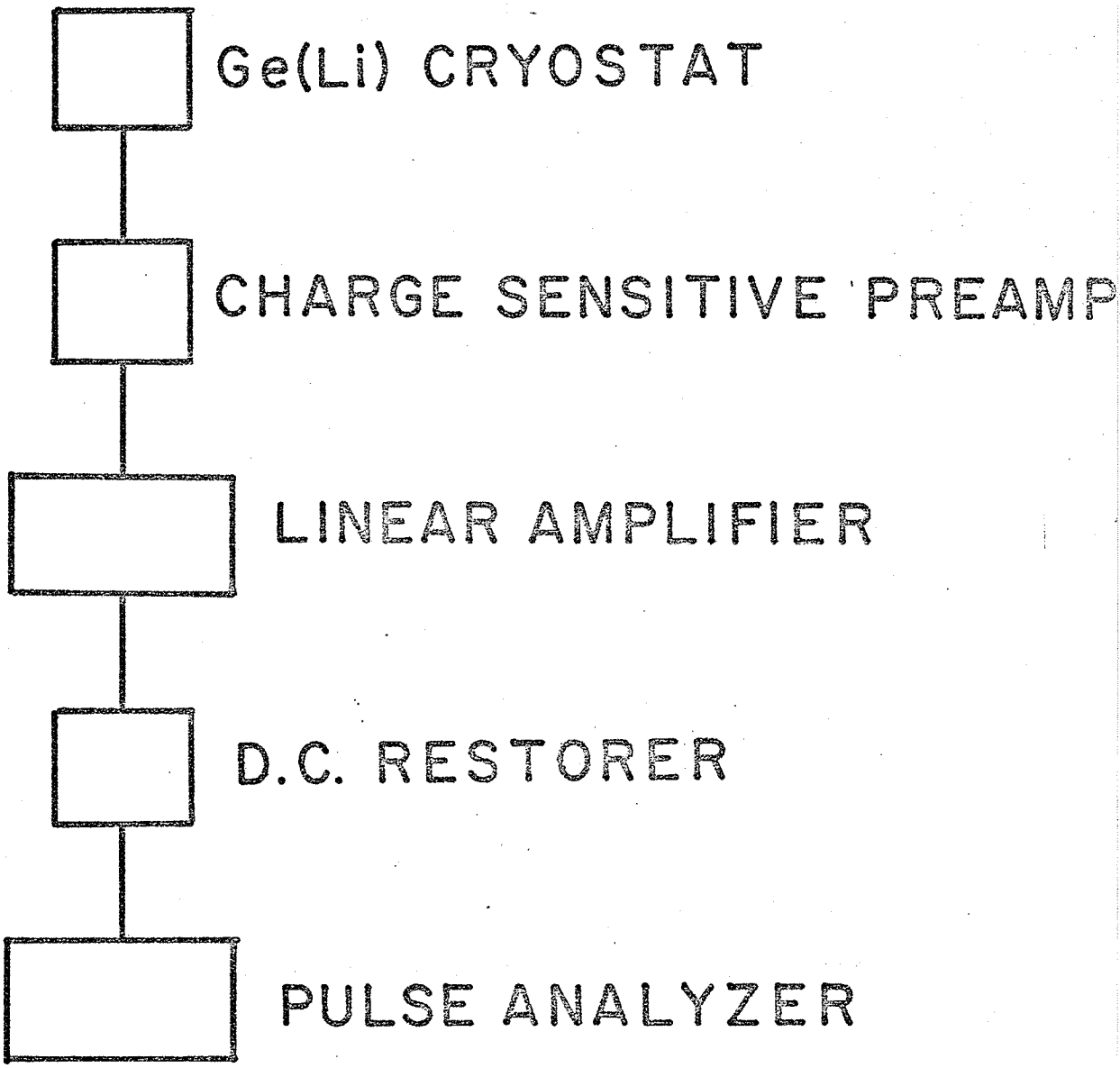
Ge(Li) CRYOSTAT
CHARGE SENSITIVE PREAMP
LINEAR AMPLIFIER
D.C. RESTORER
PULSE ANALYZER

Briefly, the technique used is that of "mixed sources". The unknown spectrum and that of several conveniently chosen standard sources are accumulated simultaneously. In this way, any gain drifts or loss of resolution due to electronics, counting rate, etc. will be shared equally by both known and unknown lines. From the observed position of the standard lines a straight line calibration and "linearity plot" can be obtained for that particular experiment. Fig. 1.2 shows a linearity plot for the Nuclear Diodes detector and ND2200 analyzer. This curve was obtained by establishing the channel numbers of the full energy peaks of various energy standards then calculating the equation of the straight line through two intermediate points. These points correspond to standard photopeaks located in regions of the display where one might expect good linearity--i.e. away from the first few hundred channels. From the equation the deviation in energy from the straight line as a function of channel number is obtained. This deviation is the quantity plotted in Fig. 1.2 vs. channel number. With the aid of the linearity plot the energies of the prominent radiations from the unknown sample can be determined. Interpolation from these strong lines can then be used in spectra of the weak lines.

Table 1.2 lists the standards used in this way and their accepted energies as tabulated by Lederer et al.[2].

The four Ge(Li) detectors were calibrated for absolute

Figure 1.2

"Gamma ray spectrometer linearity plot."

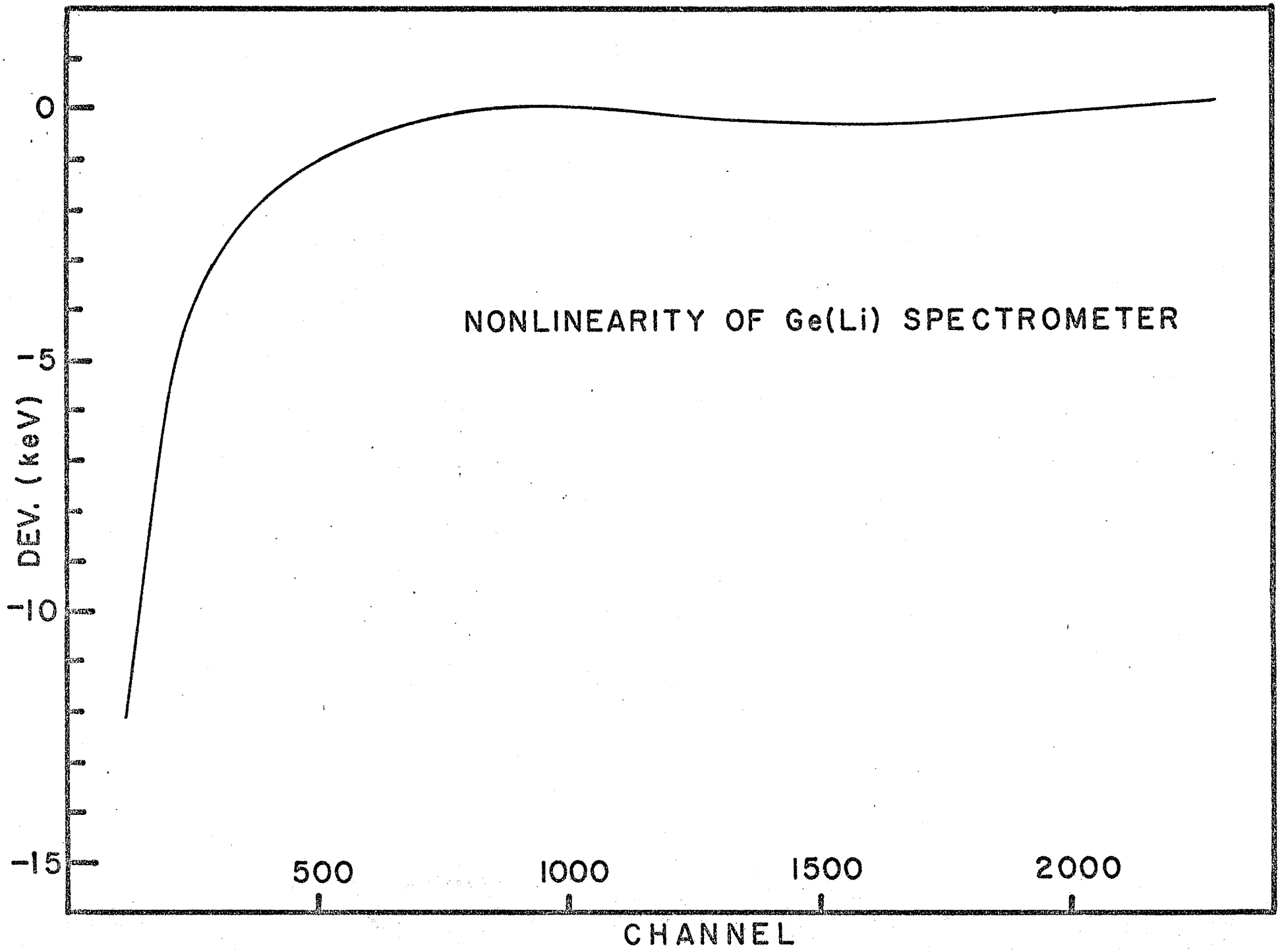
NONLINEARITY OF Ge(Li) SPECTROMETER
0
-5
-10
-15
DEV. (keV)
500
1000
1500
2000
CHANNEL

TABLE 1.2 GAMMA RAY ENERGY STANDARDS

SOURCE	ENERGY (keV)
Am^{241}	59.543
Co^{57}	121.97
	136.33
Ce^{141}	145.43
Ce^{139}	165.84
Hg^{203}	279.17
Na^{22}	511.01
	1274.53
Cs^{137}	661.60
Mn^{54}	834.85
Co^{60}	1173.23
	1332.48

photopeak efficiency with standards obtained from the International Atomic Energy Agency, Vienna. The sources used, along with the relevant intensity data are listed in Table 1.3.

A typical photopeak efficiency curve is shown in Fig. 1.3 for the Nuclear Diodes detector. The two large volume detectors exhibited similar characteristics. The smallest Ge(Li) detector (0.25 cc) was sensitive to energies down to a few keV and its efficiency curve is shown in Fig. 1.4.

(iv) A Solid State Coincidence Spectrometer

While the superiority over other techniques of solid state

TABLE 1.3 INTENSITY STANDARDS

NUCLIDE	ACTIVITY (μCUR) (1 Jan., 1969)	PHOTON ENERGY (keV)	PHOTONS/100 DISINTEGRATIONS
Am^{241}	10.35 ± 0.6%	11.9	0.8 ± 0.1
		13.9	13.5 ± 0.3
		17.8	18.4 ± 0.4
		20.8	5.0 ± 0.1
		26.3	2.5 ± 0.2
		59.5	35.9 ± 0.6
Co^{57}	11.13 ± 0.9%	14.4	9.5 ± 0.3
		122.0	85.0 ± 1.7
		136.3	11.4 ± 1.3
Hg^{203}	21.02 ± 1.0%	72.8	9.7 ± 0.5
		82.5	2.8 ± 0.2
		279.2	81.55 ± 0.15
Na^{22}	9.98 ± 0.9%	511.0	179.7 ± 0.8
		1274.6	99.95 ± 0.02
Cs^{137}	11.04 ± 1.3%	661.6	85.1 ± 0.4
Mn^{54}	11.09 ± 0.7%	834.8	100
Co^{60}	11.13 ± 0.6%	1173.2	99.74 ± 0.05
		1333.5	99.85 ± 0.03
Y^{88}	10.75 ± 0.9%	511.0	0.40 ± 0.02
		898.0	91.4 ± 0.7
		1836.1	99.4 ± 0.1
		2734.2	0.62 ± 0.04

Figure 1.3

"Absolute photopeak efficiency of Nuclear Diodes spectrometer. Source to window distance 4.85 cm."

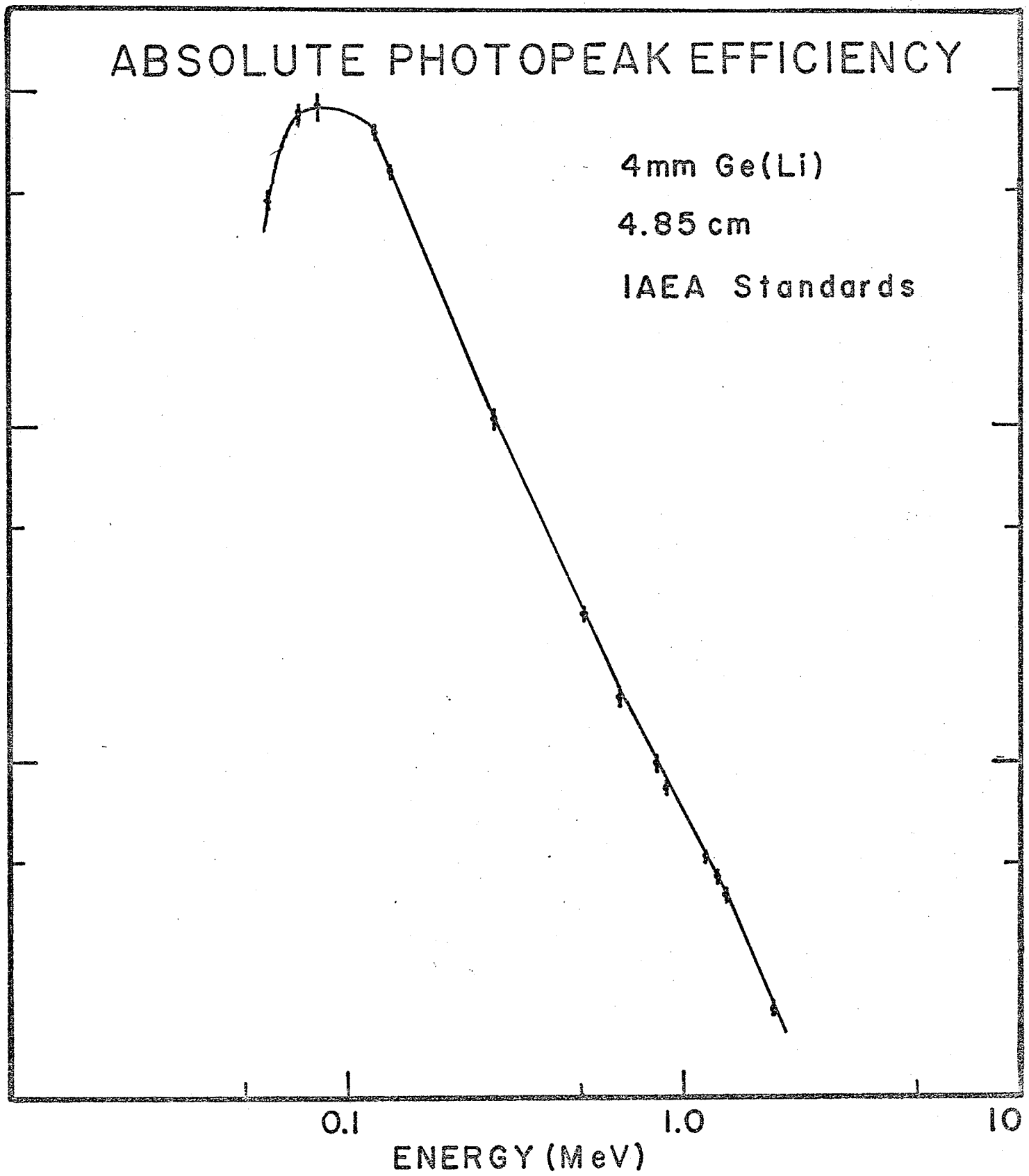
ABSOLUTE PHOTOPEAK EFFICIENCY
4mm Ge(Li)
4.85 cm
IAEA Standards
3
4
5
6
0.1
1.0
10
ENERGY (MeV)

Figure 1.4

"Absolute photopeak efficiency of Ortec X-ray spectrometer. Source to window distance 0.95 cm."

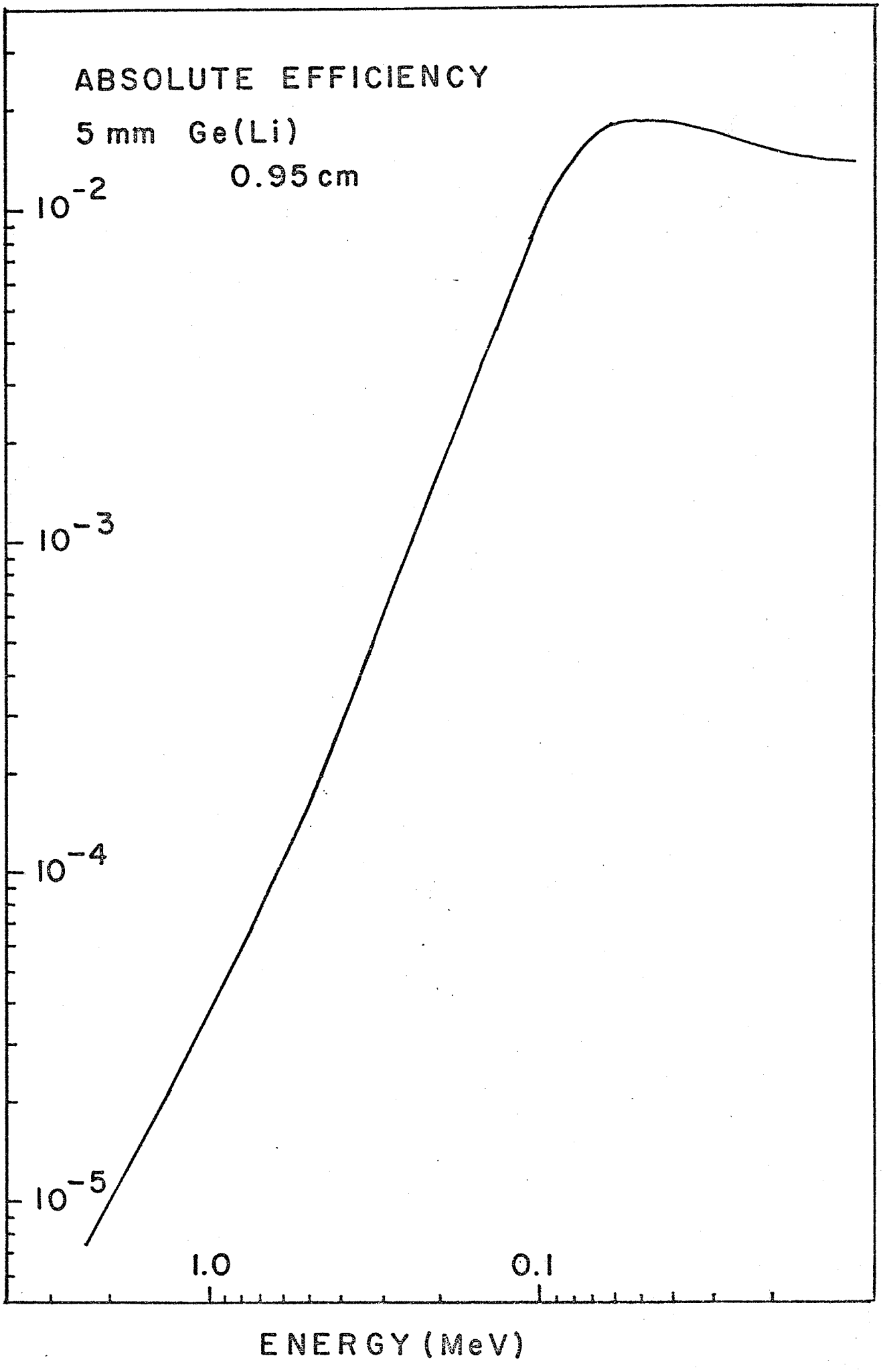
ABSOLUTE EFFICIENCY
5 mm Ge(Li)
0.95 cm
10^-2
10^-3
10^-4
10^-5
1.0
0.1
ENERGY (MeV)

detectors in the accumulation of single gamma ray spectra is manifest, difficulties soon arise when one attempts to use two such devices to detect gamma rays in coincidence. As is well known the main problems are low detection efficiency and rather long charge collection times which vary according to the position of the ionizing events in the crystal and the energy of the radiation. The former gives rise to low coincidence counting rates and the latter to poor time resolution. Many workers have attempted to circumvent partially these drawbacks by using hybrid systems employing one Ge(Li) detector and one NaI crystal and have met with considerable success. Even relatively small Ge(Li) detectors can be used in this way[3].

The development and perfection of the axial drift method of lithium compensation has led recently to extremely large Ge(Li) detectors with active volumes up to 40 cc and higher. With such large volume crystals complete solid state coincidence systems become quite feasible. Moreover improvements in developing fast timing pulses from charge sensitive preamplifiers have greatly enhanced the time resolution capabilities of solid state detectors. Germanium and silicon detectors cannot of course compete in time resolution with NaI and plastic scintillators, but certainly much stronger sources can now be used in conventional coincidence experiments for decay scheme analyses as a consequence of this improvement.

The 35 cc and 20 cc Ge(Li) counters discussed earlier

in this chapter were used as the basis of a gamma-gamma coincidence spectrometer in the Hg^{195} decay studies which follow. Fig. 1.5 is a block diagram of the fast-slow coincidence system used, also showing the geometry. The source (vacuum sublimed or drop evaporated) is mounted between two disks of 1 thou aluminum foil suspended as shown in an anti-scattering shield of 0.6 cm lead sandwiched between two 0.2 cm thick copper plates. The lead-copper shield effectively eliminated compton scattering from one crystal to the other, such scattering having the undesirable effect of producing spurious peaks in the coincidence spectra. Fast timing pulses are derived from the unshaped preamplifier pulses with two leading edge time pick-off units (Model C129A+). The timing pulse is triggered whenever the preamplifier output voltage rises above a certain preset discriminator level which is usually set just above noise. The difference in arrival time of any pair of such pulses from the two detectors is converted into an analogue voltage pulse by a C111+ time analyzer (normally set for a range of 1 μsec). This "time spectrum" as observed at terminal A can then be fed directly into a multi-channel analyzer and the resulting pulse height distribution gives an indication of the performance of the system. If the detectors are sensitive to coincident radiations the time spectrum will show a "prompt coincidence" peak. An example of this is shown in Fig. 1.6(a), for a Na^{22}

+Conuclear Ltd., Winnipeg, Manitoba

Figure 1.5

"Fast-slow coincidence system employing two Ge(Li) detectors."

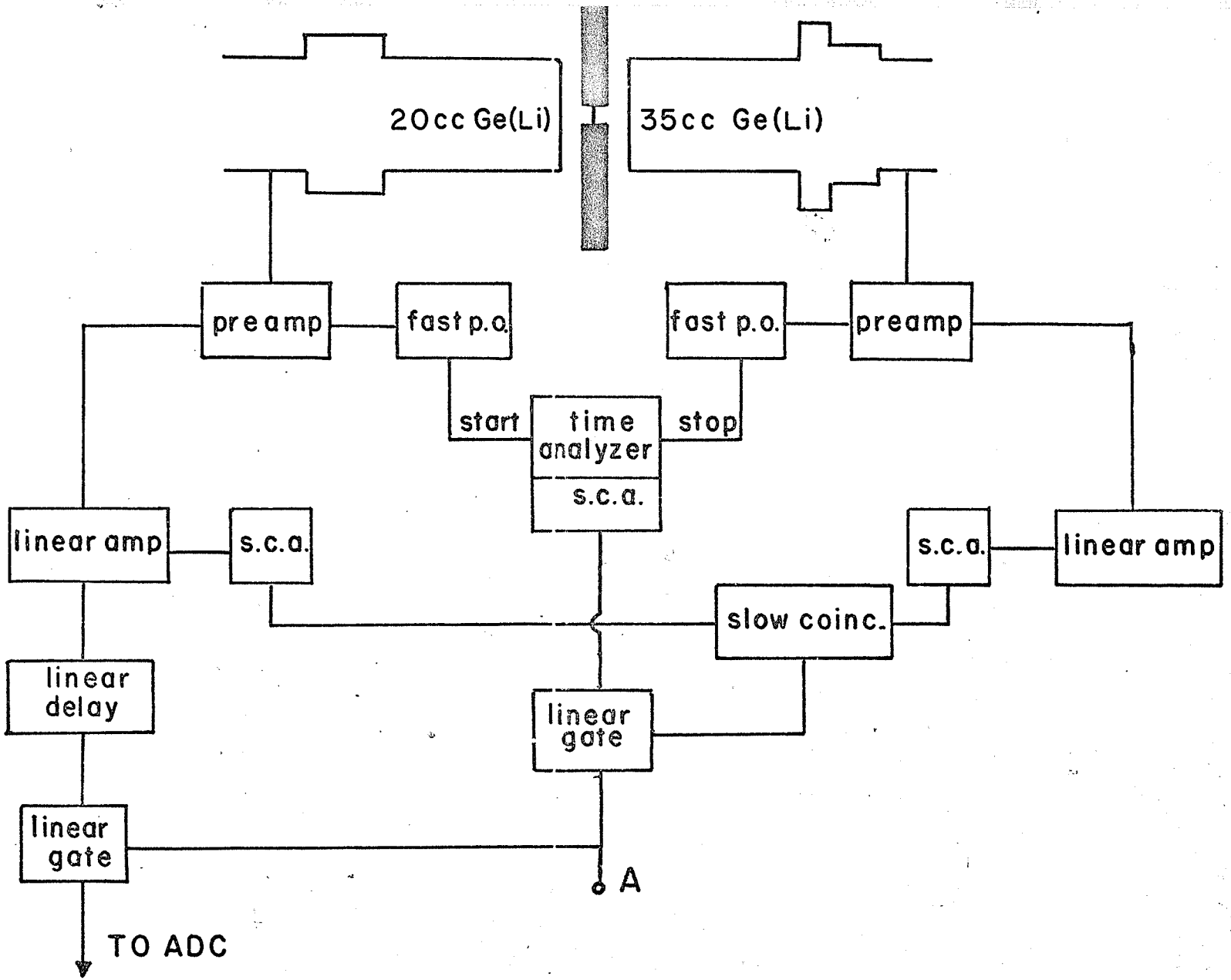
20cc Ge(Li)
35cc Ge(Li)
preamp
fast p.o.
fast p.o.
preamp
start
time analyzer
stop
s.c.a.
linear amp
s.c.a.
s.c.a.
linear amp
slow coinc.
linear delay
linear gate
linear gate
A
TO ADC

Figure 1.6

(a) Prompt coincidence peak in time analyzer output, no energy requirements

(b) Prompt coincidence peak with side channels

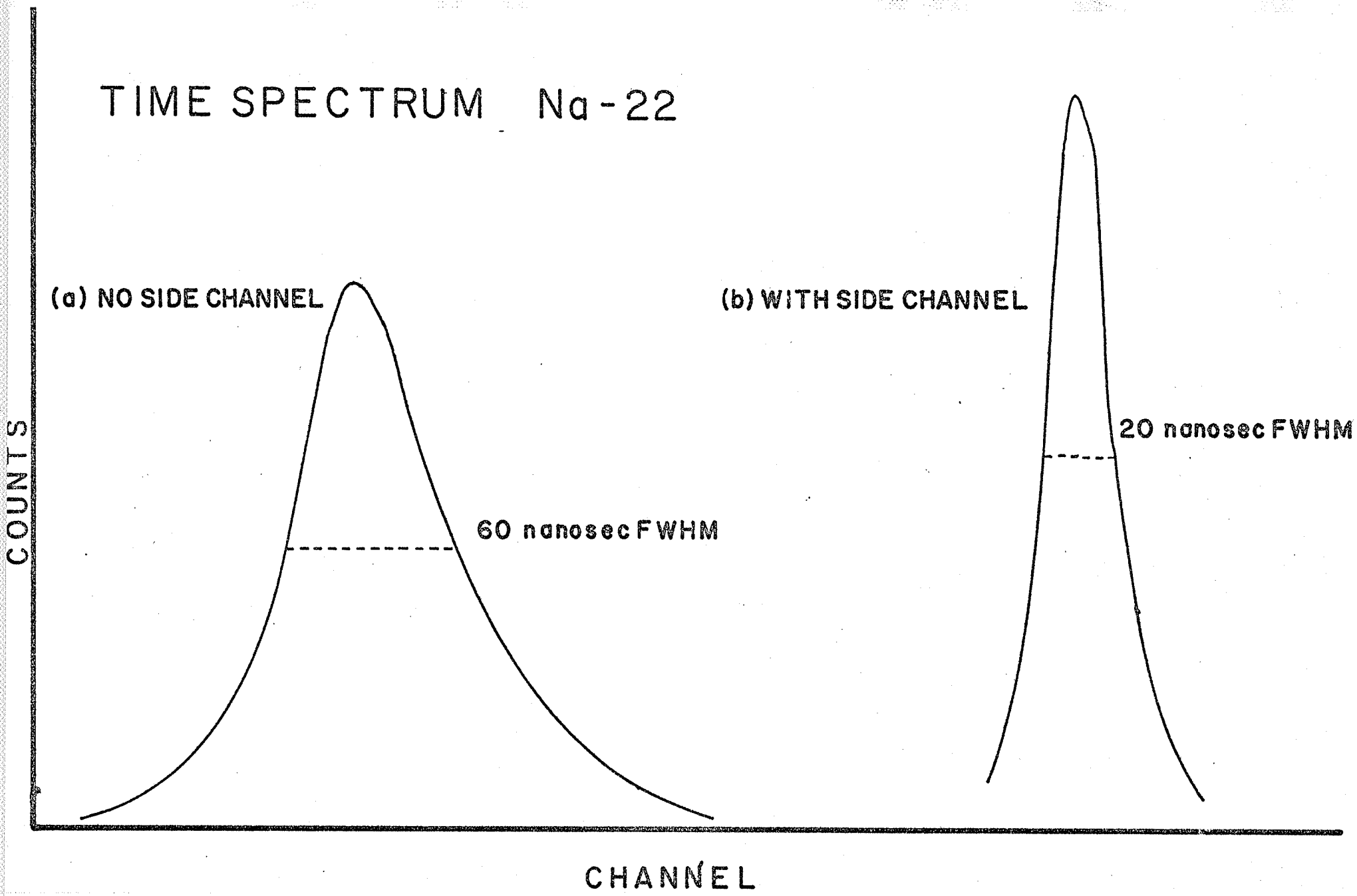
TIME SPECTRUM Na-22
(a) NO SIDE CHANNEL
60 nanosec FWHM
(b) WITH SIDE CHANNEL
20 nanosec FWHM
COUNTS
CHANNEL

gamma source. The width of the coincidence peak is limited by the fluctuations in rise time of the pre-amp pulses going into the time pick-off units. These fluctuations have two main causes:

(1) Irregular charge collection time of the crystal. This is a geometrical effect, resulting from non-uniformities in the electric field in the depletion region of the detector and from the differing mobility of holes and electrons in that region.

(2) Amount of charge collected. Because of the Compton effect, the detectors produce a continuum of charge pulses ranging up to the full energy of the gamma ray. Since the discriminator levels on the time pick-offs are set at fixed values, we would expect the time of generation of fast timing pulses to be dependent on the size of the preamplifier voltage pulses.

The second limitation can be circumvented at least partially with the use of "side channels" or single channel analyzers (S.C.A.) which put energy restrictions on the fast coincidence pulses. In Fig. 1.5 the output of the time analyzer is passed through a slow coincidence linear gate (C113[+]) which is opened only when the energy requirement set by two single channel analyzers is met. If at least one of these windows is set on a narrow energy range--for example on a full energy

---

[+]Conuclear Ltd., Winnipeg, Manitoba

line--the effect is to sharpen up the prompt coincidence peak and hence improve the resolving time of the system. The effect is shown in Fig. 1.6(b). A third SCA on the output of the time analyzer can then be set on this improved coincidence peak to any width (resolving time) desired, in this way eliminating all random coincidence pulses except those falling within this window. The output pulses from the linear gate are then used to open a second linear gate which allows the delayed, shaped energy pulses from one of the detectors through to the multi-channel analyzer.

As can be seen from Fig. 1.6(b) typical coincidence resolving times obtainable with this system were of the order of 20-30 nanoseconds. As a matter of interest, one of the Ge(Li) detectors (the 20 cc one) was examined alone for its optimum timing characteristics using the same fast-slow coincidence system described above. In this test the time analyzer was started with Na^{22} positron pulses generated in NE102 plastic scintillator, and stopped by the resulting annihilation radiation detected in the Ge(Li) crystal. The time spectrum is shown in Fig. 1.7. Quite narrow side channels were set on the gamma and β-spectra. The best resolution obtainable is seen to be 11 nanoseconds FWHM. The asymmetry in the peak shape can be attributed to the irregular charge collection time of the crystal as discussed above.

As an example of the performance of the coincidence

Figure 1.7

"Timing characteristics of Princeton Gamma Tech detector."

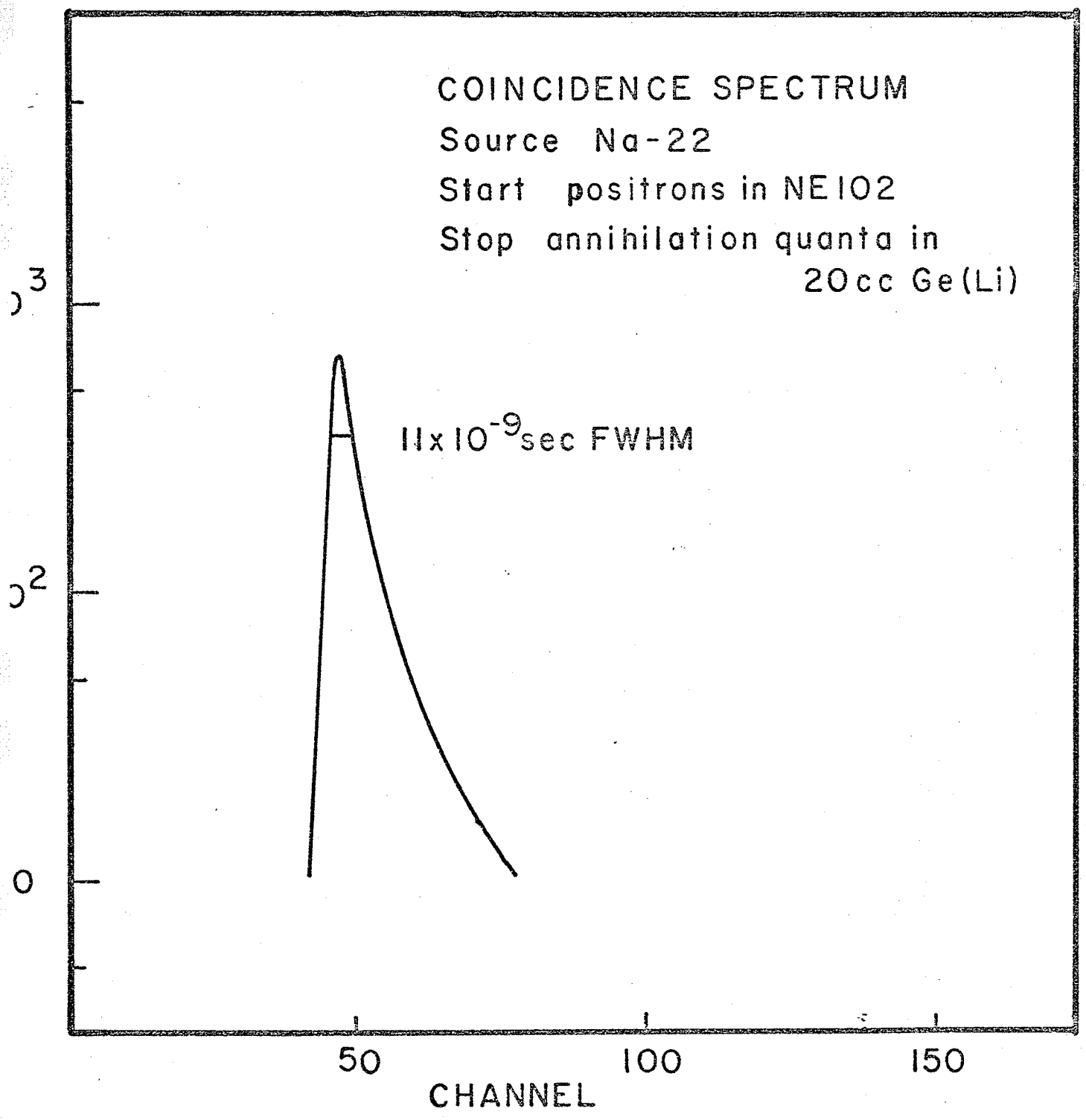
COINCIDENCE SPECTRUM
Source Na-22
Start positrons in NE102
Stop annihilation quanta in
20cc Ge(Li)
11x10⁻⁹sec FWHM
10³
10²
0
50
100
150
CHANNEL

system in practice, Fig. 1.8 shows a Co^{60} gamma-gamma coincidence spectrum as observed in the 20 cc Ge(Li) detector. The side channel on the 35 cc detector is shown in Fig. 1.9 set on the 1333 keV line which is in cascade with the 1172 keV line. The side channel on the 20 cc detector was left effectively wide open. The presence of the 1333 keV line in Fig. 1.9 is due to random coincidence pulses falling within the preset window on the time analyzer. Its intensity indicates a true to random event ratio of about 40 to 1.

In most of the coincidence spectra reported in this work, the narrow side channel is set on the 35 cc detector. This is done to take full advantage of its excellent peak to Compton ratio (16:1 under ideal conditions). Compton pulses from higher energy gamma rays that fall within the selected energy window can greatly complicate the resulting coincidence spectrum and hence should be avoided as much as possible.

(v) Instrumentation for Directional Correlation Measurements

Gamma-gamma directional correlation experiments were performed in this study to aid in angular momentum assignments for levels in Au^{195}. We shall conclude this chapter on gamma ray detectors with a discussion of the design and performance of the angular correlation table used. (The theory and method of interpretation of gamma ray directional correlations are presented in Chapter IV).

Figure 1.8

"Co^{60} singles spectrum with Ortec 35 cc detector, showing side channel position."

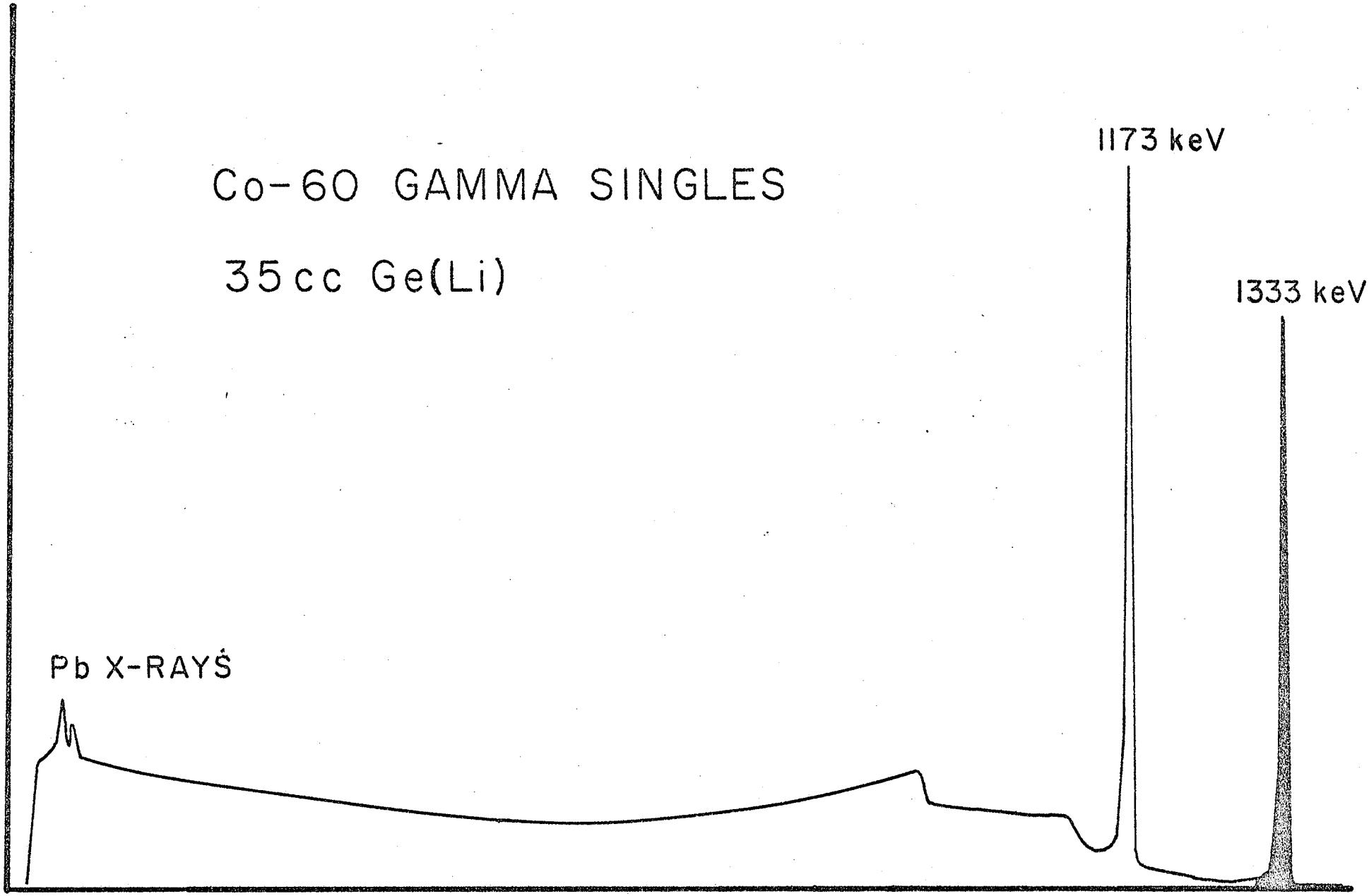
Co-60 GAMMA SINGLES
35cc Ge(Li)
1173 keV
1333 keV
Pb X-RAYS

Figure 1.9

"Co^{60} coincidence spectrum."

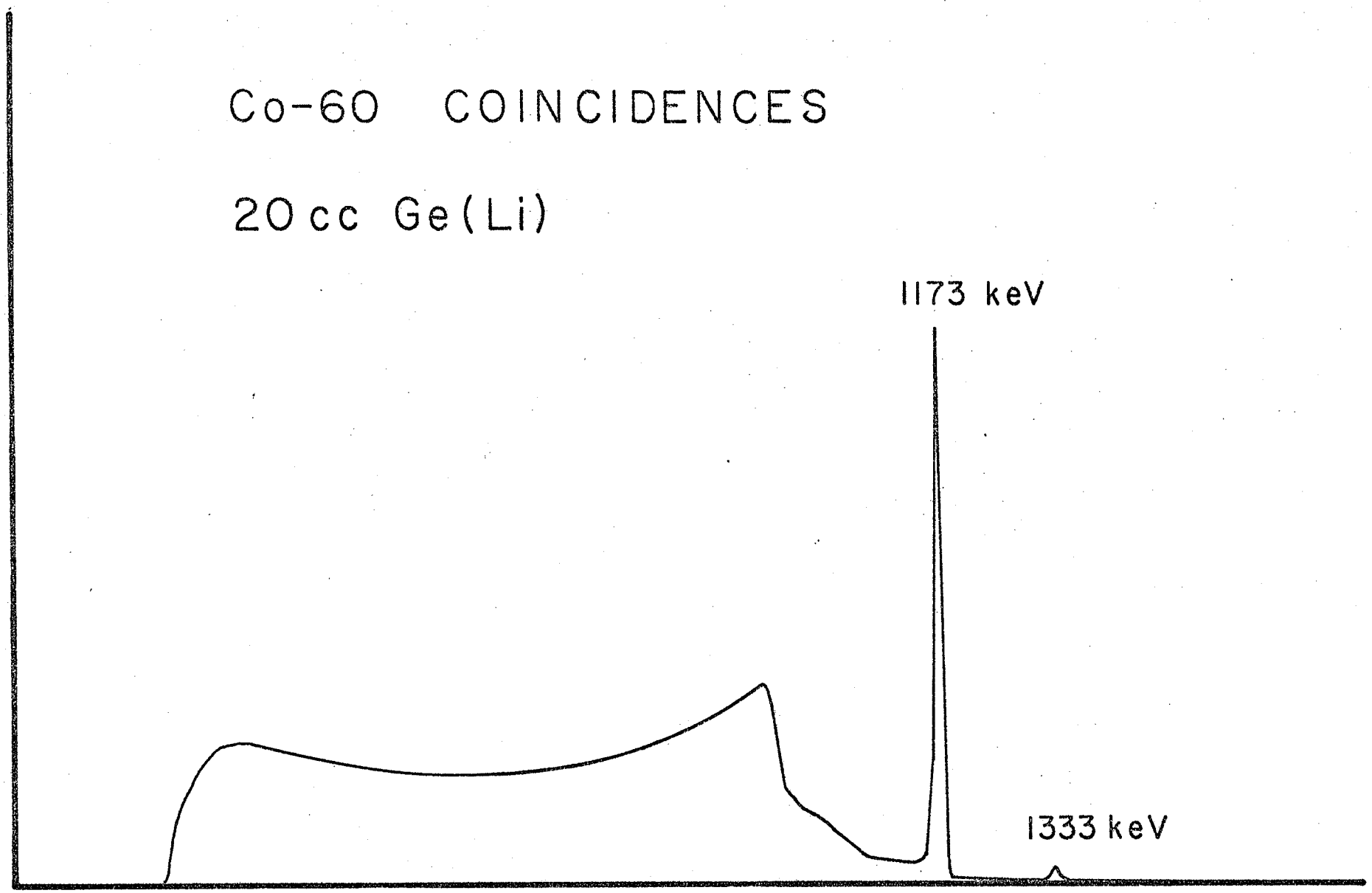
Co-60 COINCIDENCES
20 cc Ge(Li)
1173 keV
1333 keV

A diagram of the counting apparatus* is presented in Fig. 1.10. The source is mounted centrally in a 15.8 cm diameter aluminum 'can' which forms the base of a cryostat for a Si(Li) electron detector when the system is used for electron-gamma directional correlation measurements. The source shown in the diagram can be drop evaporated or vacuum sublimed and is supported by a thin aluminum backing. If a liquid source is preferred, a hollow perspex tube, also mounted centrally can be used. One of the two radiations involved in the correlation is detected in the 35 cc Ge(Li) detector and the line joining the center of this detector and the source defines the 0° direction. Three identical 2" x 2" NaI detectors specially selected to have closely the same efficiency and resolution define the 90°, 135°, and 180° angles. The NaI detector-photomultiplier assemblies are coupled to C402 probes[+] designed to produce simultaneously pulses suitable for energy analysis and timing applications. Each probe contains two sections, a charge sensitive preamplifier and a timing section. The pre-amplifier integrates the photomultiplier output and produces an energy proportional signal, while the timing section produces both fast and slow standard logic pulses that correspond to the leading edge of the photomultiplier pulse. The photomultiplier tubes employed with the probes are supplied with high voltage

---

[+]Conuclear Ltd., Winnipeg, Manitoba

*Reported by D. L. Salie, Western Regional Nuclear Conference, Regina, Sask. (1968)

Figure 1.10

"Geometry for gamma-gamma directional correlations."

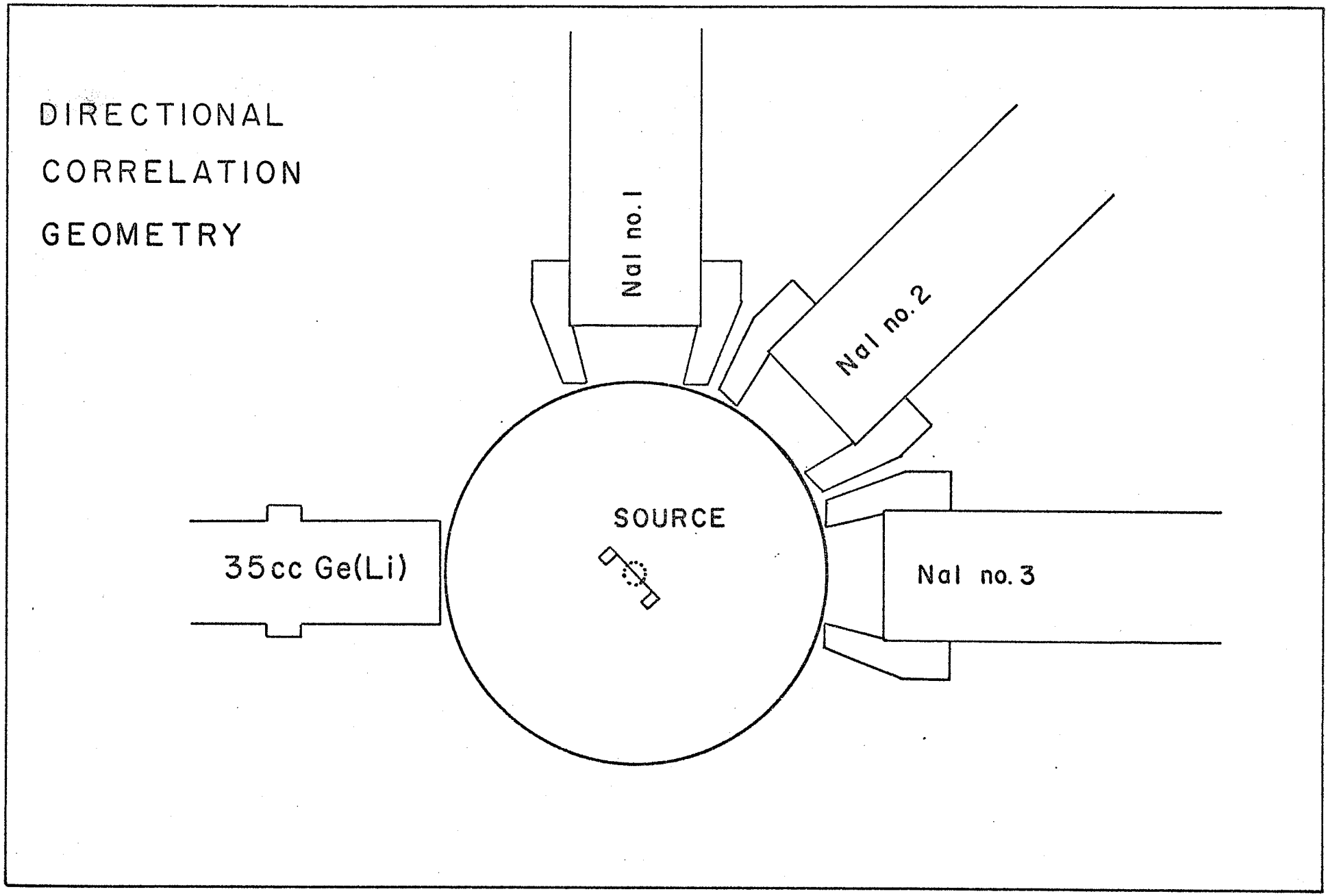
DIRECTIONAL
CORRELATION
GEOMETRY
NaI no.1
NaI no.2
SOURCE
35cc Ge(Li)
NaI no.3

from a single Fluke 405B 2.5 kV power supply. The three probes are positioned equidistant from the source and are shielded from each other by lead cones which define a precise half angle of 7.35° at the source for a source to detector distance of 10.50 cm.

A fast-slow coincidence logic system designed to enable the accumulation of data at all three angles simultaneously is presented in Fig. 1.11. The energy proportional pulses from the three NaI preamplifiers are passed via an adder amplifier (ADD 1) which is equipped with fine gain adjustments for gain matching. As the pulses from the three NaI detectors are not coincident the adder merely passes the signals without distortion to the linear amplifier where the pulses are shaped and amplified and passed on to a single channel analyzer (SCA 2). The energy windows on the NaI spectra are thus set simultaneously with one SCA. The fast timing pulses from the NaI detectors are fed into a logic OR gate which produces an output pulse whenever a timing pulse from any NaI detector appears at its input. This pulse is used to start the time analyzer. The time analyzer is stopped with the fast time pulses from the Ge(Li) detector as produced in a leading edge time pick-off (TPO). Linear, shaped energy pulses from the Ge(Li) detector are fed into another SCA (SCA 3). SCA 2 and SCA 3 control a slow coincidence linear gate through which the fast coincidence pulses from the time analyzer are fed. These two SCA's act as

Figure 1.11

"Fast-slow coincidence and logic for directional correlation experiments."

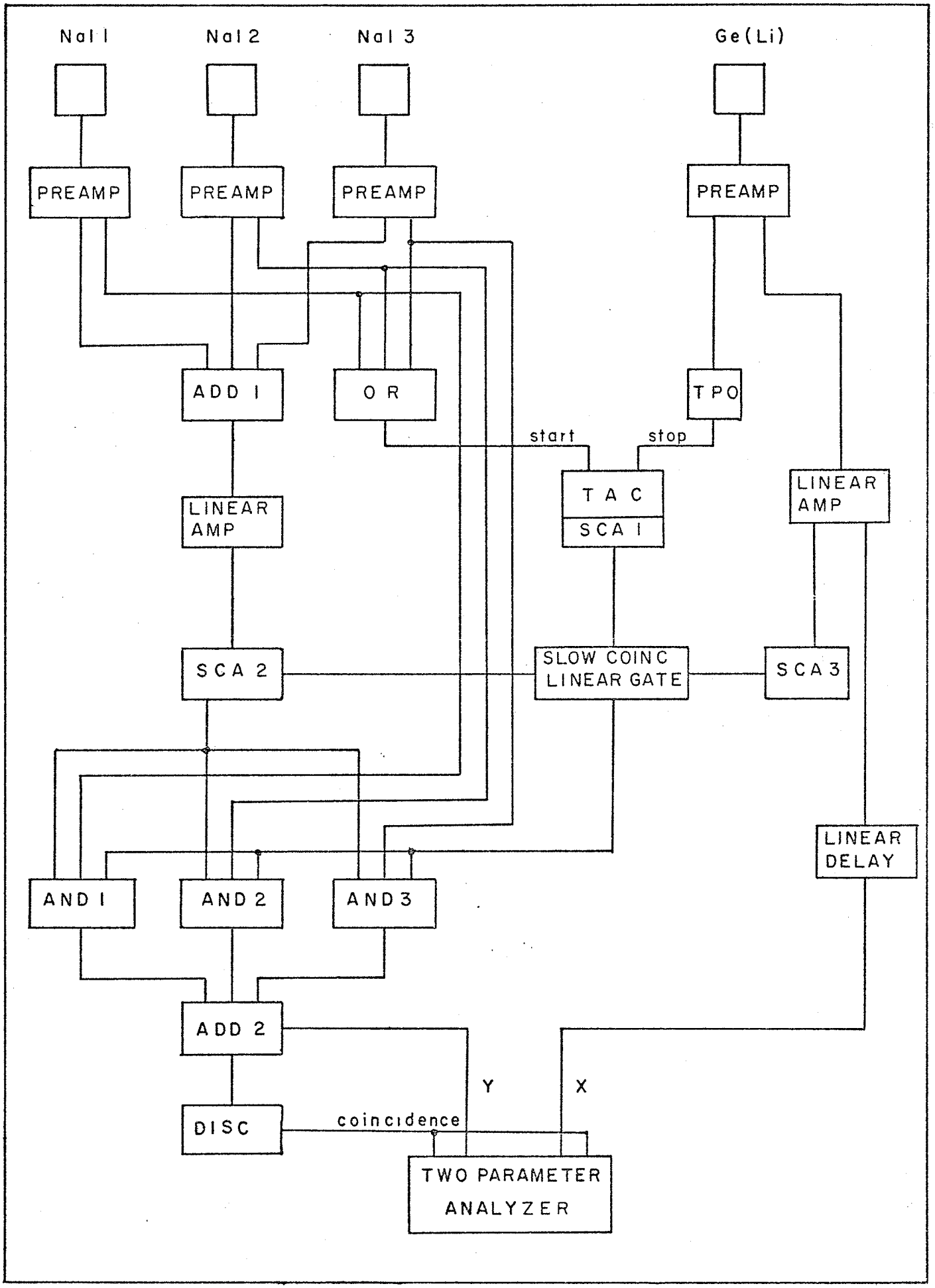
NaI 1
NaI 2
NaI 3
Ge(Li)
PREAMP
PREAMP
PREAMP
PREAMP
ADD 1
O R
T P O
start
stop
T A C
SCA 1
LINEAR AMP
LINEAR AMP
SCA 2
SLOW COINC LINEAR GATE
SCA 3
LINEAR DELAY
AND 1
AND 2
AND 3
ADD 2
Y
X
DISC
coincidence
TWO PARAMETER ANALYZER

side channels in the same manner as in the γ- γ coincidence system discussed in part (iv) of this chapter. They serve to sharpen up the prompt coincidence peak from the time analyzer. SCA 1 is set on this prompt coincidence peak and its window width determines the resolving time of the experiment.

In order to understand the operation of the rest of the system, it is perhaps simplest to consider an example. Suppose coincident radiations are detected in NaI 2 and the Ge(Li) detector, and suppose further that the corresponding energy pulses are within the windows set by SCA 2 and SCA 3. Then a "fast-slow" coincidence logic pulse will appear at the output of the slow coincidence linear gate and be presented simultaneously to three "and" gates (AND 1, AND 2, AND 3). At the same time, a logic pulse from SCA 2 is presented to the 3 "and" gates, and a logic timing pulse from NaI 2 is presented to AND 2. Thus, AND 2 alone will produce an output which is fed via a second adder amplifier (ADD 2) to the Y input of a two parameter analyzer. This routing pulse also fires a low level discriminator which opens the coincidence gates to both inputs of the analyzer. The delayed energy pulse from the Ge(Li) detector is then accepted and stored in a section of the memory controlled by the amplitude of the routing pulse from AND 2. In this experiment the dual ADC was run in the 4 x 1024 channel mode and the routing pulses from the 3 'and' gates chosen so as to put the 3 coincidence spectra into

channels 1025-2048, 2049-3072, and 3073-4096 respectively. Channels 1-1024 were reserved for monitoring singles spectra from the various detectors dueing the run.

Because of its ability to collect data at all angles simultaneously this system has an obvious advantage over 2-counter systems when short lived sources are studied since no source decay corrections are necessary. In the case of $Hg^{195,195m}$ which does not have a simple exponential decay such corrections would have been difficult indeed. The main disadvantage of the system (apart from the comparatively poor resolution of NaI detectors) is the stringent requirement that the gain and resolution of the three NaI detectors be matched, and remain so throughout the experiment. In all the runs reported in the present work the singles spectra from the three NaI detectors as well as the gated singles counting rate as observed at the output of SCA 2 were regularly monitored. This is done by removing all but the appropriate input to ADD 1. The gated singles rates at each angle were used to normalize the three coincidence spectra, and never differed, from angle to angle, by more than one percent.

In order to test the reliability of this system a directional correlation experiment on the gamma rays of Co^{60} was performed. The decay of this isotope is well known and the pertinent parts are shown in Fig. 1.12.

The single channel analyzer common to the three NaI detectors (SCA 2) was set on the full energy line of the

Figure 1.12

"Co^{60} decay scheme."

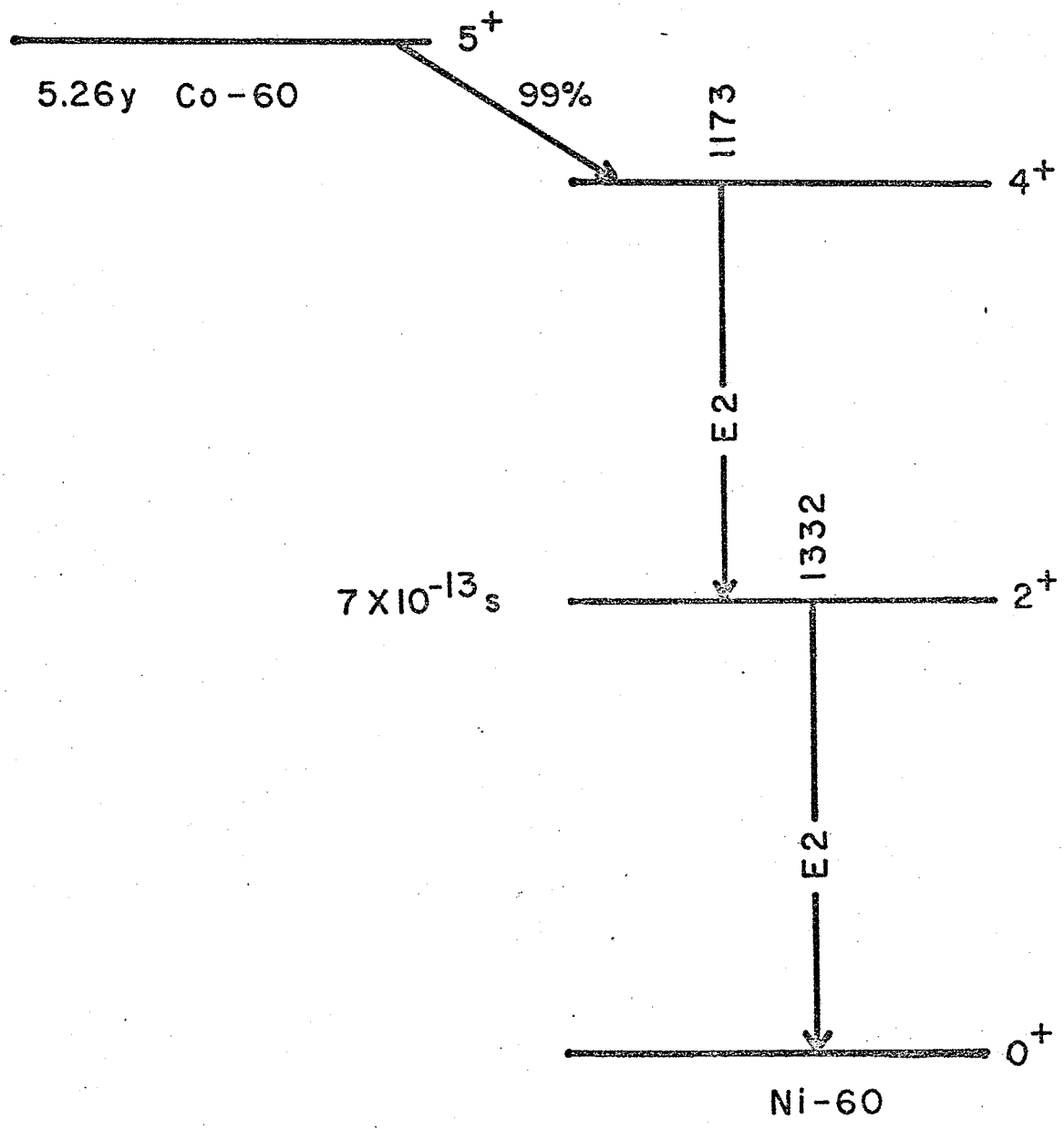
5+
5.26y Co-60
99%
1173
4+
E2
1332
7X10-13 s
2+
E2
0+
Ni-60

1332 keV gamma ray. The Ge(Li) side channel (SCA 3) was set to receive all energy pulses above about 1 MeV. Data was accumulated for 18½ hours. The number of counts in the 1173 keV coincidence peaks observed at each angle was approximately 9000. The random coincidence rate was estimated from the relative intensity of the 1332 keV line in the 3 coincidence spectra and was about 1% of the true coincidence rate. After subtraction of random and compton background, and normalization to the singles counting rate at each angle the angular correlation coefficients in the theoretical expression

$$W(\theta) = 1 + a_2 P_2 (\cos\theta) + a_4 P_4 (\cos\theta)$$

were determined according to the method of White[4]. (This method is outlined in Appendix II, as is the method of finite solid angle correction.)

The results are $a_2 = 0.106 \pm 0.012$

$a_4 = 0.005 \pm 0.013$

The error here is statistical.

After correction for the finite solid angles of the four detectors the coefficients became

$a_2 = 0.111 \pm 0.012$

$a_4 = 0.006 \pm 0.013$

These coefficients are in agreement with the accepted[5] values of

$a_2 = 0.1020$

$a_4 = 0.0091$

It was concluded from this result that the angular correlation system was performing satisfactorily.

REFERENCES, CHAPTER I

1. G. E. Keller, E. F. Zganjar and J. J. Pinagian, Nucl. Phys. A129, 481 (1969).

2. C. M. Lederer, J. M. Hollander, and I. Perlman, Table of Isotopes, 6th Ed., Wiley (1968).

3. J. Ungrin and M. W. Johns, Nucl. Phys. A127, 353 (1969).

4. D. H. White, Nuclear Instruments and Methods 21, 209 (1963).

CHAPTER II

A SOLID STATE INTERNAL CONVERSION COEFFICIENT SPECTROMETER

(i) General Principles

A solid state internal conversion spectrometer similar to that described by Hollander[1] was constructed in this laboratory. Fig. 2.1 is a block diagram of the experimental arrangement. A Si(Li) electron detector and a Ge(Li) detector face each other in fixed geometry. Radioactive sources on standardized source mounts are placed between the two detectors in a well defined, reproducible position. The gamma ray spectrum and associated conversion electron spectrum are accumulated simultaneously in two essentially independent pulse height analyzers for a convenient period of time. In this work two analogue to digital converters shared a single memory by means of a digiplex system. The two solid state detectors are calibrated for full energy peak efficiency, and internal conversion coefficients are obtained simply by taking appropriate ratios of full energy peak intensities.

The internal conversion coefficient for electrons in the i°th subshell corresponding to an isomeric nuclear transition of energy E is defined as

$$\alpha_i = \frac{N_{ei}\ (E - W_i)}{N_\gamma\ (E)} \qquad (1)$$

Figure 2.1

"Internal conversion coefficient spectrometer, experiment arrangement."

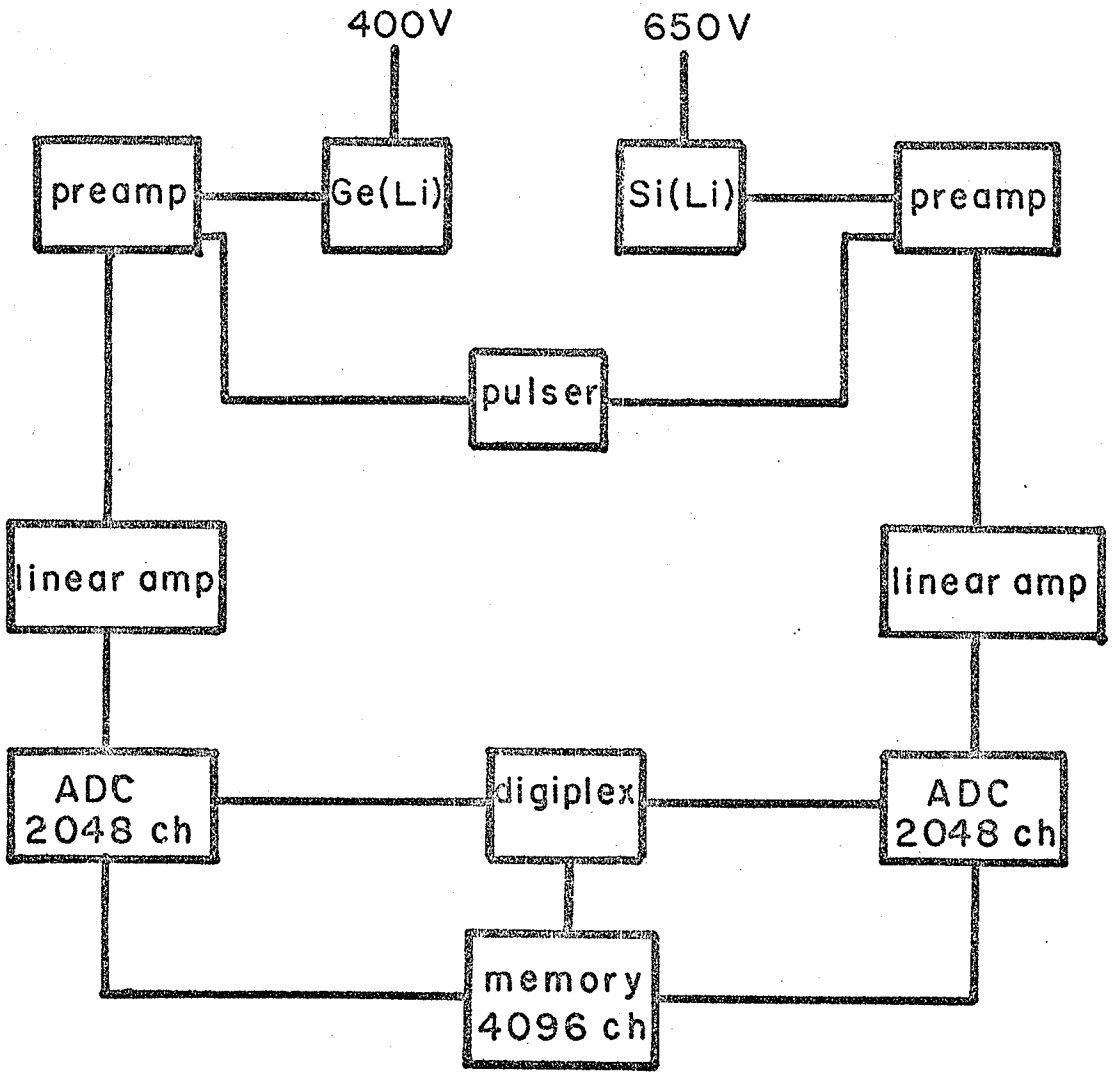
400V
650V
preamp
Ge(Li)
Si(Li)
preamp
pulser
linear amp
linear amp
ADC
2048 ch
digiplex
ADC
2048 ch
memory
4096 ch

where $N_{e_i}(E)$ is the number of i-shell electrons emitted per unit time with energy E, N (E) is the number of gammas emitted per unit time with energy E in the same transition, and W_i is the i-shell binding energy. Thus, experimentally,

$$\alpha_i = \frac{n_{e_i}}{n_\gamma} \frac{\epsilon_\gamma(E)}{\epsilon_e(E-W_i)} \qquad (2)$$

n_{e_i} = number of i-shell electron full energy pulses detected during data accumulation time

$n_\gamma(E)$ = number of γ-ray full energy pulses detected having energy E

$\epsilon_\gamma(E)$ = gamma detector photopeak efficiency at energy E

$\epsilon_e(E)$ = electron detector efficiency at energy E

Equation (2) is not exactly correct if there are significant dead time losses in the ADC's. If this is the case, the actual times for which the two detector systems are sensitive to incident radiation--i.e. the "live times"--will not in general be equal. This will of course depend on the choice of source to detector distances and on the nature and strength of the source. In order to correct for this effect a pulser (see Fig. 2.1) has been included in the experimental arrangement. The pulser is fed into the test inputs of both preamplifiers and the pulser peaks are accumulated along with the spectra. If the half-life of the source is of the order of or shorter than the accumulation time, the pulser should be left on throughout the run, as the ratio of dead times of the two ADC's will not be constant. Otherwise it need only be

turned on for a short time at the beginning or end of the run. If P_e and P_γ are the number of counts in the pulser peaks in the electron and gamma spectra respectively, the corrected version of (2) is

$$\alpha_i = \frac{n_{e_i}}{n_\gamma} \frac{\epsilon_\gamma(E)}{\epsilon_e(E-W_i)} \frac{P_\gamma}{P_e} \qquad (2')$$

As we shall see in the following paragraphs, this technique can be expected to give K- and L- shell conversion coefficients to within ± 10% for sources of sufficiently high Z for which the electron lines of interest will be resolved. While the silicon detector does not possess the resolution of large magnetic spectrometers, this degree of accuracy in the determination of α_i is typical of that currently appearing in the literature using other techniques and is quite good enough to determine the multipolarity of a given transition. Moreover this system enables data on a large number of transitions to be collected simultaneously. The method is therefore well suited to the study of short lived activities. Such activities can be handled only with difficulty by more conventional instruments which collect data on a point by point basis.

(ii) The Electron Detector

A diagram of the electron detector cryostat and vacuum chamber is shown in Fig. 2.2. The Si(Li) detector (model No. A-80-3) was obtained from Kevex corporation, California. Its

Figure 2.2

"Electron detector cryostat and vacuum chamber."

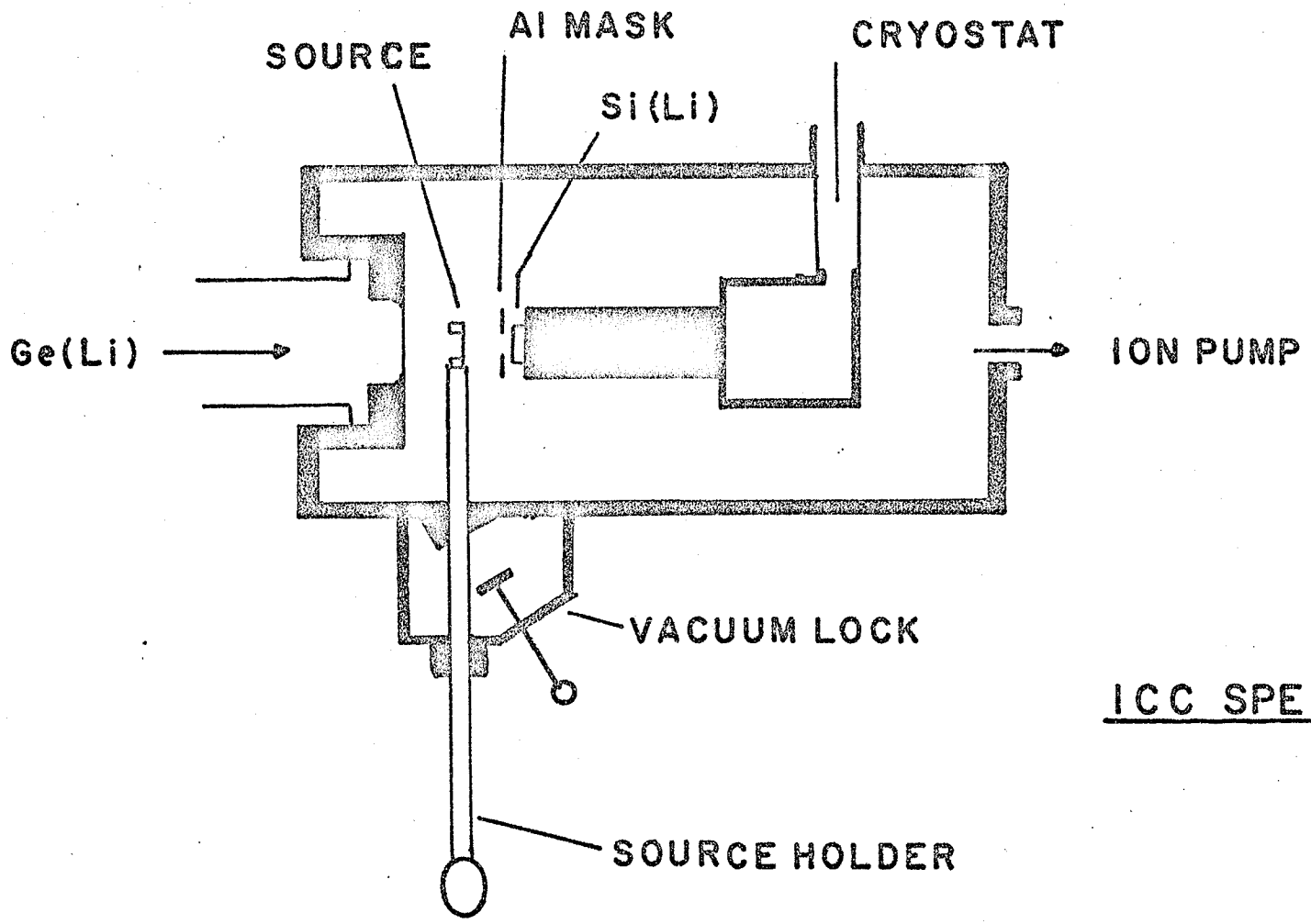

ICC SPECTROMETER

sensitive area was 80 mm^2 with a depletion depth of 3 mm. The sensitive region was further restricted to 56.5 mm^2 by a 0.125 inch thick aluminum mask. This was done to improve the full energy line shape by eliminating possible edge effects in the Si(Li) crystal. The detector was maintained at 77°K by means of a brass "cold finger" attached to a small liquid nitrogen cryostat. This latter was suspended from the top of the vacuum system by a stainless steel cylinder with 0.005 inch thick walls. The level of liquid nitrogen was maintained in the cryostat with a Linde CR-10 gravity feed cold trap reservoir (not shown). When the system was cooled down, a pressure of between 10^{-6} and 10^{-7} mm Hg could be maintained with an 8 litre/sec ion pump (Varian Associates). Sources enter the main vacuum chamber via a vacuum lock which can be roughed down to about 10 microns Hg. The source position is defined by an aluminum stop fastened to the shaft of the source holder. In this geometry the source to electron detector distance was 0.60 inches. Details of the source holder and source mount are shown in Fig. 2.3.

The manufacturers of this detector recommended that its surface not be touched under any circumstances because it was covered with a very thin exposed layer of evaporated gold. Occasionally small oil droplets were visible on this surface, presumably due to the vacuum lock being repeatedly opened. Such contaminations, when they occurred, were effectively

Figure 2.3

"Source holder and mount."

SOURCE HOLDER

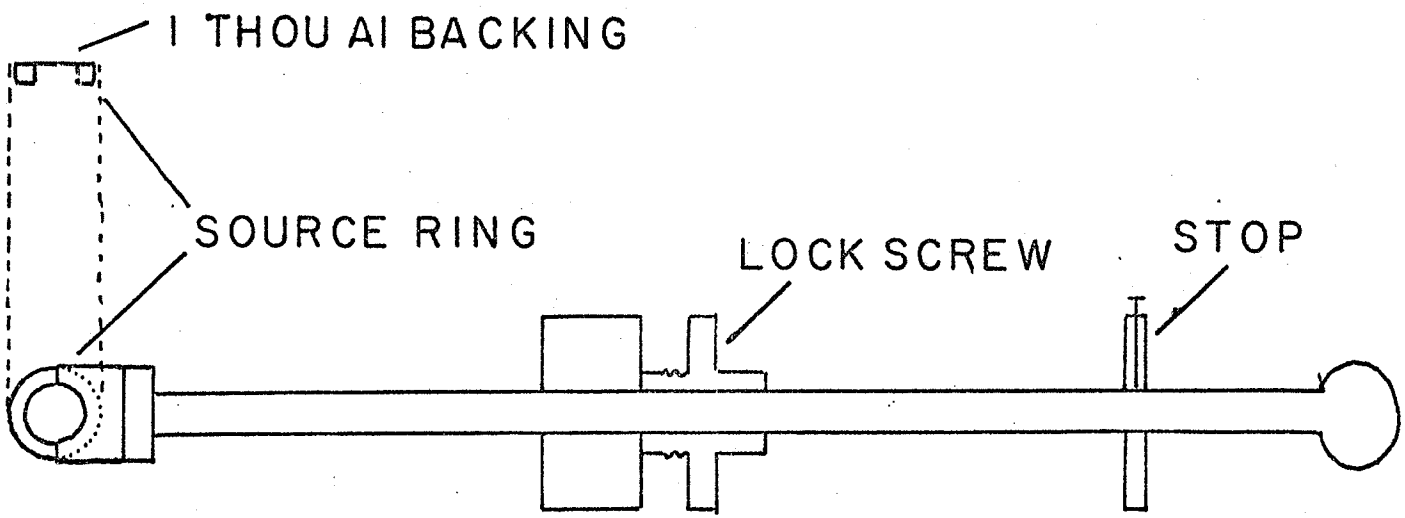

removed by decoupling the detector from the cold finger, placing it on the floor of the main vacuum chamber and pumping the system down to operating pressure for a period of one or two days with the cold finger at liquid nitrogen temperature.

A modified version of a Tennelec TC135M preamplifier was used to collect pulses of charge from the detector. The modification, performed in our laboratory, consisted of removing the first stage of preamplification and placing it inside the vacuum system with the field effect transistor mounted on the cold finger, directly behind the detector.

As can be seen, considerable care was taken with the electron detector in order to optimize its energy resolution. It was felt that the success of the system would depend critically on the performance of the electron detector. Since conversion electron spectra in which K, L and M lines are separated are in effect three times as complex as the corresponding gamma spectra, a poor electron response function would limit the internal conversion spectrometer's application to very simple decay schemes. The actual performance of the electron side of the spectrometer is discussed in section (iv).

(iii) The Gamma Detector

A commercial detector-cryostat-preamplifier system was used for gamma detection. This instrument, obtained from Nuclear Diodes Inc. had a depletion depth of 4 mm with an active (planar) volume of 0.5 cm^3. The design is conventional and is

shown schematically in Fig. 2.4. The preamplifier (not shown) was a Tennelec model TC130, again with cooled first stage. The front wall of the vacuum chamber for the electron detector was designed to accept the Ge(Li) detector cryostat with only a few thousandths of an inch clearance. This effectively defined the position of the gamma detector, inside its cryostat, as 1.0 inches from the source.

(iv) Calibration and Performance of the Spectrometer

The method of calibration of Ge(Li) gamma detectors used in the present studies was discussed in Chapter I. In Fig. 2.5 is plotted an absolute photopeak efficiency curve for the 4 mm Ge(Li) detector. The calibration extends from 60 keV to 2.6 MeV and may be considered as reliable to ± 5% over the range 0.1 to 1.4 MeV which includes the main region of interest in the present studies. Because of the experimental difficulty in positioning the standard gamma sources inside the electron detector vacuum chamber, the Ge(Li) detector was calibrated separately and in a geometry only roughly equivalent to that of the conversion coefficient spectrometer. Since one is just comparing unknown conversion coefficients with those of standard sources, only the shapes of the two detector efficiency curves need be known--i.e. relative efficiences vs. energy--for then they can be normalized to each other via the internal conversion coefficient of a single standard. Thus no great care need be taken in reproducing the spectrometer geometry of

Figure 2.4

"Nuclear diodes Ge(Li) gamma ray spectrometer."

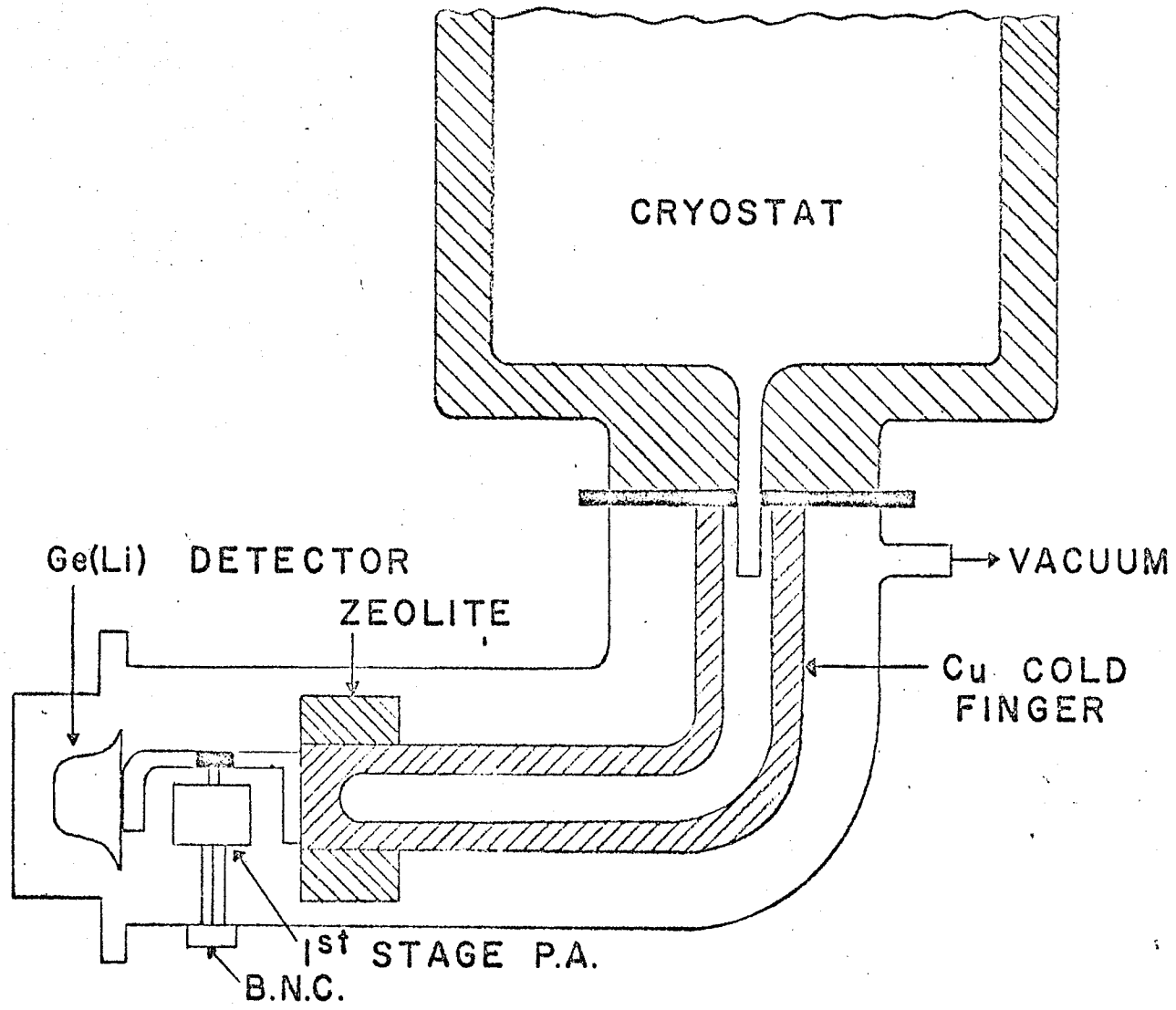

CRYOSTAT AND DETECTOR ASSEMBLY

Figure 2.5

"Photopeak efficiency of gamma detector used in conversion coefficient measurements."

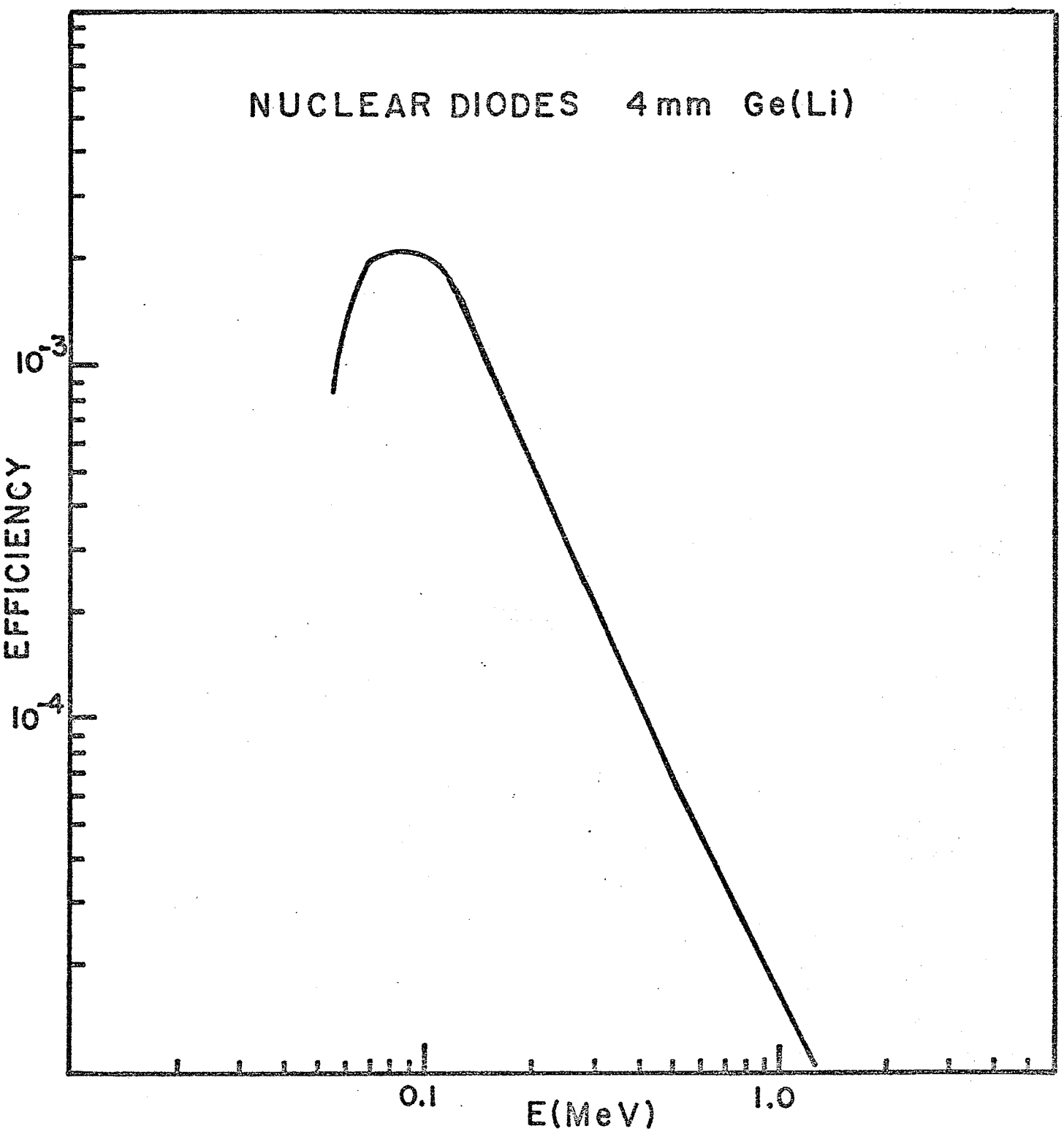
NUCLEAR DIODES 4mm Ge(Li)
EFFICIENCY
10^{-3}
10^{-4}
0.1
1.0
E(MeV)

Fig. 2.2.when calibrating the gamma detector. However since the calibration geometry was close to the conversion spectrometer geometry we shall continue to refer to "absolute" detector efficiencies. Allowance was made in the gamma ray calibration for the thickness of the window of the electron detector cryostat which consisted of 0.010" Al. The correction is negligible above 60 keV.

A full energy peak efficiency curve for the Si(Li) electron detector was obtained from this gamma efficiency curve in the energy range 60 keV-1100 keV by means of the standards listed in Table 2.1.

TABLE 2.1 STANDARDS FOR I.C.C. CALIBRATION

E_e(keV)	SOURCE	α_K (REF. 1)	NATURE OF SOURCE
62.2	Cd^{109}	11.0 ± 0.3	Vacuum sublimed
103.4	Ce^{141}	0.379 ± 0.004	Drop evaporated
126.9	Ce^{139}	0.2142 ± 0.0015	Drop evaporated
328.7	Au^{198}	0.0302 ± 0.0003	Vacuum sublimed
624.2	Cs^{137}	0.0894 ± 0.0010	Drop evaporated
1106.5	Zn^{65}	0.0001664 ± 0.0000066	Vacuum sublimed

The table also indicates the method of source preparation. The details of production of vacuum sublimed sources are discussed in Chapter III. In all cases where drop sources were used, they were of high quality and showed the minimum of solid deposition.

Table 2.2 summarizes the efficiency data obtained from these standards. In the table N_e/N_γ is the measured ratio of the number of counts in the K-electron full energy peak to the corresponding gamma photopeak, corrected for relative dead time losses as discussed above. The efficiencies listed in the last column are obtained from the relation

$$Eff_e = \frac{\alpha_K}{N_e/N_\gamma} Eff_\gamma$$

and the errors quoted are the RMS deviations obtained from the fractional errors in the quantities α_K, N_e/N_γ and Eff_γ.

TABLE 2.2 ELECTRON EFFICIENCY

E_e(keV)	N_e/N_γ	Eff_γ	Eff_e
62.2	57.35 ± 5%	2.1×10^{-3} ± 10%	0.0109 ± 0.0015
103.4	3.66 ± 5%	1.07×10^{-3} ± 5%	0.0103 ± 0.008
126.9	3.19 ± 4%	8.0×10^{-4} ± 5%	0.0120 ± 0.001
328.7	3.48 ± 2%	1.03×10^{-4} ± 5%	0.0119 ± 0.0007
624.2	30.26 ± 5%	3.63×10^{-5} ± 5%	0.0123 ± 0.0009
1106.5	0.144 ± 6%	1.42×10^{-5} ± 5%	0.0123 ± 0.0010

As an example of the determination of N_e/N_γ let us consider the case of Au^{198} (E_e = 328.7 keV). Six separate calibration runs are taken. Between each run the source holder is fully removed from the vacuum system, and the aluminum ring that serves as a base for the source backing is rotated arbitrarily in the source holder tip. The source is then

re-inserted into position. The gamma detector is likewise removed from its geometry and replaced. In this way the reproducibility of the geometry was severely tested during calibration. In Fig. 2.6 is shown the gamma and electron full energy peaks for one of these calibration runs and the assumed backgrounds. As can be seen the resolution (3.0 keV FWHM at 329 keV) and line shape of the electron detector is excellent.

TABLE 2.3 Au^{198} CALIBRATION (2000 sec COUNTING TIME)

RUN	N_e	P_e	N_γ	P_γ	N_e/N_γ	P_γ/P_e	N_e/N_γ(CORR)
1	84, 265	120, 318	27, 566	136, 223	3.05	1.13	3.46
2	81, 171	120, 203	28, 100	136, 200	2.89	1.13	3.40
3	80, 346	120, 622	27, 100	136, 146	2.98	1.13	3.38
4	66, 710	120, 795	20, 133	133, 126	3.31	1.10	3.65
5	66, 175	120, 629	20, 863	132, 988	3.17	1.10	3.50
6	51, 014	120, 452	15, 818	130, 079	3.23	1.08	3.48

The quantity in the last column is

$$N_e/N_\gamma \text{ (Corr.)} = (N_e/N_\gamma) \times P_\gamma/P_e$$

The mean of the 6 runs is 3.48 ± 0.07, i.e. an error of 2%.

Stockendal[2] has measured the relative intensities of prominent electron lines in Bi^{206} with a magnetic electron spectrometer. His results are recommended in the decay scheme tabulations of Lederer et al. (see ref. 2 Chapter I) as useful for calibration of silicon electron detectors. It was decided to check the general shape of the efficiency curve obtained from the I.C.C. standards of Table 2.1 by making use of this

Figure 2.6

"Portions of gamma and electron spectra of Au^{198}."

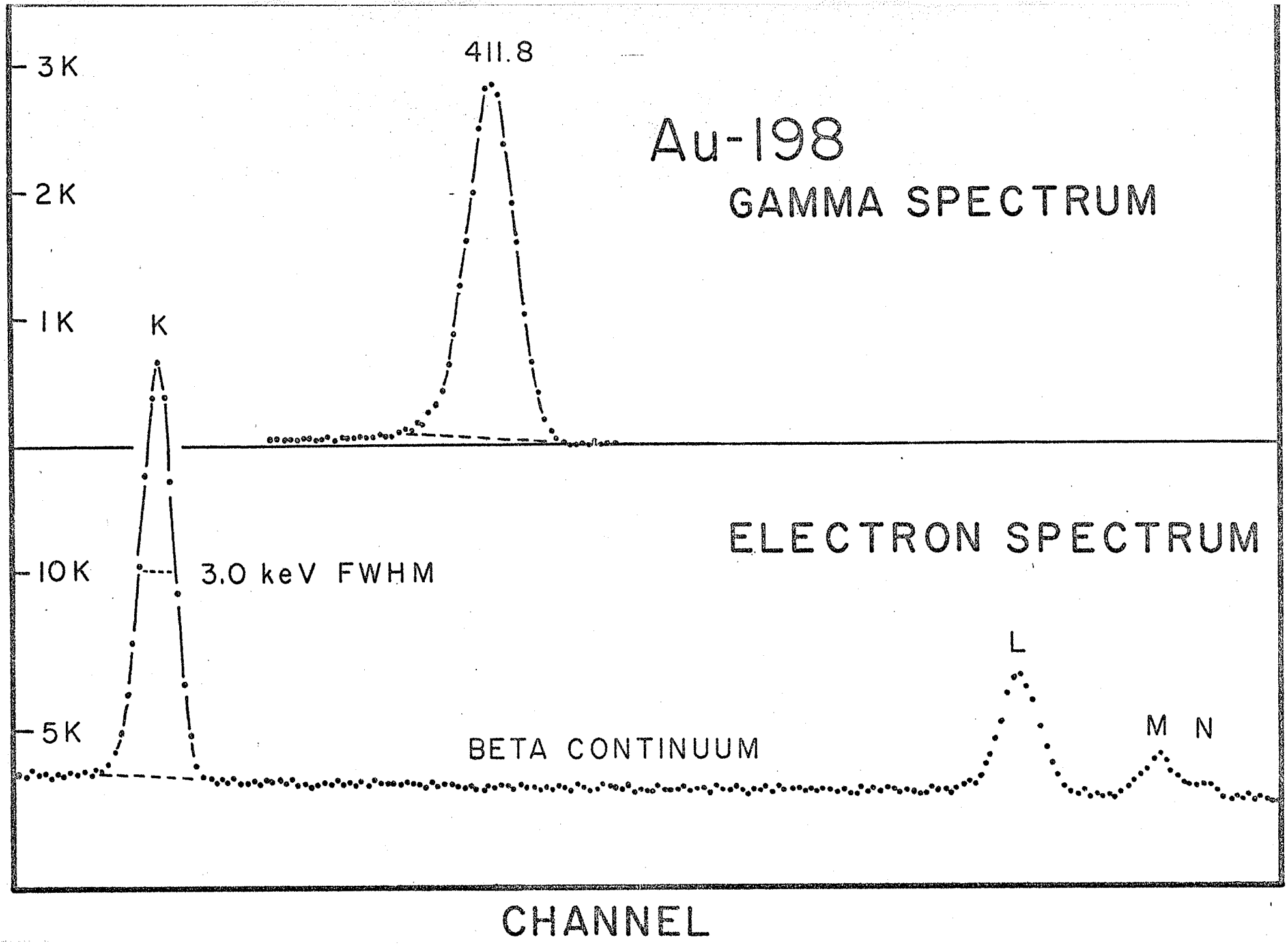
411.8
3K
2K
1K
K
Au-198
GAMMA SPECTRUM
ELECTRON SPECTRUM
10K
3.0 keV FWHM
5K
BETA CONTINUUM
L
M N
CHANNEL

isotope.

An active source of 6.24d Bi^{206} was produced in the internal beam of the University of Manitoba cyclotron. The techniques used were essentially the same as those for production of Hg^{195} sources and the reader is referred to Chapter III for details of target making, vacuum sublimation of the activity, etc.

The target consisted of about 400 mg of natural lead foil (20 thousandths of an inch thick). The proton bombarding energy was 17.5 MeV, the beam current as measured on the target holder about 3 μAmps, and the total irradiation time was two hours. The three major isotopic constituents of lead are:

Pb^{206} 23.6%

Pb^{207} 22.6%

Pb^{208} 52.3%

The threshold for (p, 2n) reactions on these nuclei is about 11 MeV so at 17.5 MeV one expects to excite 15.3d Bi^{205} from Pb^{206} and 6.24d Bi^{206} from Pb^{207}. The other activities accessible from (p, 2n) or (p, n) reactions are too long-lived to be excited in so short an irradiation time to any appreciable extent.

In fact a rather pure Bi^{206} source was obtained indicating the dominance of the reaction

Pb^{207} (p, 2n) Bi^{206} at this energy.

An electron spectrum of this activity is shown in Fig. 2.7. The K-conversion lines identified in the figure are those used as the relative intensity standards. Other lines were available, but were not made use of either because of incomplete resolution from neighbouring lines or interference from Bi^{205} contaminant.

Table 2.4 summarizes the efficiency data obtained from six lines in Bi^{206}. The efficiencies have been normalized to the graph of the data of Table 3.2 for comparison and it will be seen that the normalized efficiencies obtained from Stockendal's data are in good agreement with Table 2.2.

TABLE 2.4 Bi^{206} EFFICIENCY DATA

E_e(keV)	I_e (Stockendal)	Eff (normalized)
255.4	760	1.34×10^{-2}
310.1	210	1.26×10^{-2}
409.1	170	1.22×10^{-2}
428.1	250	1.24×10^{-2}
449.5	280	1.29×10^{-2}
715.3	100	1.23×10^{-2}

In Fig. 2.8 is shown the final efficiency curve for the Si(Li) detector. The circles indicate points obtained from the I.C.C. standards and the squares the Bi^{206} data. There would appear to be a slight decrease in efficiency below about 100 keV. This may merely reflect the uncertainty of the Ge(Li) calibration curve in this energy region. In all the I.C.C.

Figure 2.7

"Electron spectrum of Bi^{206} produced by proton irradiation of natural lead at 17.5 MeV."

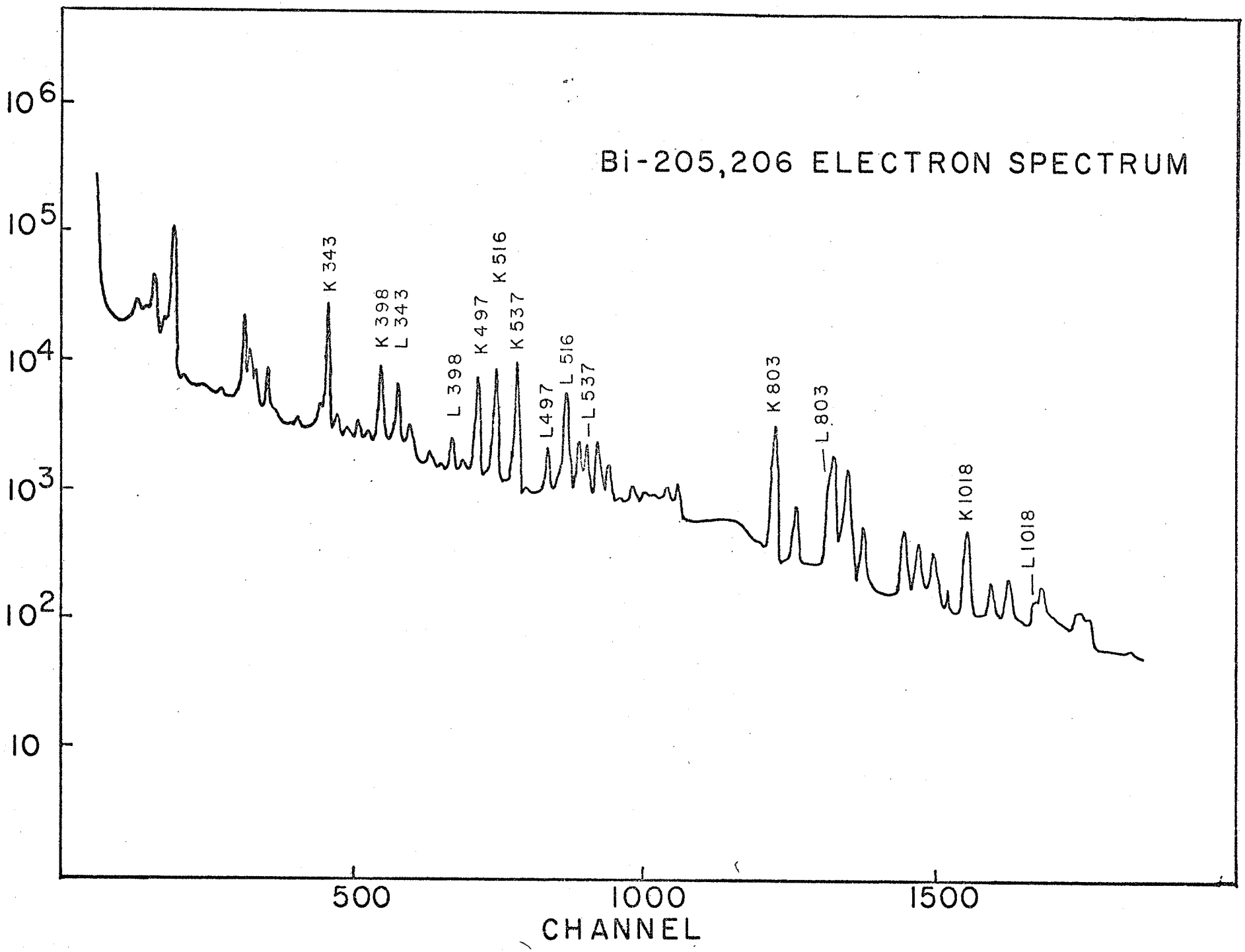
Bi-205,206 ELECTRON SPECTRUM
10^6
10^5
10^4
10^3
10^2
10
K 343
K 398
L 343
L 398
K 497
K 516
K 537
L 497
L 516
L 537
K 803
L 803
K 1018
L 1018
500
1000
1500
CHANNEL

Figure 2.8

"Full energy efficiency of Si(Li) detector."

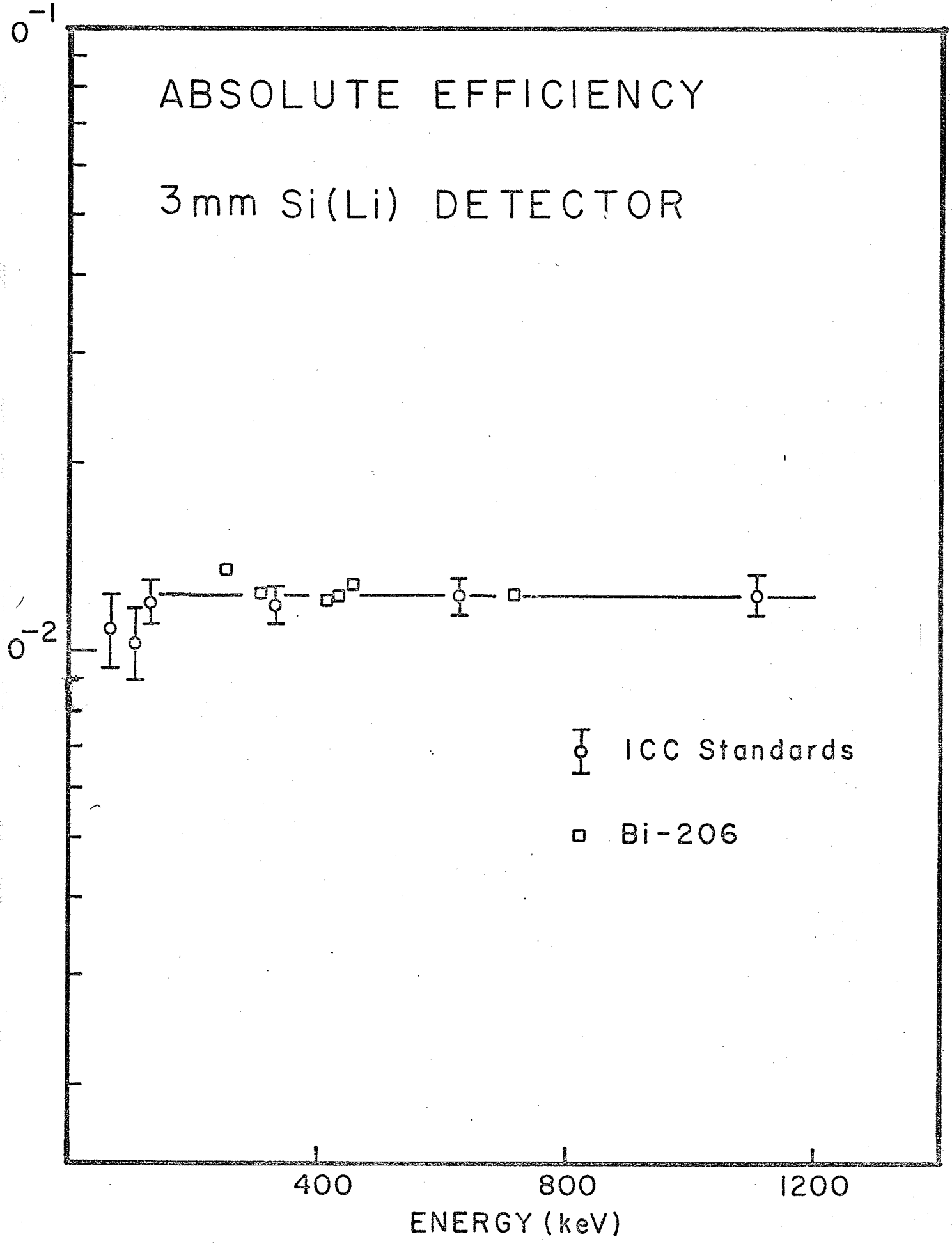
ABSOLUTE EFFICIENCY
3mm Si(Li) DETECTOR
10^{-1}
10^{-2}
ICC Standards
Bi-206
400
800
1200
ENERGY (keV)

measurements made in this work a Si(Li) detector efficiency of $1.23 \times 10^{-2} \pm 5\%$ has been assumed. These measurements involve electron lines from 100 to 1200 keV, but only three of them (lines in Hg^{195}) fall below 200 keV.

(v) Some Absolute I.C.C. Measurements

As a final check on the reliability of this spectrometer, α_K and α_L measurements were made on Bi^{206} and Bi^{207}.

Stockendal[2], in addition to measuring electron relative intensities, obtained α_K for 11 prominent transitions following the decay of Bi^{206} by the internal-external conversion method. Seven of these were measured in the present work and are compared with Stockendal's values in Table 2.5. The agreement is well within quoted experimental errors in all cases.

TABLE 2.5 α_K MEASUREMENTS IN Bi^{206}

E_γ (keV)	α_K	
	Present Work	Stockendal et al.
343	0.24 ± 0.02	0.25 ± 0.03
398	0.16 ± 0.02	0.18 ± 0.02
497	0.090 ± 0.01	0.081 ± 0.015
516	0.047 ± 0.005	0.047 ± 0.005
537	0.073 ± 0.007	0.070 ± 0.008
803	0.0080 ± 0.0008	0.0086 ± 0.0009
1018	0.0133 ± 0.001	0.016 ± 0.008

K and L shell internal conversion coefficients were measured for the two strong lines in Bi^{207} at 570 keV and 1064 keV. The results are presented in Table 2.6 where they are compared with the theoretical values of Sliv and Band and of Hager and Seltzer as well as with the results of two recent experimental determinations.

TABLE 2.6 I.C.C. MEASUREMENTS IN Bi^{207}

	PRESENT WORK	THEORY(a)	THEORY(b)	EXPERIMENT(c)	EXPERIMENT(d
E = 570 keV (E2)					
α_K	0.0161 ± 0.0016	0.0159	0.0158	0.016 ± 0.001	0.0156 ± 0.00
α_L	0.0045 ± 0.005	0.0045	0.0045	0.0049 ± 0.0005	0.0045 ± 0.00
E = 1064 keV (M4)					
α_K	0.096 ± 0.01	0.095	0.098	0.085 ± 0.005	0.084
α_L	0.024 ± 0.002	0.024	0.025	0.023 ± 0.002	—

(a) Sliv and Band, ref. [2] Chapter IV

(b) Hager and Seltzer, ref. [3] Chapter IV

(c) Ref. [3]

(d) Ref. [4]

Here again there is good agreement with previous measurements. The theoretical values were obtained assuming the 570 keV transition to be pure E2 and the 1064 transition to be pure M4. The present work would seem to confirm such an assignment. (Sen (ref. 3) suggests that their value for α_K (1064 keV), which is somewhat lower than the present measurement, might suggest a small E5 admixture.)

REFERENCES, CHAPTER II

1. J. M. Hollander, in Proceedings of International Conference on the Internal Conversion Process, Ed. J. H. Hamilton, Academic Press, 1965.

2. R. Stockendal and S. Hultberg, Ark. Fys. 15, 33 (1959).

3. S. K. Sen and S. I. H. Rizvi, Nucl. Instr. and Meth. 2, 227 (1967).

4. V. Andersen and C. J. Christensen, Nuclear Physics A113, 81 (1968).

CHAPTER III

THE GAMMA SPECTRUM OF $Hg^{195,195m}$

Introduction

The presently accepted level scheme of Au^{195} [1] is shown in Fig. 3.1. This scheme is based primarily on the work of Brunner et al.[2] and Joly et al.[3] who examined the decay of Hg^{195} and Hg^{195m} with magnetic electron spectrometers and NaI gamma spectrometers in both singles and coincidence configurations. More recently Frank[4] examined the gamma spectrum with a Ge(Li) detector and postulated three new transitions in Au^{195}.

This chapter describes the gamma ray measurements intended to check the validity of this decay scheme and, where necessary, to extend or amend it. Because of the continued improvement in resolution and efficiency of Ge(Li) detectors and having regard to the complicated nature of the decay, we might reasonably expect some new information, and certainly better values for gamma intensities and electron capture branching ratios.

(i) Source Preparation

Active sources of 9.5 hr Hg^{195} and 40 hr Hg^{195m} were prepared by proton irradiation of targets in the internal beam of the University of Manitoba cyclotron. This accelerator produces a maximum proton energy of 50 MeV with an internal beam current (H^- ions) of, typically, a few μAmps. Natural

Figure 3.1

"Level scheme of Au^{195}, after Lederer et al.[1]"

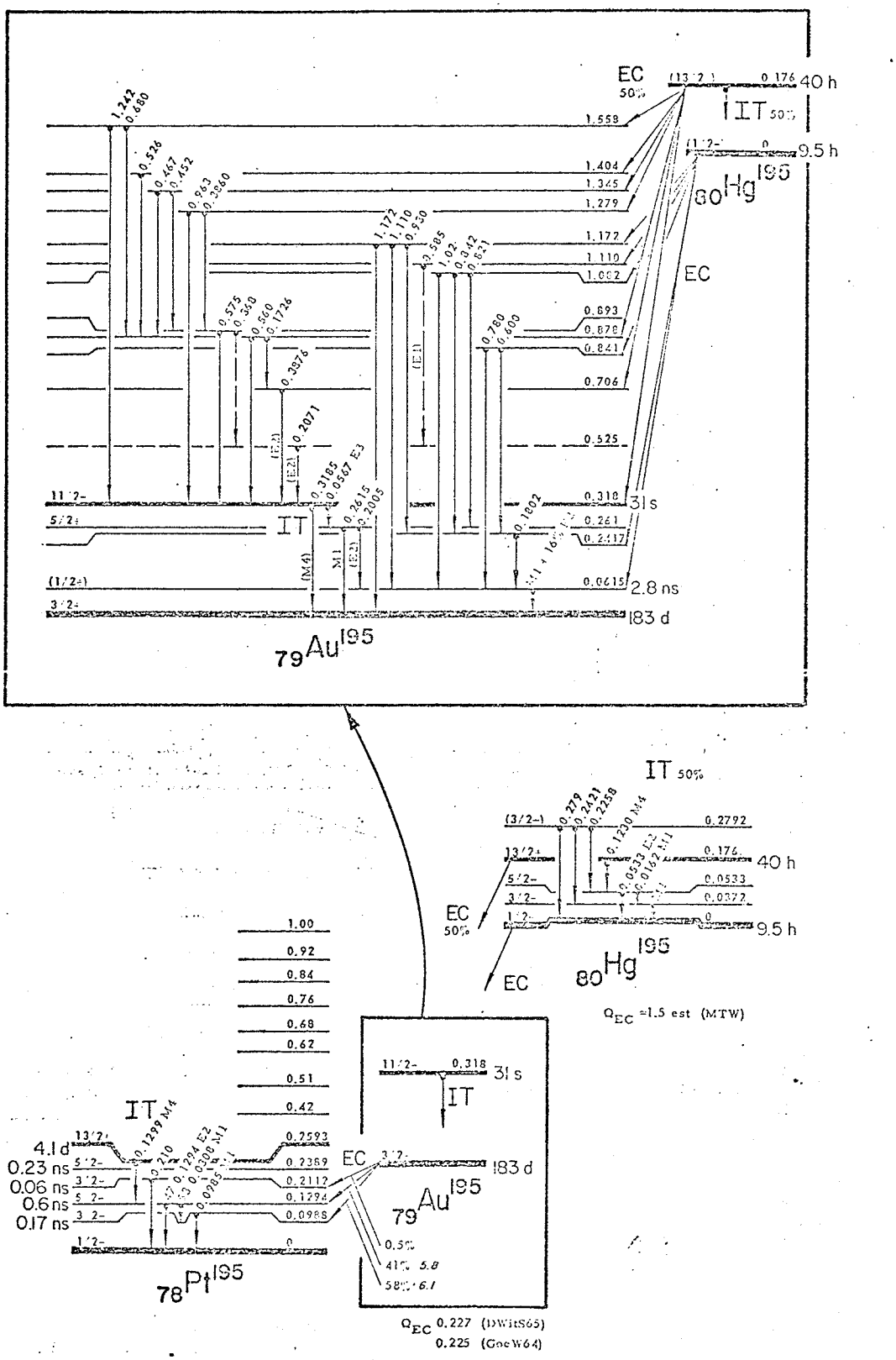
EC
50%
IT 50%
40 h
9.5 h
80Hg195
EC
1.558
1.404
1.345
1.279
1.177
1.110
1.002
0.893
0.870
0.841
0.706
0.525
0.318
31 s
0.261
0.2417
0.0615
2.8 ns
183 d
IT
79Au195
IT 50%
40 h
9.5 h
EC
50%
EC
80Hg195
QEC =1.5 est (MTW)
1.00
0.92
0.84
0.76
0.68
0.62
0.51
0.42
IT
4.1 d
0.23 ns
0.06 ns
0.6 ns
0.17 ns
0.7593
0.7369
0.2112
0.1294
0.0988
0
78Pt195
EC
183 d
79Au195
0.5%
41% 5.8
58% 6.1
QEC 0.227 (DWitS65)
0.225 (GoeW64)

gold targets (>99% pure) in the form of thin wire wrapped in aluminum foil envelopes were used. Since gold is monoisotopic (A=197), the reaction of interest is

$$Au^{197}(p, 3n)\ Hg^{195,195m}$$

Table 3.1 lists threshold energies for (p, xn) reactions on Au^{197} as calculated from the mass tables of Wapstra et al.[5].

TABLE 3.1 REACTION THRESHOLDS

REACTION	THRESHOLD ENERGY (MeV)	PRODUCT NUCLIDE
p, n	1.54	65 hr Hg^{197}, 24 hr Hg^{197m}
p, 2n	8.18	STABLE Hg^{196}
p, 3n	17.00	9.5 hr Hg^{195}, 40 hr Hg^{195m}
p, 4n	24.30	1.9 y Hg^{194}

Reactions of the type (p, pxn) produce gold activities (especially 6.18d Au^{196}) which are eliminated in source preparation by the sublimation process (described below). The (p, α) reaction produces stable Pt^{194}.

Most of the irradiations were done at 25 MeV since the (p, 3n) cross section is expected to be large at this energy. Degradation of the proton beam energy in the gold wire (about 0.040" in diameter) resulted in the production of some Hg^{197}. However the decay of this isotope has been well studied and is fairly simple so this contamination did not prove an inconvenience.

Active sources with strengths of the order of a few μCur were prepared by sublimation in vacuum onto thin aluminum backings (0.001" thick). Besides producing very thin sources

suitable for both gamma ray and electron studies, this method also effectively separated the Hg activity from the Au carrier, the mercury being distilled off at a relatively low temperature. While considerable Au^{196} contamination was evident in the irradiated gold targets, no trace of this activity was found in the sublimed sources. Fig. 3.2 shows the sublimation apparatus. The filament is a strip of 0.005" thick tantalum. The source size is defined by an aluminum mask with a central hole 3 mm in diameter.

Because of its high vapour pressure, mercury has the unpleasant habit of diffusing under high vacuum at room temperature. To avoid contamination of the electron detector and erroneous values for internal conversion coefficients which would result it was necessary to cover all sublimed electron sources with VYNS film (about 20 μgm/cm^2 thickness). Fortunately no deterioration in electron line shape resulted, even down to 50 keV energy, and the mercury sources were rendered immobile.

(ii) The Gamma Ray Spectrum

The gamma spectrum of $Hg^{195,195m}$ is a rich one, as can be seen from Fig. 3.3. This spectrum was taken with the 35 cc Ge(Li) detector from a sublimed source, 94 hours after irradiation with 25 MeV protons. The counting time was 105 minutes. Of the lines seen in this spectrum, the following ones can be indentified as impurities from their energies and/or decay properties:

Figure 3.2

"Apparatus for vacuum sublimation of sources."

SUBLIMATION CHAMBER

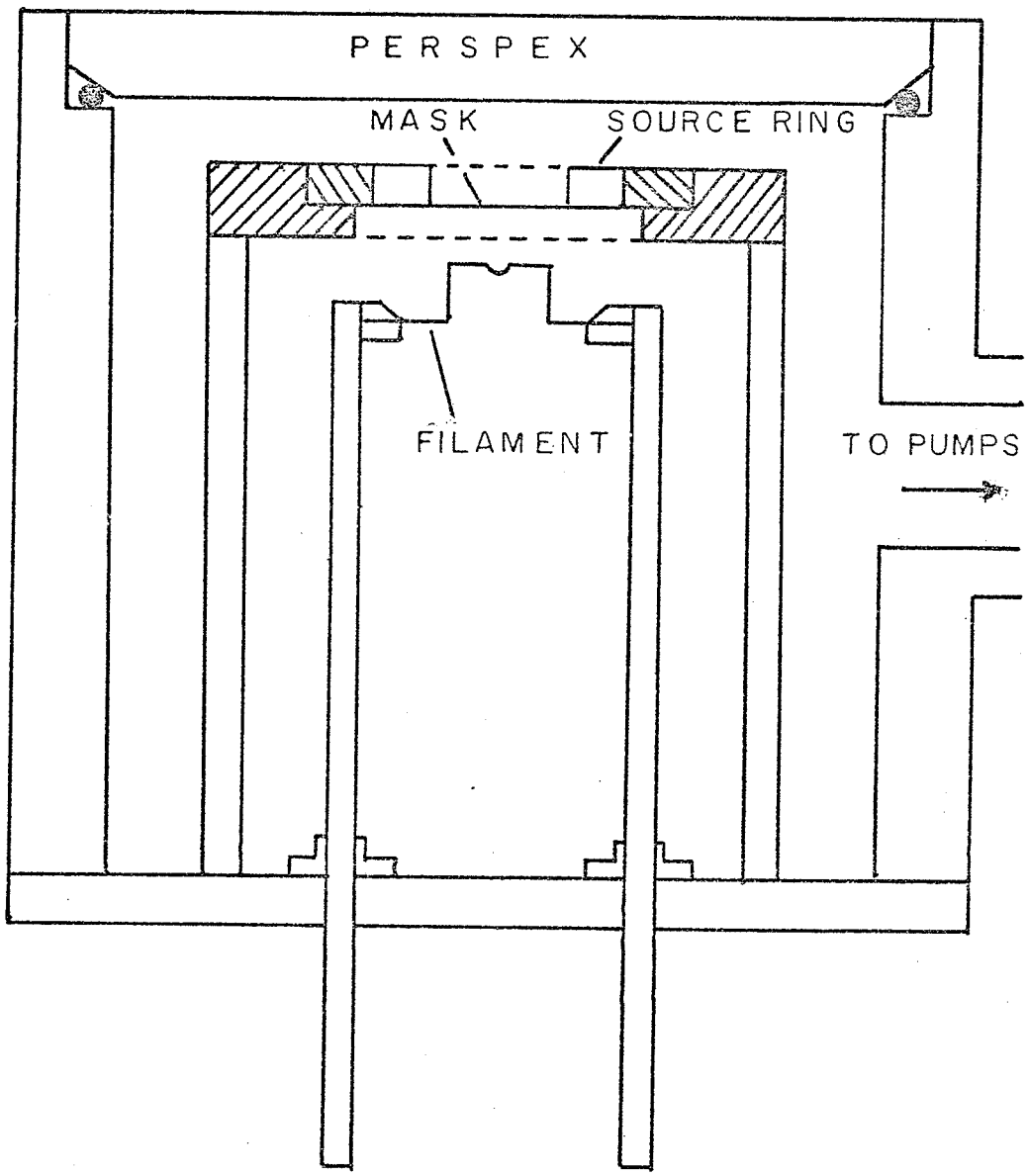

Figure 3.3

"The gamma ray spectrum of $Hg^{195,195m}$ above 130 keV as seen with the ORTEC 35 cc Ge(Li) detector. Energies are in keV. The proton bombarding energy was 25 MeV."

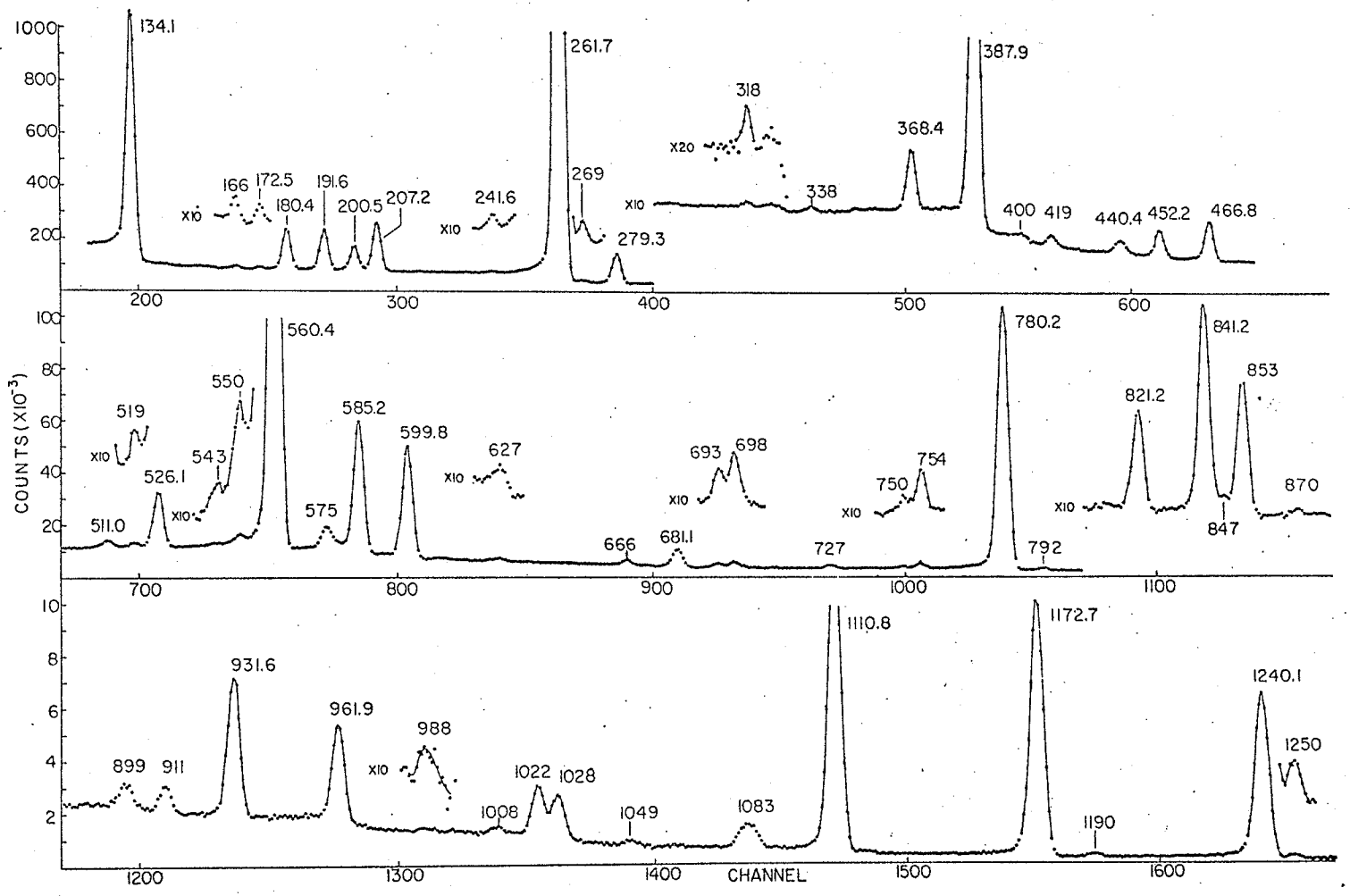
COUNTS (X10⁻³)
CHANNEL
134.1
166
172.5
180.4
191.6
200.5
207.2
241.6
261.7
269
279.3
318
338
368.4
387.9
400
419
440.4
452.2
466.8
511.0
519
526.1
543
550
560.4
575
585.2
599.8
627
666
681.1
693
698
727
750
754
780.2
792
821.2
841.2
847
853
870
899
911
931.6
961.9
988
1008
1022
1028
1049
1083
1110.8
1172.7
1190
1240.1
1250
X10
X20

Figure 3.4

"The gamma ray spectrum of $Hg^{195,195m}$ below 270 keV as seen with the ORTEC 0.25 cc X-ray spectrometer. Unidentified impurities are marked 'I'. Energies are in keV. The proton bombarding energy was 40 MeV."

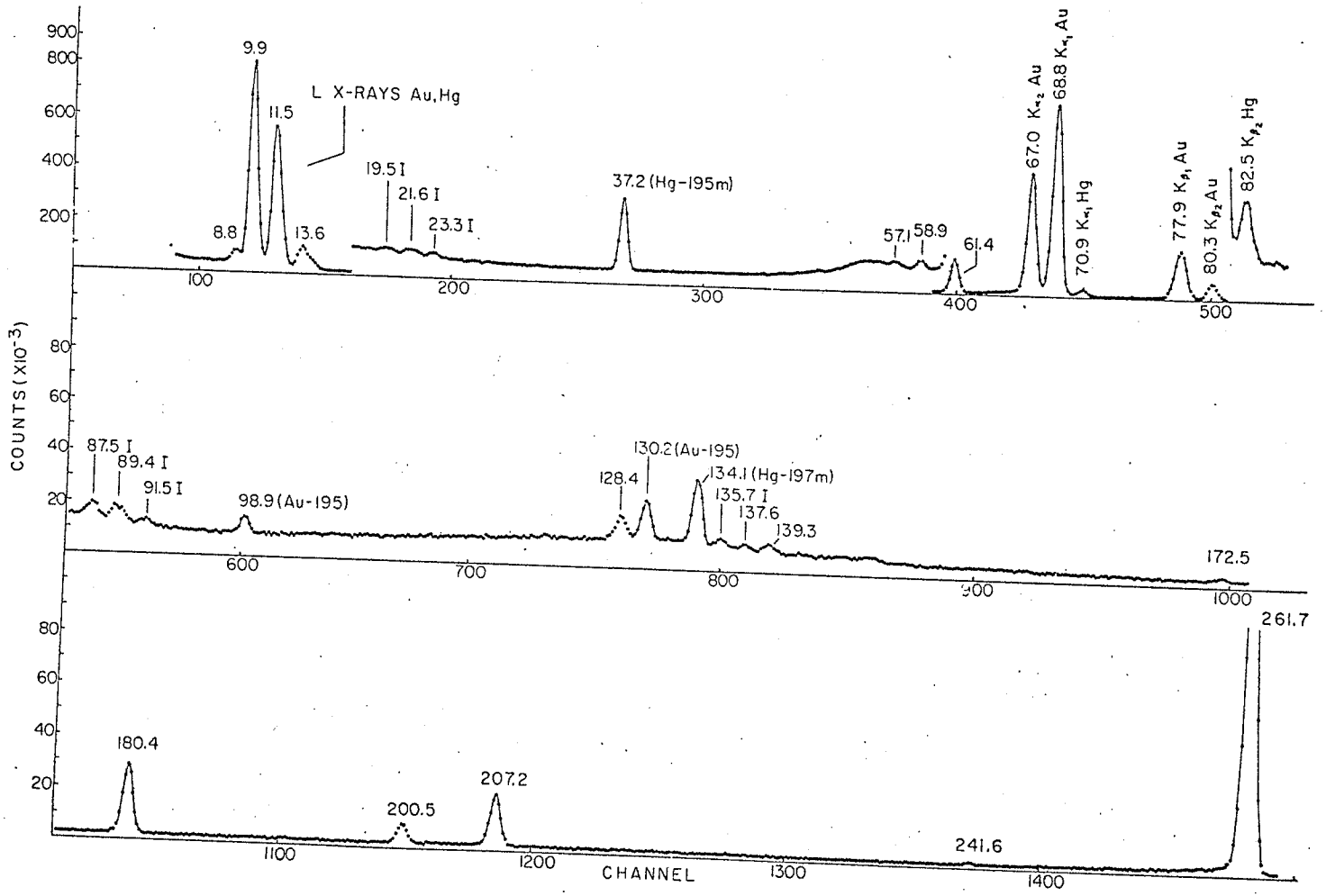
COUNTS (X10⁻³)
CHANNEL
L X-RAYS Au, Hg
8.8
9.9
11.5
13.6
19.5 I
21.6 I
23.3 I
37.2 (Hg-195m)
57.1
58.9
61.4
67.0 Kα2 Au
68.8 Kα1 Au
70.9 Kα1 Hg
77.9 Kβ1 Au
80.3 Kβ2 Au
82.5 Kβ2 Hg
87.5 I
89.4 I
91.5 I
98.9 (Au-195)
128.4
130.2 (Au-195)
134.1 (Hg-197m)
135.7 I
137.6
139.3
172.5
180.4
200.5
207.2
241.6
261.7

134 keV following the decay of Hg^{197m}

166 keV following the decay of Hg^{197m}

191.6 keV following the decay of Hg^{197}

279.3 keV following the decay of Hg^{197m}

1190 keV origin unknown.

Of the remaining lines, all of which were observed to decay at a rate consistent with that of known radiations from $Hg^{195,195m}$ twenty-three have been hitherto unreported: 241.6, 338, 400, 419, 440.4, 519, 543, 550, 627, 666, 693, 727, 750, 792, 847, 870, 899, 911, 1008, 1028, 1049, 1083 and 1250 keV. The existence of radiations at 698, 754, and 853 keV first reported by Frank[4] is confirmed in the present work although the first two of these gamma rays are actually seen to be members of 2 partially resolved doublets.

Fig. 3.4 displays the low energy part of the gamma spectrum as observed with the 0.25 cm^3 Be-window detector. A bombarding energy of 40 MeV was chosen so as to eliminate as much as possible the $Hg^{197,197m}$ impurities. The L and K X-rays of mercury and gold are clearly visible. The strong 134 keV transition from Hg^{197m} is still evident although considerably reduced in intensity relative to the Hg^{195} gamma rays. The lines labelled "I" were identified as impurities either from their decay rates when found to be inconsistent with a $Hg^{195,195m}$ assignment or because of their absence from similar spectra

from lower energy irradiations. Their origin remains unknown. Other obvious impurities are identified in the figure. Of the remaining lines, those hitherto unreported which may be candidates for the Au^{195} level scheme are the following: 58.9, 128.4, 137.6, and 139.3 keV.

Not only is the spectrum of this isotope complex, but so is its mode of decay. In Fig. 3.1 it is seen that the 40 hour state decays through two competing channels--isomeric cascades to the ground state followed by electron capture transitions to excited states in Au^{195}, or direct electron capture decay to states in Au^{195}. Since the spin of the isomeric state differs so greatly from that of the ground state, it is expected that those electron capture decays depopulating the 9.5 hour ground state will feed levels of low spin in Au^{195}, while similar decays depopulating the 40 hour isomeric state will feed levels of high spin. Moreover, because of the gamma transition selection rules, we might expect a minimum of interference between the two resulting sets of transitions in Au^{195}. To put it another way, we expect most of the Au^{195} gamma rays to decay at the same rate as Hg^{195m} which has a simple 40 hour half life, or at the same rate as Hg^{195} which is in transient equilibrium with the isomeric state.

The situation is illustrated in Fig. 3.5 where the intensities of three prominent gamma rays are plotted vs. time. Their intensities have all been normalized at $t = 0$ (which

Figure 3.5

"Decay characteristics of some representative gamma rays following the decay of $Hg^{195,195m}$."

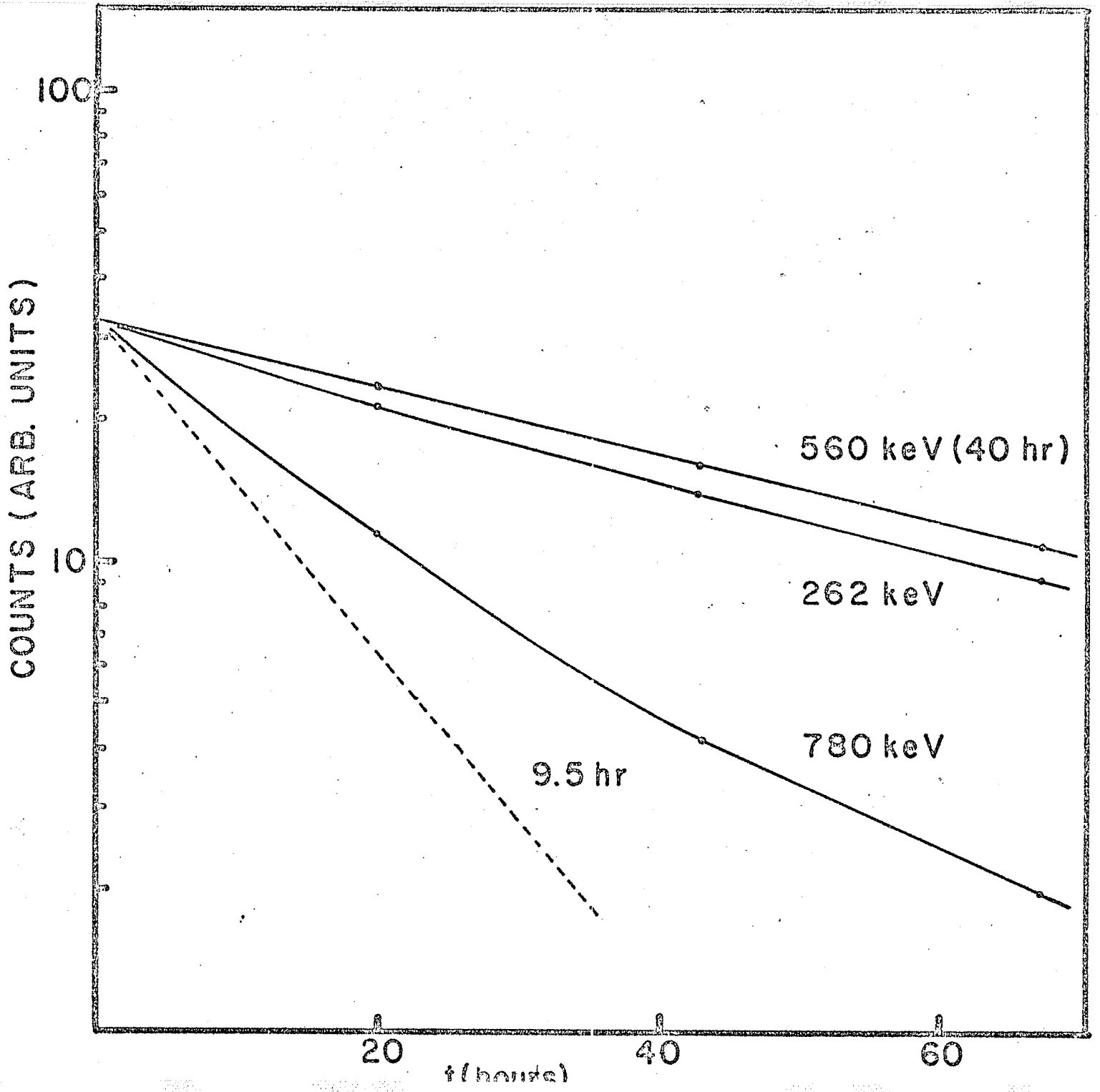
100
10
COUNTS (ARB. UNITS)
560 keV (40 hr)
262 keV
780 keV
9.5 hr
20
40
60
t (hours)

actually corresponded to 75 minutes after irradiation). It is evident that, if the decay scheme of Fig. 3.1 is correct, the 560 keV photopeak must follow the electron capture decay of the 40 hour isomeric state only and hence have a simple exponential decay. This is in fact observed. Similarly the 780 keV line should follow the decay of the Hg^{195} ground state and its behaviour is seen to be consistent with this. Indeed almost all the gamma rays had decay curves with the same shape as one or the other of these two representatives and, depending upon which shape they exhibited, had their relative intensities normalized to either the 560 keV line or the 780 keV line. In this way the two decay modes could be treated effectively independent of one another for the purpose of working out population balances and branching ratios.

The only complication to this method of analysis arises when one considers gamma rays depopulating the 262 keV level. It is clear from Fig. 3.1 that this level is populated appreciably by gamma rays which follow the decay of both parent states, and possibly even by direct electron capture from the Hg^{195} ground state. Hence the 261.7 and 200.5 keV lines should exhibit a behaviour intermediate between the two representative cases discussed above. This effect is shown in Fig. 3.5 for the 261.7 keV line. The question now arises: at a given time after irradiation, what fraction of 261.7 keV (or 200.5 keV) gammas follows the decay of Hg^{195} as opposed to

Hg^{195m}? This problem is discussed in detail in Appendix I of this thesis where a simple least squares comparison of the shapes of the decay curves involved is used to compute the relative contributions of the two decays at a given time. The results are as follows: At t = 0 (75 minutes after irradiation) (14 ± 2)% of the 261.7 keV gammas and (12 ± 15)% of the 200.5 keV gammas resulted from parent ground state decays. The large error for the 200.5 keV transition is due to the fact that the spectrometer used was not able to resolve completely that gamma ray from the 207 keV line. Since its intensity is relatively small, this error did not seriously affect the decay scheme calculations. Moreover, since the two lines depopulate the same level, the admixtures should be identical and were taken as such.

(iii) Energy and Relative Intensity Measurements

The techniques of energy and efficiency calibration used in this study were discussed in detail in Chapter I. Gamma ray energy and intensity measurements were made with all four available gamma spectrometers and the results are presented in Table 3.2. This table lists all the gamma rays which have been placed (tentatively or with confidence) in the electron capture decay scheme of $Hg^{195,195m}$ grouped according to their decay characteristics as discussed in section (ii). The energies (column 1) quoted to 0.1 keV are believed accurate to ± 0.3 keV and those listed to 1 keV are accurate to ± 1 keV. The subsequent

TABLE 3.2 RELATIVE PHOTON INTENSITIES

E_γ	RUN 1	RUN 2	RUN 3	RUN 4	RUN 5	RUN 6	RUN 7	RUN 8	RUN 9	RUN 10	MEAN
9.5 hr											
61.4								84.7			85±9
128.4											
139.3											
180.4	30.6	25.1	30.9		29.1		29.4	28.4			28.9±2.6
200.5			0.6(a)								0.6±0.1
207.2	33.0	28.0	31.5		26.8		29.4				29.7±2.2
241.6	1.0	1.3					1.2			1.1	1.2±0.1
261.7			25(a)								25±3.5
585.2	29.6	28.0	33.3		27.9	30.9					29.9±2.0
599.8	26.3	21.8	26.2		27.3	25.5			26.5	26.6	25.7±0.9
780.2	100	100	100	100	100	100	100	100	100	100	100
821.2	3.1	3.0	3.0		3.4	3.5					3.2±0.2
841.2	7.2	7.2	7.8		8.1	8.2					7.7±0.4
911		0.6		0.7							0.7±0.1
931.6	4.2	5.6	6.5	6.7	6.3	6.7					6.0±0.9
988									0.2		0.2±0.1
1008									0.3		0.3±0.1
1022									2.8	2.9	2.9±0.3
1049				0.3						0.2	0.3±0.1
1083		1.1		1.3						1.1	1.2±0.1
1110.8	17.8	16.9	21.2	21.0	16.9	17.7				20.4	18.8±1.9
1172.9	20.3	17.6	22.1	21.2	17.1	16.8					19.2±2.1
1250									0.2		0.2±0.1
40 hr											
172.5							0.7				0.7±0.4
200.5			13.3(a)								13.3±1.7
261.7			485(a)								485±68
279											
318									0.2		0.2±0.1
368.4	4.0	5.2			4.9	5.6					4.9±0.7
387.9(b)	30.6	34.2			29.2	30.5					31.1±1.9
452.2	2.5	2.6			2.7	2.2					2.5±0.2
466.8	3.3	3.8			2.9	4.9					3.7±0.7
526.1	6.1	6.5			7.3	6.8					6.7±0.4
560.4	100	100	100	100	100	100	100	100	100	100	100
575		4.9									4.9±0.5
627									0.5		0.5±0.2
665									0.6	0.7	0.7±0.3
693									0.7		0.7±0.3
698									1.1	0.9	1.0±0.5
681.1	3.4	2.7		2.5							2.9±0.3
727									0.6	0.8	0.7±0.1

TABLE 3.2 (CONTINUED)

E_γ	RUN 1	RUN 2	RUN 3	RUN 4	RUN 5	RUN 6	RUN 7	RUN 8	RUN 9	RUN 10	MEAN
752									0.3		0.3±0.1
754				0.7					0.9	0.9	0.9±0.1
853		3.4		4.1							3.8±0.4
898									0.8	0.8	0.8±0.1
961.9	2.4	3.1		3.0		3.0			3.0	3.1	2.9±0.2
1028									1.6	1.6	1.6±0.2
1240.1	7.1	7.4		8.4	8.1	6.5					7.5±0.7

(a) As obtained from least squares analysis, Appendix II

(b) Doublet

4 mm Nuclear Diodes detector Runs 1, 5, 6, 7

0.25 cc ORTEC detector Run 8

25 cc Princeton Gamma Tech detector Runs 2, 3, 4

35 cc ORTEC detector Runs 9, 10

TABLE 3.3 COMPARISON WITH PREVIOUS WORK

E_γ (keV)	I_γ PRESENT WORK	I_γ FRANK
9.5 hr		
61.4	85±9	86
180.4	28.9±2.6	33
200.5	0.6±0.1	0.7
207.2	29.7±2.2	28.5
241.6	1.2±0.1	
261.7	25±3.5	28.5
585.2	29.9±2.0	37.7
599.8	25.7±0.9	28.6
780.2	100	100
821.2	3.2±0.2	4.8
841.2	7.7±0.4	11.5
911	0.7±0.1	
931.6	6.0±0.9	6.5
988	0.2±0.1	
1008	0.3±0.1	
1022.4	2.9±0.3	3.0
1049	0.3±0.1	
1083	1.2±0.1	
1110.8	18.8±1.9	18.2
1172.9	19.2±2.1	16.9
1250	0.2±0.1	
40 hr		
172.5	0.7±0.4	<6.0
200.5	13.3±1.7	9.8
261.7	485±68	392
368.4	4.9±0.7	7.6
387.9	31.1±1.9	27
452.2	2.5±0.2	4.9
466.8	3.7±0.7	8.9
526.1	6.7±0.4	4.1
560.4	100	100
575	4.9±0.5	9.0
627	0.5±0.2	
665	0.7±0.3	
693	0.7±0.3	
698	1.0±0.5	
681.1	2.9±0.3	2.7
727	0.7±0.1	
752	0.3±0.1	
754	0.9±0.1	1.7
853	3.8±0.4	5.0
898	0.8±0.1	
961.9	2.9±0.2	1.8
1028	1.6±0.2	
1240	7.5±0.7	7.0

columns show the relative photopeak intensities as obtained in 10 independent runs and normalized to the 780 keV photopeak or the 560 keV photopeak depending on their decay properties. The last column gives the mean of the various runs, along with the estimated error. Where more than three runs are available for comparison the errors are RMS deviations. Otherwise an error of ± 10% was assigned if the photopeak was well defined statistically (e.g. the 61.4 keV peak) and ± 50% it if was not.

Table 3.3 summarizes the relative photon intensity data and compares it with the results of Frank[4] whose work constitutes the only previous extensive measurements of photon intensities in this decay.

(iv) Gamma-Gamma Coincidence Studies

Coincidence work was undertaken for two reasons:

(a) To verify the general level structure of Fig. 3.1 before undertaking spin-parity assignments and model comparison.

(b) To aid in the placing of newly discovered gamma rays.

The solid state gamma-gamma coincidence spectrometer described in the first chapter was used for this purpose. Vacuum sublimed sources were prepared in the usual way and the counting geometry was essentially that of Fig. 1.5. The energy windows selected for coincidence study are shown superimposed on the 35 cc Ge(Li) gamma spectrum of Fig. 3.6. As can be seen, wherever possible a coincidence spectrum gated by the

Figure 3.6

"Portion of $Hg^{195,195m}$ gamma ray singles spectrum showing energy windows selected for coincidence gating."

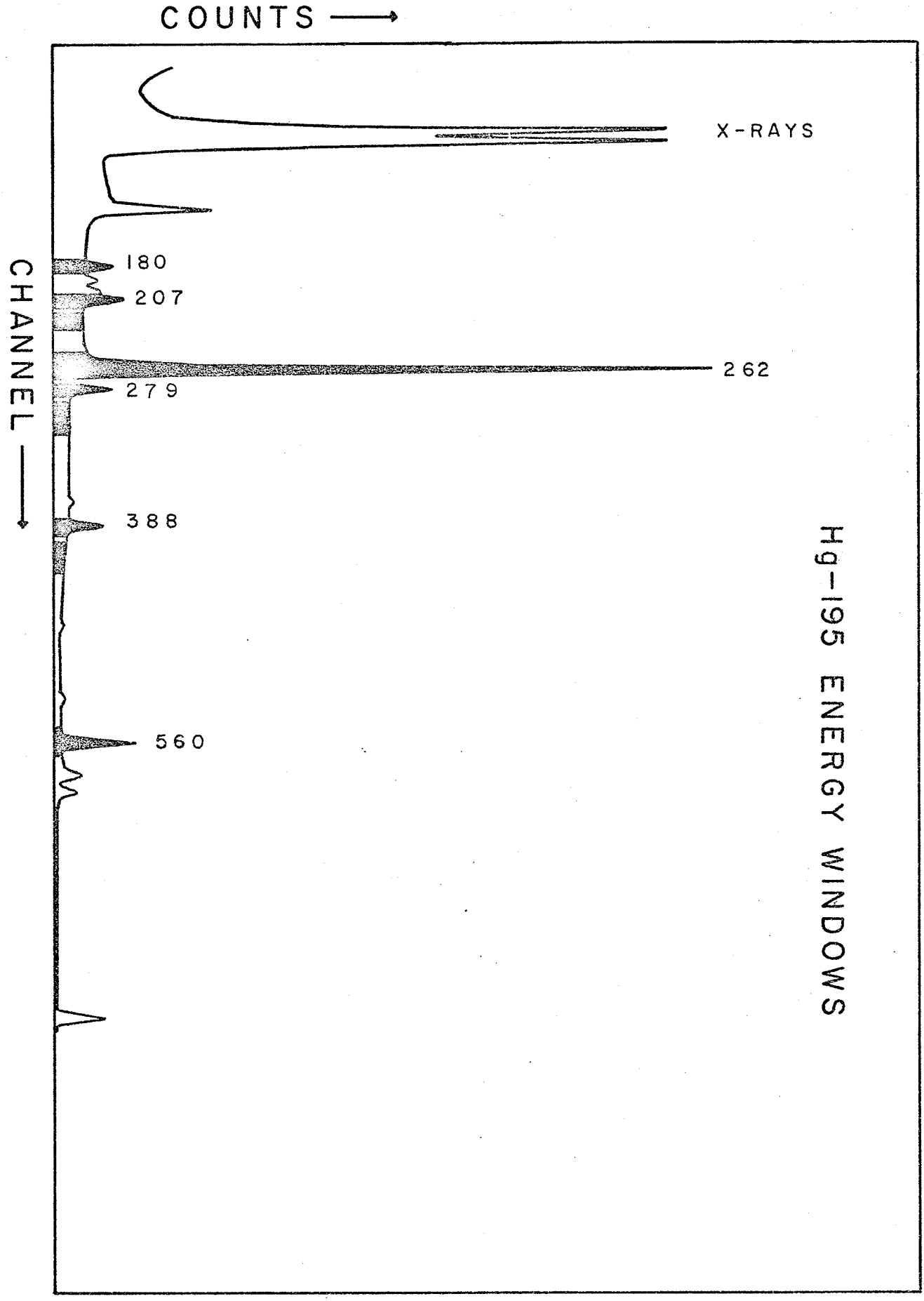
COUNTS
X-RAYS
180
207
262
279
388
560
CHANNEL
Hg-195 ENERGY WINDOWS

compton continuum directly above each chosen photopeak was also run, so as to be able to distinguish between true coincidence lines and those due to the underlying compton background. No attempt was made at quantitative comparison of two such spectra because the various experiments were run sequentially and the complicated nature of the decay (discussed earlier in this chapter) precluded any such comparisons. Nevertheless the sought for information was obtained by scanning the spectra obtained.

In Figures 3.7(a)-3.7(i) are presented the various coincidence spectra. In order to indicate how they were analyzed, we shall discuss the interpretation of Fig. 3.7(a) and afterwards merely present the conclusions drawn from succeeding spectra without going into details. In this figure we see displayed the spectrum of gamma rays in coincidence with the 180 keV photopeak. This figure should be compared with Fig. 3.7(c) which corresponds to a window set on the compton continuum above 207 keV. Since there is no reason to expect the existence of another 180 keV gamma ray in coincidence with the one depopulating the 242 keV level we can attribute its presence in Fig. 3.7(a) to compton events within the pre-set window. Indeed both the 180 keV and 207 keV lines dominate the compton coincidence spectrum of Fig. 3.7(c) (and all subsequent compton coincidence spectra). The intensity of the 180 keV line may therefore be taken as a rough means of

Figure 3.7

"Coincidence spectra obtained with 20 cc Ge(Li) and 35 cc Ge(Li) detector systems.

(a) With 180 keV photopeak

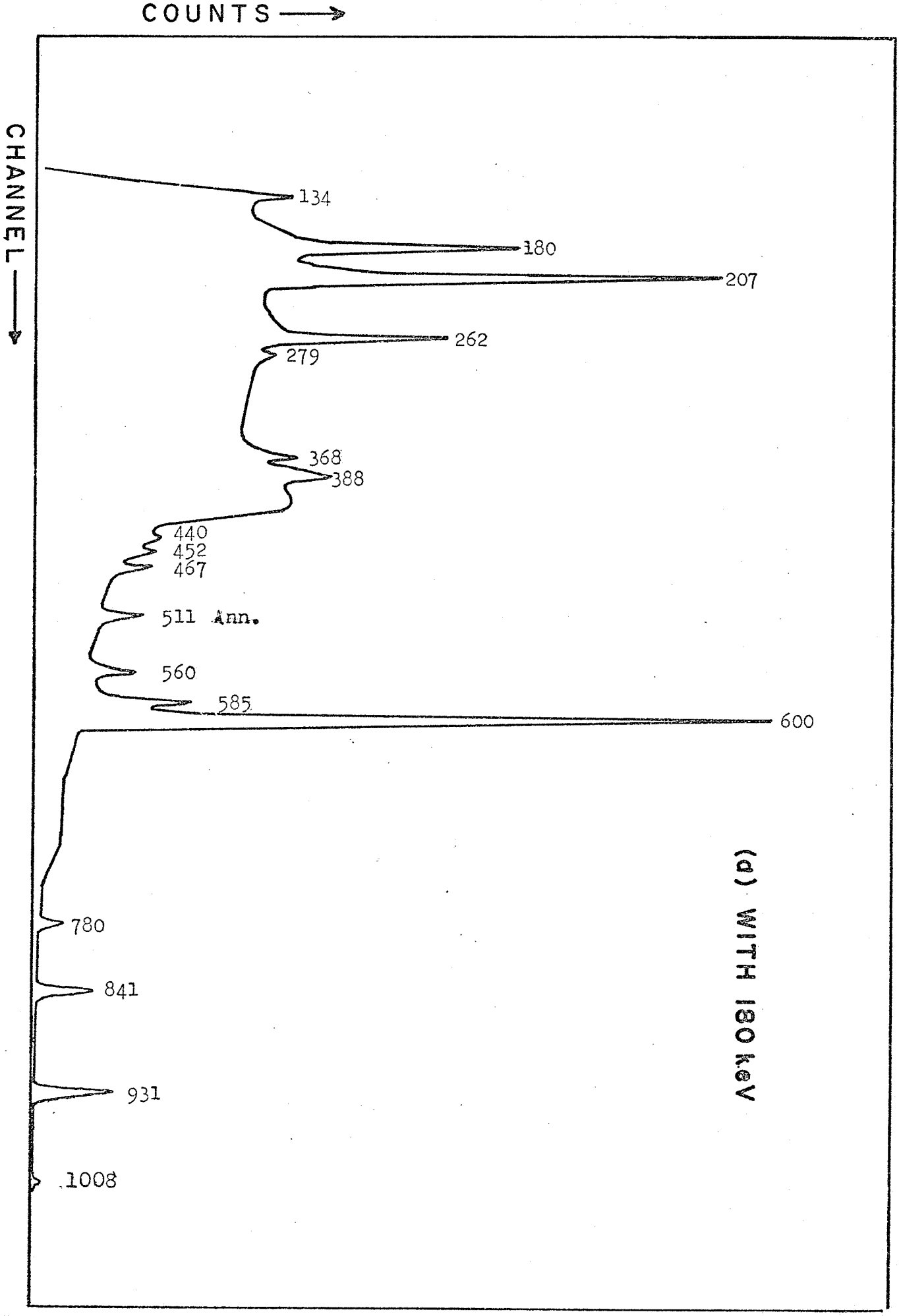
COUNTS
CHANNEL
134
180
207
262
279
368
388
440
452
467
511 Ann.
560
585
600
780
841
931
1008
(d) WITH 180 keV

Figure 3.7

(b) With 207 keV photopeak

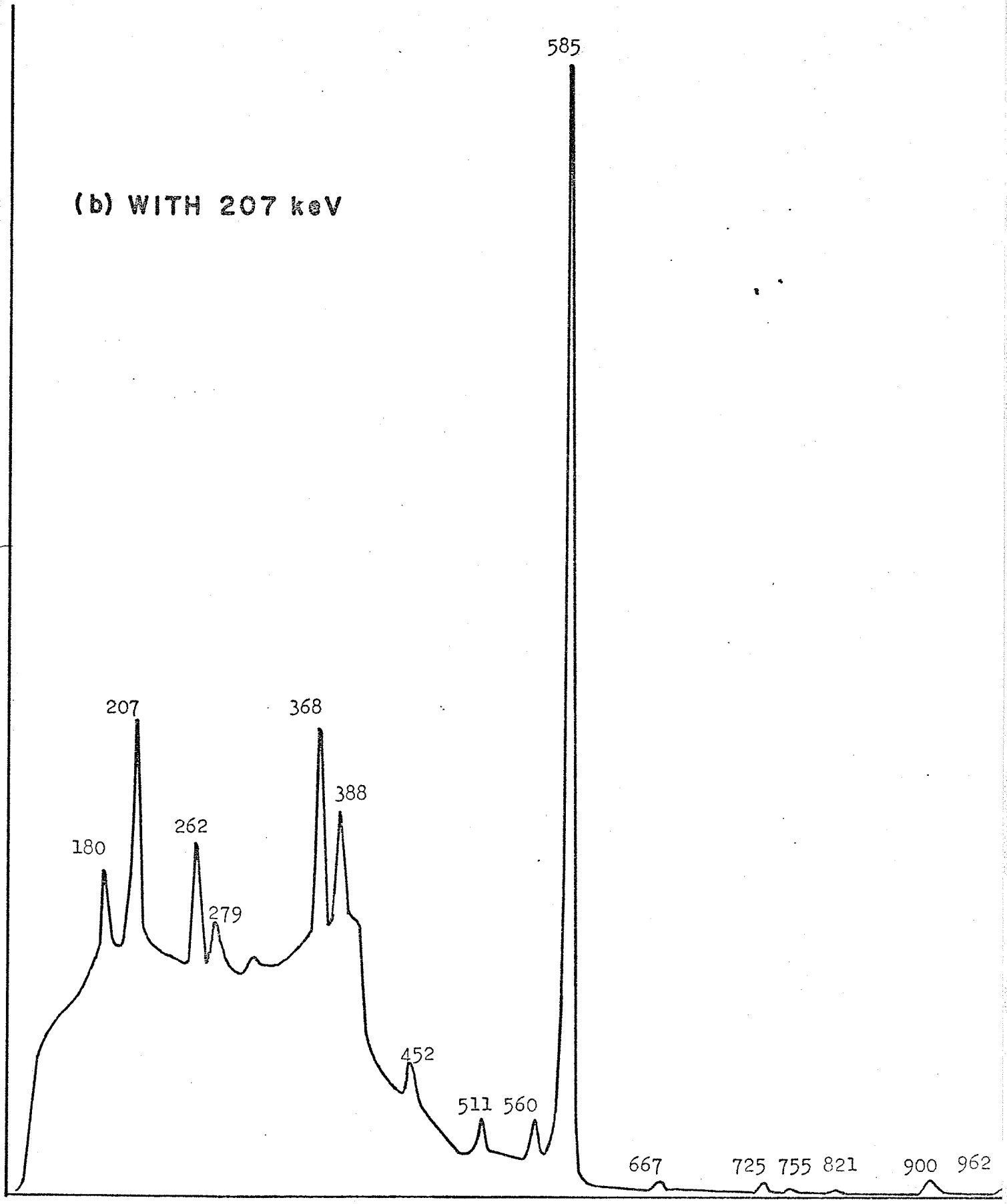
(b) WITH 207 keV
585
207
368
388
262
180
279
452
511
560
667
725
755
821
900
962

Figure 3.7

(c) With compton continuum above 207 keV peak

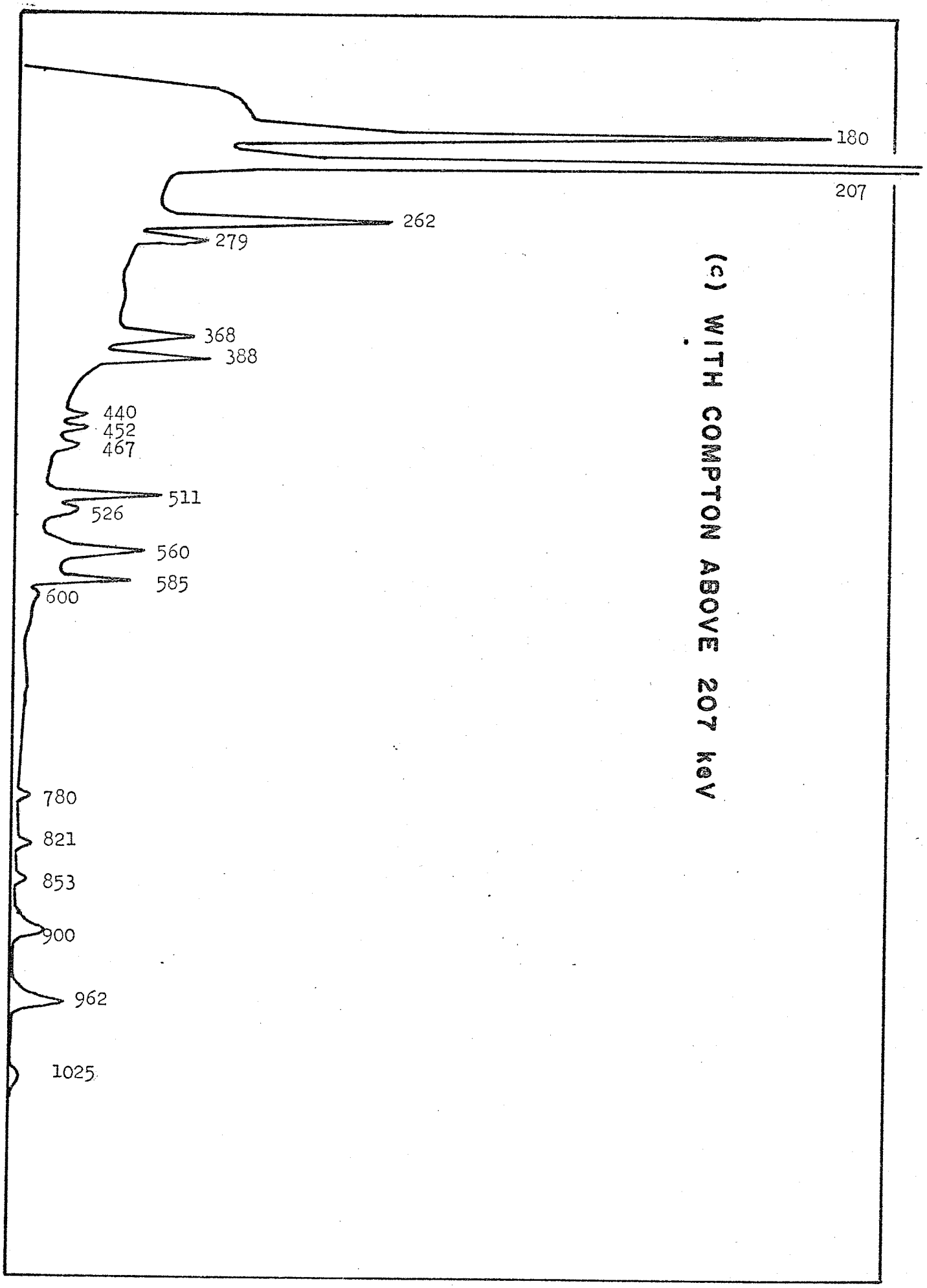
180
207
262
279
368
388
440
452
467
511
526
560
585
600
780
821
853
900
962
1025
(c) WITH COMPTON ABOVE 207 keV

Figure 3.7

(d) With 262 keV photopeak

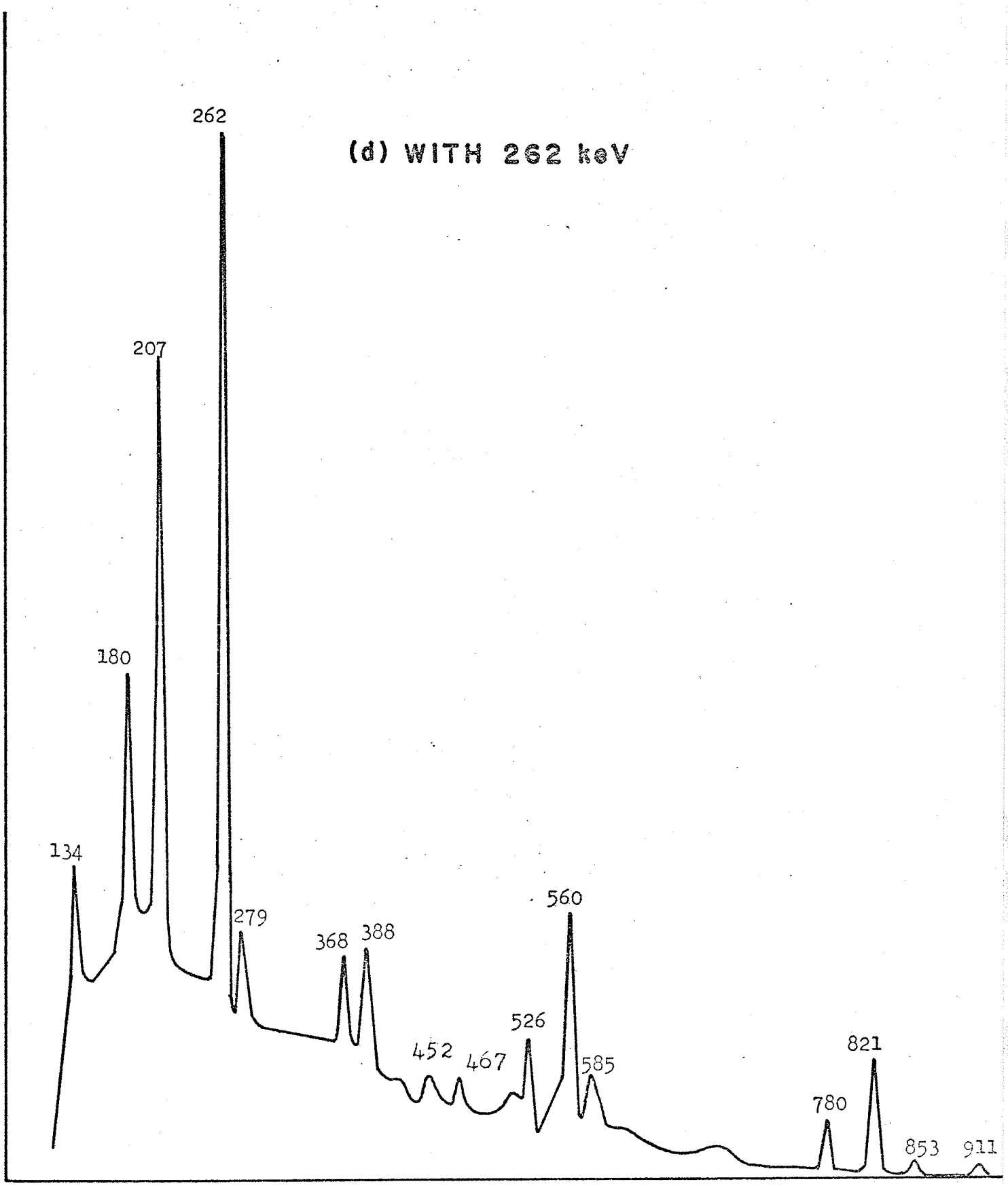
(d) WITH 262 keV
262
207
180
134
279
368
388
560
526
452
467
585
821
780
853
911

Figure 3.7

(e) With 279 keV photopeak

(e) WITH 279 keV

Figure 3.7

(f) With compton continuum above 279 keV peak

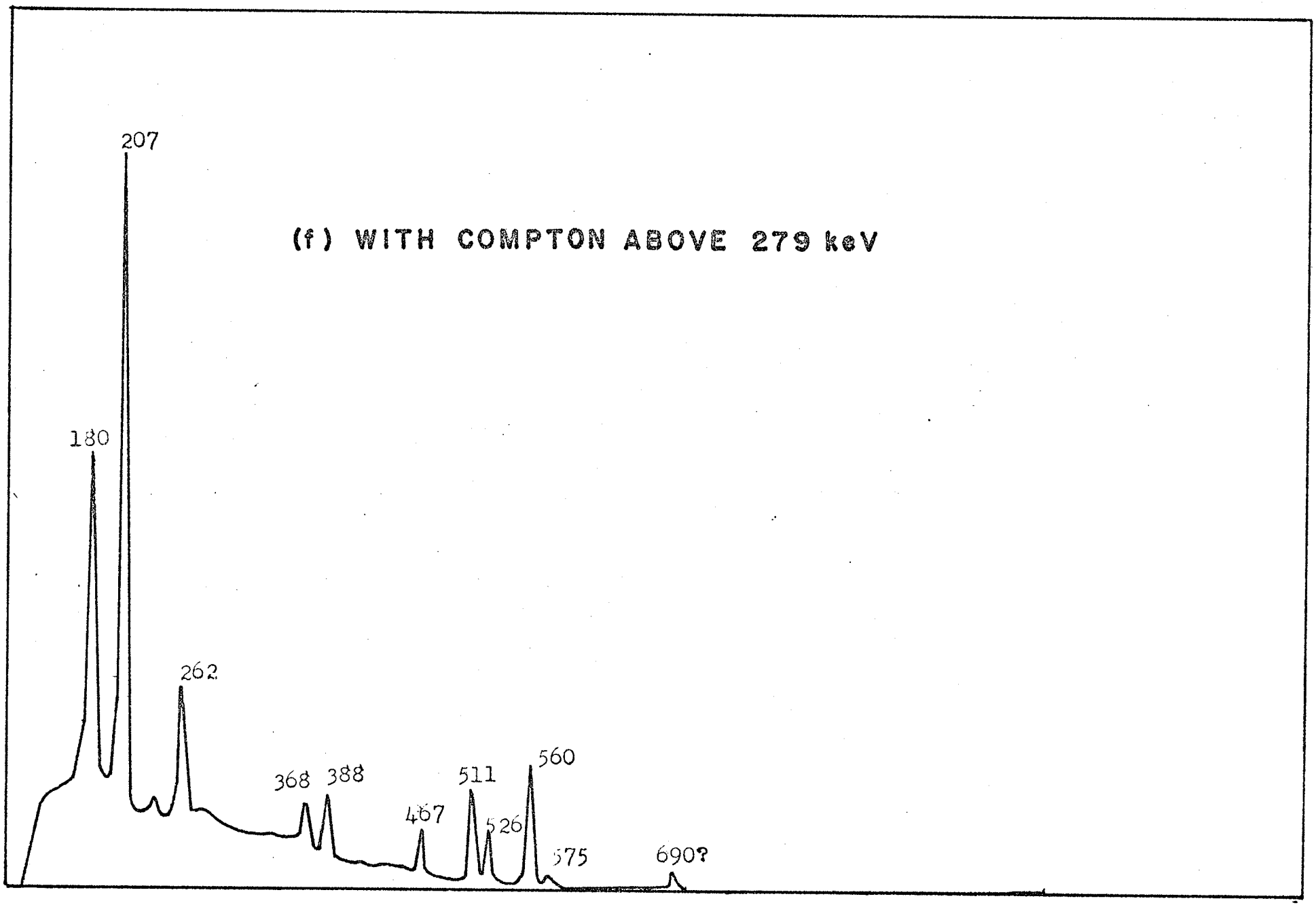
(f) WITH COMPTON ABOVE 279 keV
207
180
262
368
388
467
511
526
560
575
690?

Figure 3.7

(g) With 388 keV photopeak

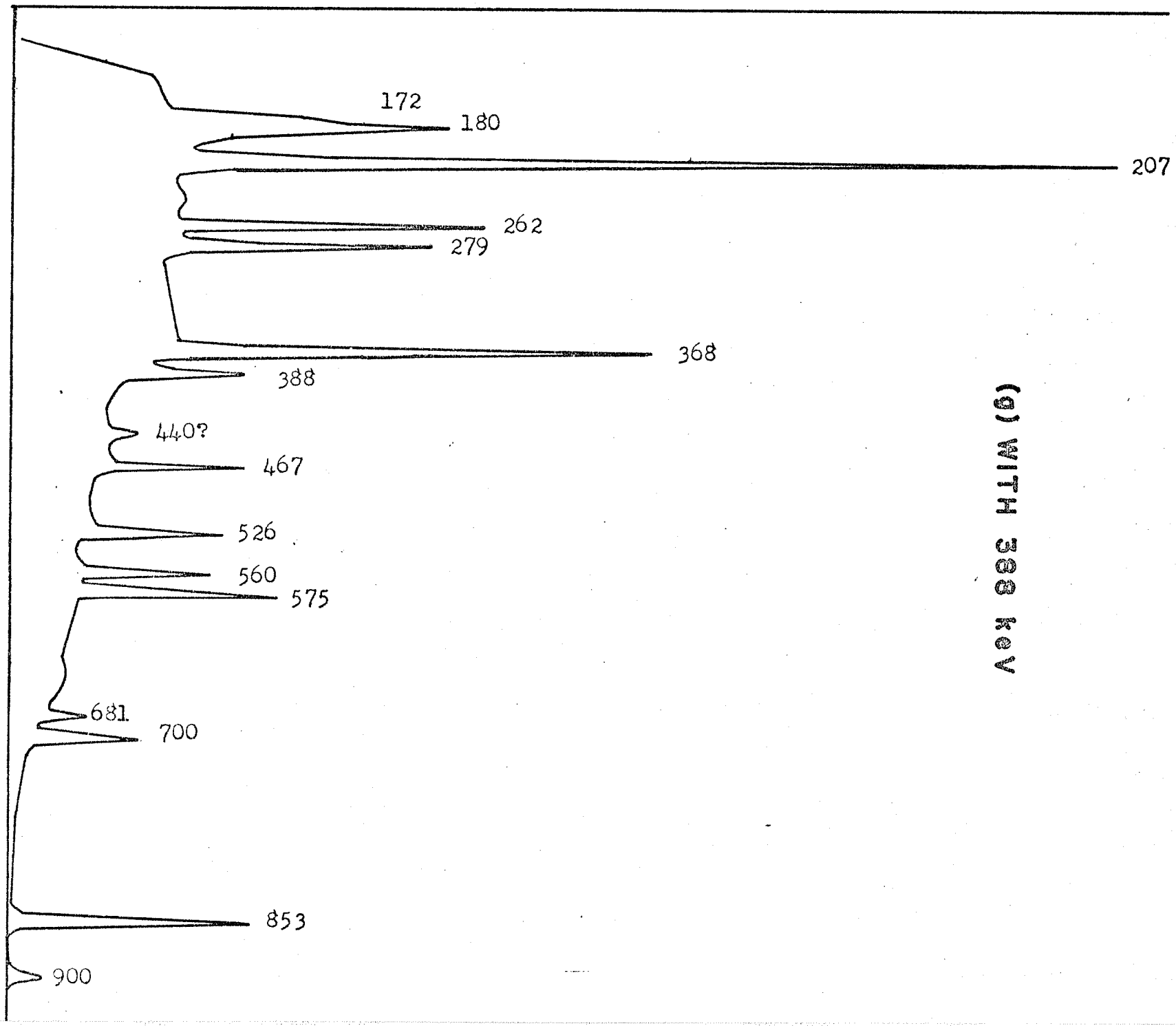
172
180
207
262
279
368
388
440?
467
526
560
575
681
700
853
900
Ag WITH 388 keV (g)

Figure 3.7

(h) With compton continuum above 388 keV peak

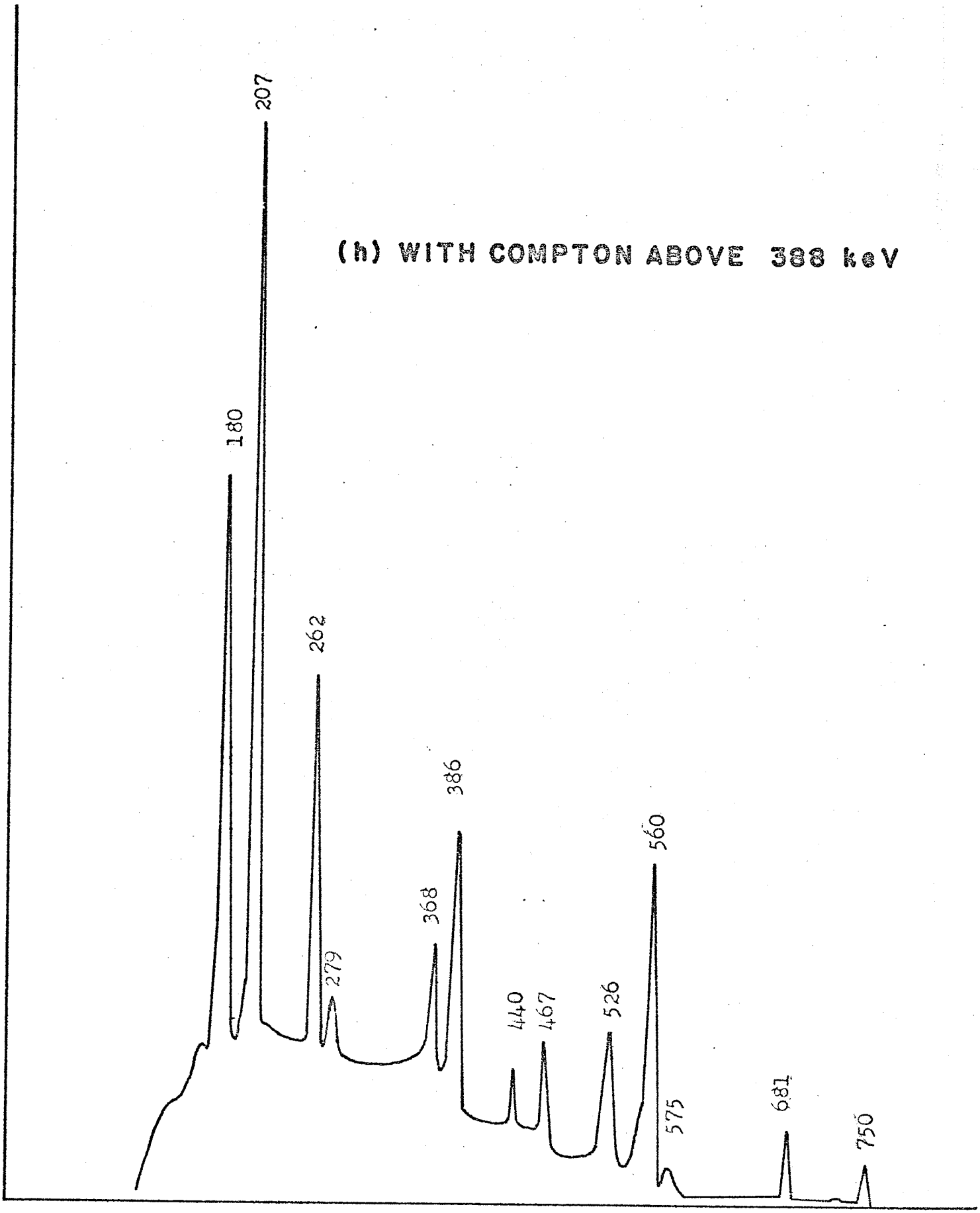
(h) WITH COMPTON ABOVE 388 keV
207
180
262
279
368
386
440
467
526
560
575
681
750

Figure 3.7

(i) With 560 keV photopeak

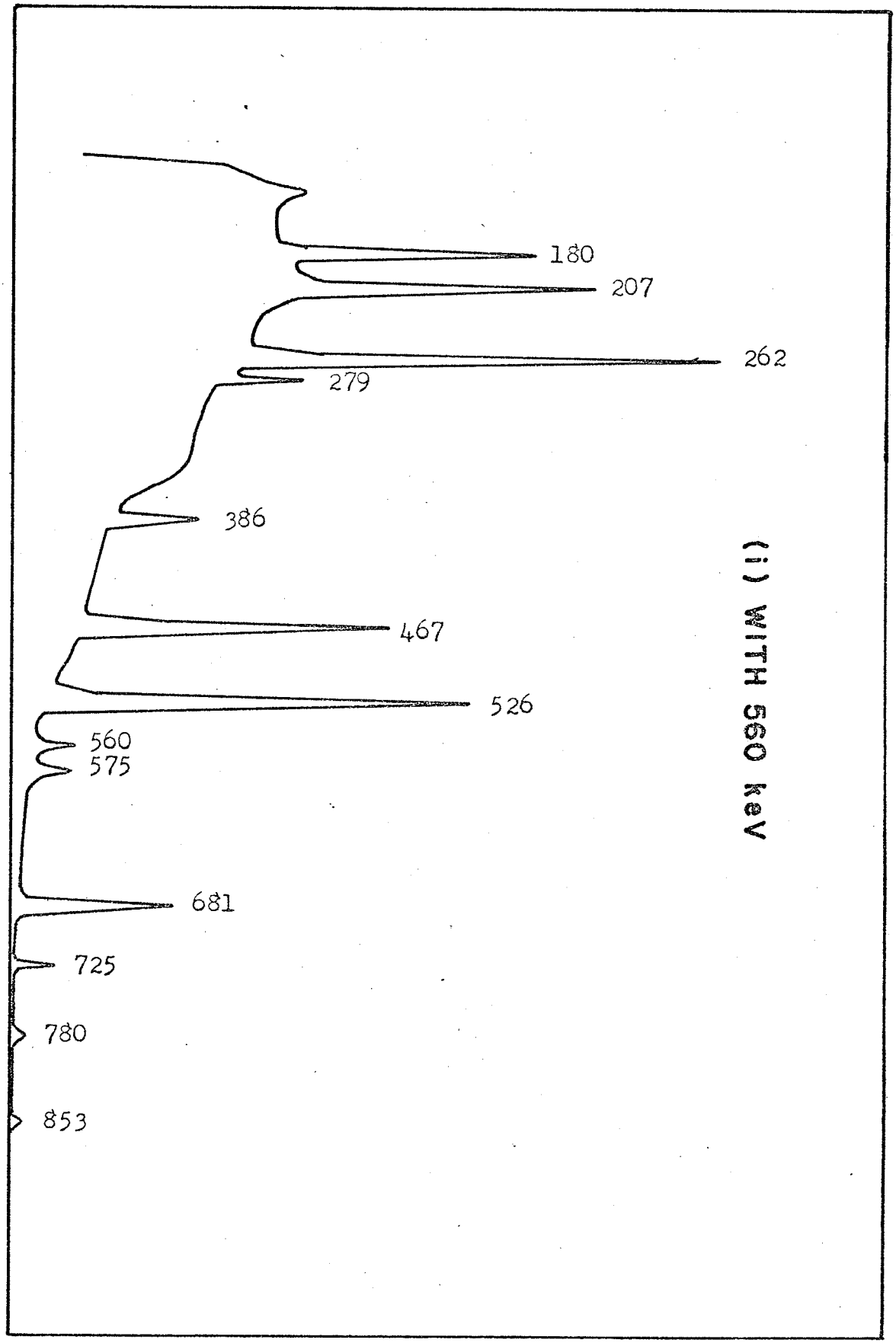
180
207
262
279
386
467
526
560
575
681
725
780
853
(i) WITH 560 keV

normalization of the two spectra. It may at first appear surprising that several lines appear in Fig. 3.7(c) which are absent in Fig. 3.7(a). This can be attributed simply to the fact that a considerably longer counting time was required in the case of the compton coincidence spectrum to obtain adequate statistics, so that very weak lines due purely to compton coincidences are able to make their presence known. The 134 and 780 keV lines in Fig. 3.7(a) are due to random coincidence events. (The absence of the 134 keV line in Fig. 3.7(c) is due to a higher threshold setting on one of the single channel analyzers.) There is no difficulty in identifying the lines at 180, 207, 262, 279, 368, 388, 440, 452, 467, 560, and 585 keV in Fig. 3.7(a) as compton coincidences. The 262 keV line it may be argued is enhanced relative to the 180 keV line but this is probably due to its anomalous decay rate. (See Fig. 3.5) We can conclude then that the 600, 841, 931 and 1008 keV lines are in coincidence with the 180 keV gamma ray. It was interesting to note that the 841 keV line in the coincidence spectrum did not bear the same intensity ratio to the 600 keV line as had been observed in previous singles spectra, but was reduced by approximately a factor of two. This was taken as evidence that this gamma ray is actually a doublet, consisting of the ground state transition from the 842 keV level, and a gamma ray feeding the 242 keV level. The relative intensities of these two components as calculated from the coincidence data, and normalized to a 780 keV line intensity of 100% were as follows:

Populating the ground state 4.6%

Populating the 242 keV state 3.1%

The conclusions of the preceding paragraph and of similar analyses of the other coincidence spectra are summarized in Table 3.4. Here the established coincidences are reported, along with their assigned positions in the Au^{195} level scheme. It will be noted that the 279 keV gamma ray bears a very marked and quite consistent coincidence relationship to many transitions in Au^{195} indicating that, beneath the strong Hg^{197m} impurity line of the same energy, there lies another gamma ray belonging to the Au^{195} level scheme. It has been placed, as the table indicates, between the levels at 1559 and 1280 keV.

One additional coincidence experiment was performed this time using the 35 cc Ge(Li) detector and the o.25 cc Be-window Ge(Li) detector. The latter was used to select the 61 keV photopeak and the gamma ray spectrum in coincidence with this line is shown in Fig. 3.8. This spectrum was of use primarily in verifying the position of the intense 1111 keV gamma ray which could de-excite either the 1173 keV state or the 1111 keV state. The relative intensity of the 1111 keV photopeak in this coincidence spectrum, normalized to $I_{780} = 100$, was found to be $I_{1111} = 16$. As this is in agreement with the relative intensity observed in the singles spectra (Table 3.2) it was concluded that the 1111 keV gamma ray de-excites the 1173 keV state only. An upper intensity limit

TABLE 3.4 γ-γ COINCIDENCE RESULTS

SELECTED PHOTOPEAK	ASSUMED POSITION	COINCIDENT RADIATIONS	ASSIGNMENT
180 keV	242 - 61	600 keV	842 - 242
		841 keV	1083 - 242
		931 keV	1173 - 242
		1008 keV	1250 - 242
207 keV	525 - 318	368 keV	894 - 525
		452 keV	1346 - 894
		585 keV	1111 - 525
		667 keV	1559 - 894
		725 keV	?
		755 keV	1280 - 525
262 keV	262 - 0	262 keV?	525 - 262?
		452 keV	1346 - 894
		585 keV?	1111 - 525
		821 keV	1083 - 262
		853 keV	?
		911 keV	1173 - 262
279 keV	1559 - 1280	368 keV	894 - 525
		386 keV	1280 - 894
		575 keV	894 - 318
		755 keV	1280 - 525
		962 keV	1280 - 318
388 keV } 386 keV }	706 - 318 } 1280 - 894 }	172 keV	879 - 706
		262 keV	262 - 0 ?
		279 keV	1559 - 1280
		368 keV	894 - 525
		467 keV	1346 - 894
		526 keV	1405 - 879
		575 keV	894 - 318
		682 keV	1559 - 879
		700 keV	1405 - 706
		853 keV	1559 - 706
		900 keV	1605 - 706
560 keV	879 - 318	386 keV	?
		467 keV	1346 - 879
		526 keV	1405 - 879
		681 keV	1559 - 879
		725 keV	1605 - 879
		853 keV	?

Figure 3.8

"Gamma rays in coincidence with 61 keV photopeak."

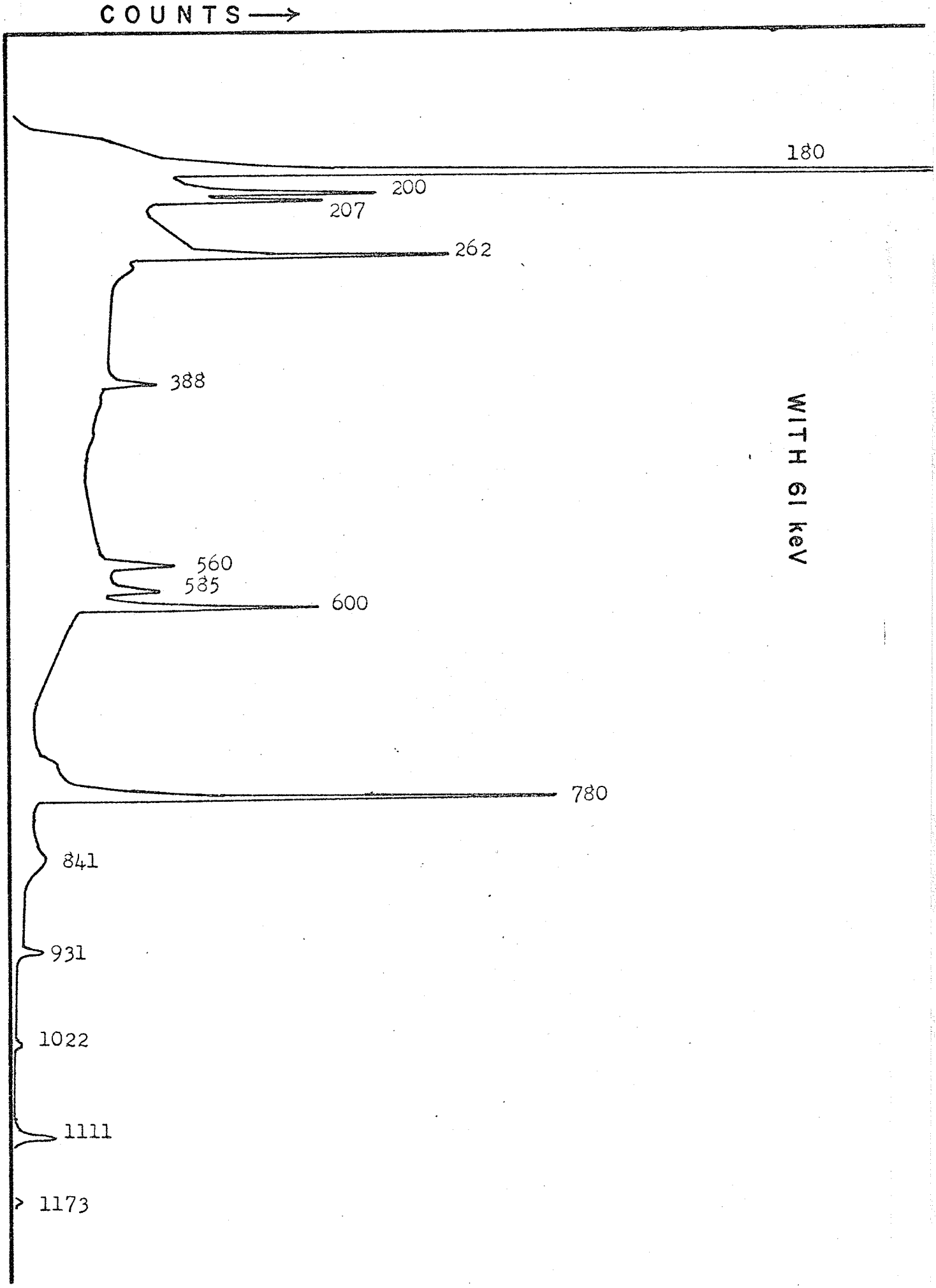
COUNTS ⟶
CHANNEL ⟶
180
200
207
262
388
560
585
600
780
841
931
1022
1111
1173
WITH 61 keV

of ~2 (on the same intensity scale) can be placed on any possible ground state transition from the 1111 keV state.

The level structure indicated by these investigations is presented in Fig. 4.9 in the next chapter. Transitions drawn on the left hand side follow the decay of Hg^{195m} and those drawn on the right follow the decay of the Hg^{195} ground state. The previously accepted decay scheme is confirmed and three additional levels are suggested--at 653 keV, 1250 keV and 1605 keV. The first of these (653 keV) is somewhat doubtful. Although it accounts for four unplaced gamma rays, the only known de-exciting gamma ray (128 keV) has an intensity which decays at the same rate as the Hg^{195} ground state, while the three incoming transitions depopulate levels in equilibrium with Hg^{195m}. This anomaly may be due to as yet undetected feeds from the Hg^{195} ground state. Excluding this level and its associated gammas, a total of 15 new transitions have been placed in Au^{195}. The gamma rays still remaining unaccounted for are the following: 338, 400, 419, 440.4, 519, 543, 550, 666, 791, 847, 870, 137.6 keV. It will be noted in Fig. 4.9 that, in addition to the 262 keV level, the levels at 61 keV, 318 keV, 525 keV and, perhaps, 653 keV are populated indirectly from both Hg^{195} and Hg^{195m}. However, as was indicated earlier in this chapter, the contributions from each parent state interfere significantly only in the case of the 262 keV level. It is only for this state that the effect need be taken

account of in the treatment of population balances. The discussion of population balances and electron capture branching ratios, very important in confirming the decay scheme, will be reserved to the next chapter where the measurements on conversion coefficients are presented.

REFERENCES, CHAPTER III

1. C. M. Lederer, J. M. Holander, and I. Perlman, Table of Isotopes, sixth edition. Wiley (1968).

2. J. Brunner, J. Halter, and P. Scherrer, Helv. Phys. Acta 31, 335 (1958).

3. R. Joly, J. Brunner, and O. Huber, Helv. Phys. Acta 28, 403 (1955).

4. K. H. Frank, Z. Phys. 203, 71 (1967).

5. J. H. E. Mattauch, W. Thiele, and A. H. Wapstra, Nucl. Phys. 67, 1 (1964).

CHAPTER IV

SPIN AND PARITY ASSIGNMENTS IN Au^{195}

INTRODUCTION

We begin, in section (i), with a brief discussion of internal conversion coefficients and their use in gamma ray multipolarity measurements followed by an outline of the formalism of gamma-gamma directional correlations. Section (ii) presents the experimental results of the conversion coefficient and directional correlation data, and section (iii) interprets the level scheme in the light of these results. Finally, in section (iv) the relative photon intensities and measured conversion coefficients are used to calculate population balances for the excited states of Au^{195} and electron capture branching ratios and log ft values are estimated.

(i) Theoretical Considerations

In Chapter II we defined the i-shell internal conversion coefficient as the ratio

$$\alpha_i = \frac{N_e^i}{N_\gamma}$$

of the number of i-shell electrons converted in a given isomeric transition to the number of photons emitted. Physically, one expects orbital electron emission to compete with gamma emission as a means of radiating nuclear energy for the

following reason: If the nuclear transition occurs between nuclear multipoles of order higher than 0, the orbiting electrons experience accelerations due to the sudden changes in these multipoles, and in particular, one of them may acquire sufficient energy to leave the atom[+]. This semiclassical argument can be put on a quantum mechanical footing by defining an initial state consisting of the excited nucleus and atomic electrons, the latter being in their ground state configuration, and a final state consisting of the de-excited nucleus, the atomic electrons with an i-shell vacancy, and an electron travelling away from the nucleus possessing the nuclear transition energy less the i-shell binding energy. These two states are connected by a Hamiltonian H_{INT} which is the energy of interaction between the nucleus and orbital electrons. It turns out that to first order in H_{INT} insofar as the penetration of the nucleus by the electronic wave function can be neglected, the internal conversion electron emission rate is governed by the same reduced transition probability as that for gamma emission. Since it is the reduced matrix elements that possess all the nuclear structure information and since the α_i are defined as ratios of electron to gamma emission rates, the internal

---

[+]If the nucleus de-excites by a monopole transition (i.e. a change in average radius of the nuclear charge distribution) internal conversion can still occur and is in fact the only means of emission possible in $0^+ \rightarrow 0^+$ nuclear transitions. This is because photons must carry away at least one unit of angular momentum. Electrons in an S-shell on the other hand have wave functions which penetrate the finite nuclear radius and so can be influenced by a monopole de-excitation of the nucleus.

conversion coefficients will convey information only about gross features of the transition--i.e. energy and multipolarity. A number of detailed calculations of internal conversion coefficients as a function of energy, multipolarity and nuclear charge which treat the electron relativistically and include important corrections for finite nuclear size have been performed and the results tabulated[1,2,3]. It is through comparison of these theoretical values with the measured α_i's that multipolarities may be assigned.

Turning now to the problem of directional correlations in nuclear gamma radiation, consider the gamma-ray cascade of Fig. 4.1. The nucleus in initial excited state with spin j_1 decays through an intermediate state of spin j to a final state of spin j_2. The electric or magnetic character of the two gamma-rays and their multipole order L (angular momentum of emitted photon) are determined by the spins and parities of the levels involved in the two successive transitions through the selection rules

$$|j_i - j_f| \leq L \leq j_i + j_f$$

$$\pi_i = \pi_\gamma \pi_f$$

which reflect the conservation of angular momentum and parity in the electromagnetic interaction. Here j_i (π_i) is the spin (parity) of the initial state (i.e. j_1 or j) and j_f (π_f) is the spin (parity) of the final state (i.e. j or j_2). π_γ is the

Figure 4.1

"Two nuclear isomeric transitions in cascade."

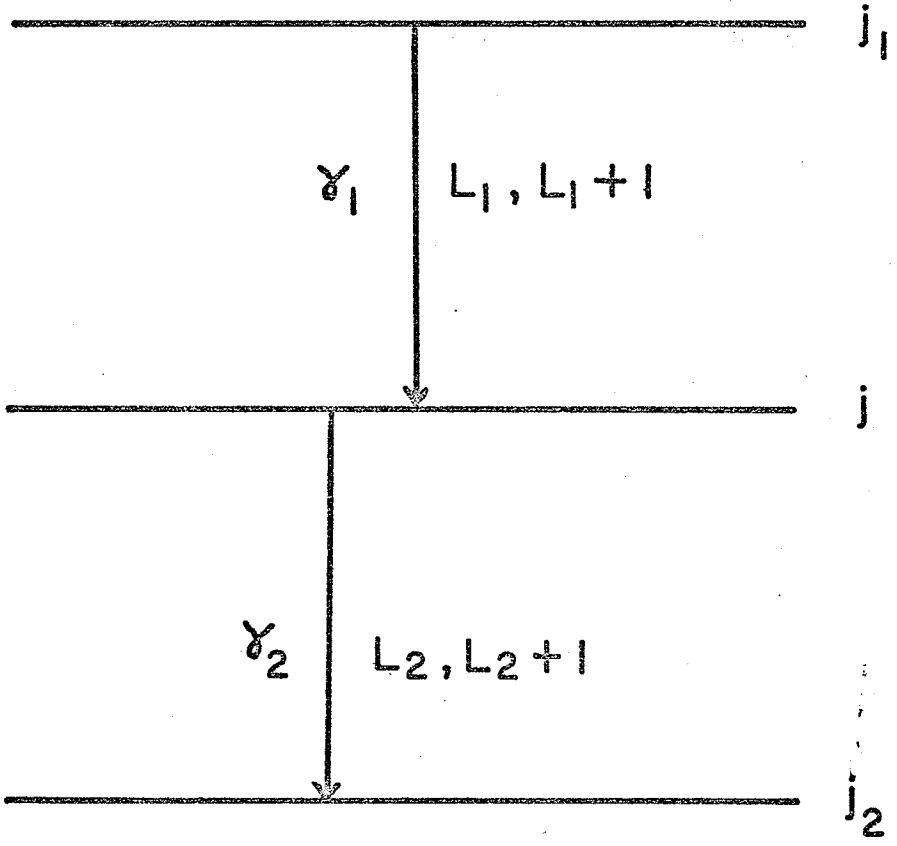
j_1
γ_1
L_1, L_1+1
j
γ_2
L_2, L_2+1
j_2

parity of the emitted photon. The expansion of the interaction in terms of multipole fields (electromagnetic fields of definite spin and parity) is such that at most only the lowest two allowed multipole orders contribute significantly to the radiation. The possibility of such admixtures is allowed for in Fig. 4.1.

At elevated temperatures (eg. room temperature) the nuclei in a given sample populate equally the degenerate $(2j_1 + 1)$ magnetic substates of the initial level. (In classical language the nuclei are randomly oriented). Hence the first radiation (γ_1) is isotropic relative to the fixed axis of quantization. In a conventional directional correlation experiment the first radiation is observed only in a fixed direction defined by the unit vector $\underline{k}_1$ relative to this axis. The population of the magnetic substates of the intermediate level by nuclei for which γ_1 has been observed is no longer random. Indeed the density matrix which describes the intermediate state j is a function of $\underline{k}_1$. If the intermediate state is of sufficiently short lifetime so that extranuclear fields do not alter this population balance before emission of the second gamma ray (γ_2), then the probability of emission of γ_2 in the direction $\underline{k}_2$ will be functionally related to the direction of observation $\underline{k}_1$ of γ_1. Specifically, if $\cos\theta = \underline{k}_1 \cdot \underline{k}_2$ it can be shown that

$$W(\theta) = \sum_{k \text{ even}} A_k(1) \cdot A_k(2) \cdot P_k(\cos\theta) \qquad (1)$$

$W(\theta)$ is the probability per unit solid angle for observation of γ_2 having previously observed γ_1, and the P_k's are Legendre polynomials. The $A_k^{(\nu)}$' are of the form

$$A_k^{(\nu)'} = F_k\,(L_\nu,\ L_\nu,\ j_\nu,\ j) + 2\delta_\nu\, F_k\,(L_\nu,\ L_\nu + 1,\ j_\nu,\ j) + \delta_\nu^2\, F_k\,(L_\nu + 1,\ L_\nu + 1,\ j_\nu,\ j) \qquad \nu = 1,\ 2$$

The summation over k runs from zero to the least of $2j$, $2(L_1 + 1)$, $2(L_2 + 1)$. The F_k are geometrical factors expressible in terms of the 3j and 6j symbols and are defined and tabulated by Ferentz and Rosenzweig[4].

The "mixing ratio" δ^2 is the ratio of the intensity of the $L_\nu + 1$ radiation to the L_ν radiation in the ν'th transition of the cascade. More specifically, if we consider the transition

$$j_1\ m_1 \xrightarrow{L_1 M_1 \pi_1} j\ m$$

induced by some scalar interaction Hamiltonian H, the transition matrix element is

$$\langle j\ m\ L_1\ M_1\ \pi_1 \mid H \mid j_1\ m_1 \rangle$$

where $|j\ m\ L_1\ M_1\ \pi_1\rangle = |j\ m\rangle\ |L_1\ M_1\ \pi_1\rangle$ is the final state of the unperturbed Hamiltonian of the nucleus and the electromagnetic field and $|j_1\ m_1\rangle = |j_1\ m_1\rangle\ |0\rangle$ is the initial state. Thinking of $|L_1\ M_1\ \pi_1\rangle$ as the M_1'th component of an irreducible tensor of rank L_1 we can apply the Wigner-Eckart theorem to factor out a reduced (geometry independent) matrix element from the transition matrix element--viz.

$$\langle j\ m\ L_1\ M_1\ \pi_1 \mid H \mid j_1\ m_1 \rangle = \langle j\ m\ L_1\ M_1 \mid j_1\ m_1 \rangle \langle j \| L_1\ \pi_1 \| j_1 \rangle$$

A similar expression holds for the $L_1 + 1$ radiation, and δ_1 is defined as the ratio of the two reduced matrix elements.

$$\delta_1 = - \frac{\langle j \| L_1 + 1, \pi_1 \| j_1 \rangle}{\langle j \| L_1, \pi_1 \| j_1 \rangle}$$

The ratio of the intensity of the $L_1 + 1$ radiation to that of the L_1 radiation is then δ_1^2. i.e. the required ratio is the ratio of the squares of the transition matrix elements summed over final and averaged over initial magnetic substates.

$$\frac{(2j_1 + 1)^{-1} \sum_{m m_1} | \langle j\, m\, L_1 + 1\, M_1\, \pi_1 | H | j_1\, m_1 \rangle |^2}{(2j_1 + 1)^{-1} \sum_{m m_1} | \langle j\, m\, L_1\, M_1\, \pi_1 | H | j_1\, m_1 \rangle |^2}$$

$$= \frac{| \langle j \| L_1 + 1\, \pi_1 \| j_1 \rangle |^2}{| \langle j \| L_1\, \pi_1 \| j_1 \rangle |^2} = \delta_1^2$$

where we have used the orthogonality properties of the Clelsch-Gordan coefficients and the fact that $M_1 = m - m_1$. Similar equations of course hold for the second transition γ_2.

In the present investigations the maximum value of k was 4. The normalized theoretical coefficients A_2 and A_4 in the expression

$$W(\theta)_{Th} = 1 + A_2 P_2 (\cos\theta) + A_4 P_4 (\cos\theta) \qquad (2)$$

were determined by fitting a similar expression to the data collected at three angles and correcting the coefficients so obtained for finite solid angle. The method of extracting these coefficients from the experimental data as well as the finite detector solid angle correction is discussed in Appendix II. The A_k of equation (2) are related to the $A_k(\nu)$' of

equation (1) by

$$A_k = \left(\frac{A_k(1)'}{A_o(1)'}\right)\left(\frac{A_k(2)'}{A_o(2)'}\right)$$

and if we make use of the relations

$$F_o\ (L,\ L,\ j',\ j) = 1$$

$$F_o\ (L,\ L+1,\ j',\ j) = 0 \text{ we obtain}$$

$$A_k = A_k(1)\ A_k(2) = \left(\frac{A_k(1)'}{1 + \delta_1^2}\right)\left(\frac{A_k(2)'}{1 + \delta_2^2}\right)$$

Arns and Weidenbeck[5] have presented graphs of the quantities $A_k(\nu)$ as a function of the mixing ratio δ^2 (or rather as a function of $Q = \frac{\delta^2}{1+\delta_2^2}$) which facilitate the determination of the mixing ratio of one transition when that of the other is known. Use has been made of these graphs in the analysis to follow.

(ii) Experimental Results

K and L-shell internal conversion coefficients were measured with the solid state conversion coefficient spectrometer discussed in Chapter II. Sublimed $Hg^{195,195m}$ sources were prepared and covered with VYNS film to prevent evaporation in the manner described in Chapter III. The observed electron spectrum is shown in Fig. 4.2. In this particular run, data was accumulated for a period of 44 hours, starting 12 hours after irradiation with 25 MeV protons. As

Figure 4.2

"Conversion electron spectrum of $Hg^{195,195m}$ in the energy region above 100 keV as seen with the KEVEX 3 mm Si(Li) detector. Energies are in keV. The proton bombarding energy was 25 MeV."

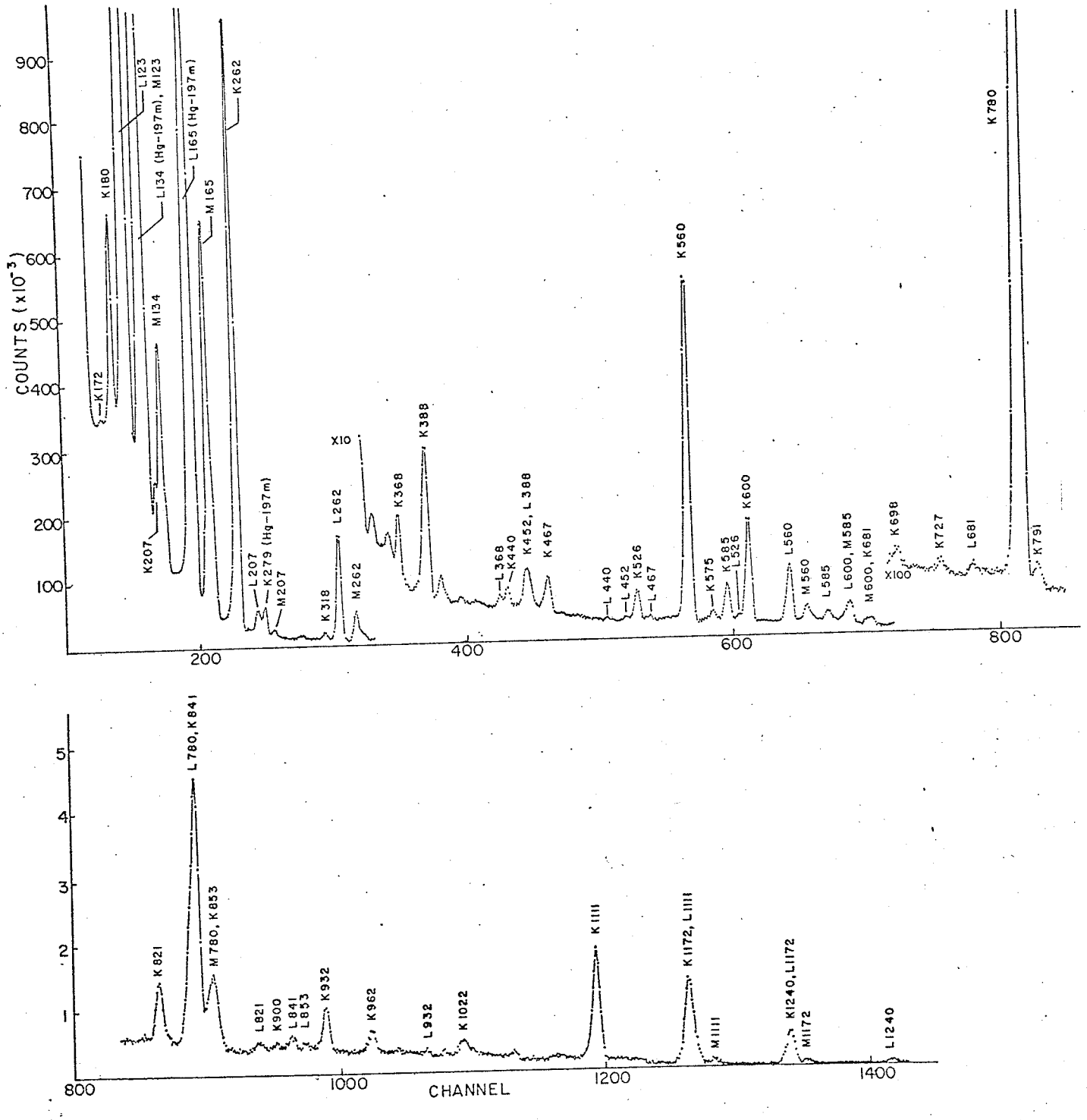
COUNTS (x10⁻³)
CHANNEL
K172
K180
L123
L123 (Hg-197m), M123
L134 (Hg-197m)
M134
L165 (Hg-197m)
M165
K262
K207
L207
K279 (Hg-197m)
M207
K318
L262
M262
X10
K368
K388
L368
K440
K452, L388
K467
L440
L452
K526
L467
K560
K575
K585
L525
K600
L560
M560
L585
L600, M585
M600, K681
X10
K698
K727
L681
K780
K791
K821
L780, K841
M780, K853
L821
K900
L841
L853
K932
K962
L932
K1022
K1111
K1172, L1111
M1111
K1240, L1172
M1172
L1240

can be seen the electron spectrum is quite complicated. In many cases interference between electron groups prevented calculation of conversion coefficients of interest. In all, five runs were taken, spaced over a period of several months, and the measured α_K and α_L values are presented in Table 4.1. Some of the numbers in Table 4.1 require special mention. In the case of the 318, 575, 698, 727, 898 and 1022 keV transitions, K-conversion coefficients were calculated using relative gamma intensities from the 35 cc Ge(Li) detector after normalization to the intensity of the 560 keV line as observed in the conversion coefficient spectrometer. The low intensity or unresolved nature of these lines did not permit direct observation in the spectrometer. Thus for these six transitions an additional efficiency calibration curve had to be used, that of the 35 cc detector, so the measured α_K values are somewhat less reliable than the others. Also it may be noted from Fig. 4.2 that the K841 electron line is completely masked by the L780 line. However if the result of Brunner et al.[6] that the K841 and K821 lines are of equal intensity is accepted, an estimate of α_K (841 keV) and α_L (780 keV) is possible. The numbers in Table 4.1 for these two quantities were obtained with this assumption. Evidence was presented in Chapter III that the 841 keV line is in fact a doublet comprised of the ground state de-excitation of the 841 keV level and a de-excitation of the 1083 keV level (Fig. 3.1).

TABLE 4.1 INTERNAL CONVERSION COEFFICIENTS

E_γ (keV)	RUN	α_K	α_L	K/L
180	3	0.90		
	4	0.98		
	5	0.99	0.16	6.2
207	4		0.10	
	5		0.10	
262	1	0.288	0.056	5.1
	2	0.278	0.051	5.4
	3	0.275	0.049	5.6
	4	0.291	0.050	5.8
	5	0.299	0.056	5.9
318	4	6.5[a]		
368	4	0.11	0.021	5.5
388[b]	1	0.084		
	2	0.082		
	3	0.082		
	4	0.083		
452	4		0.024	
467	4		0.013	
526	2	0.062		
	4	0.064		
560	1	0.051	0.0082	6.2
	2	0.049	0.0081	6.0
	3	0.045	0.0070	6.5

TABLE 4.1 (CONTINUED)

E_γ (keV)	RUN	α_K	α_L	K/L
	4	0.050	0.0082	6.2
575	4	0.04[a]		
585	1	0.011		
	2	0.012	0.0028	4.3
	4	0.011	0.0028	3.9
600	1	0.047		
	2	0.039	0.0082	4.9
	4	0.042	0.0097	4.4
681	4		0.0052	
698	4	0.092[a]		
727	4	0.065[a]		
780	1	0.020		
	2	0.020		
	4	0.021	0.0038[c]	
821	2	0.022		
	4	0.021	0.0038	5.5
841	2	0.011[b]		
	4	0.009[b]	0.0019[b]	5.3
898	4	0.036[a]		
932	2	0.0076		
	4	0.0082		
962	4	0.015		
1022	4	0.0077[a]		

TABLE 4.1 (CONTINUED)

E_γ (keV)	RUN	α_K	α_L	K/L
1111	2	0.0094		
	4	0.0090		
1173	2	0.0069		
	4	0.0073		
1240	4		0.0013	

(a) Gamma intensities from 35 cc Ge(Li) detector

(b) Unresolved doublet

(c) Assuming K821 and K841 are of equal intensity

Hence the measured α_K and α_L cannot be taken as definite evidence of an M1, E2 character for either radiation. Other de-excitations however restrict the spin of the 841 keV level to $(1/2^+, 3/2^+)$ and of the 1083 keV level to $3/2^+$. Hence both 841 keV radiations must be M1 or M1, E2, a requirement which is of course consistent with the observed α_K and α_L.

The low energy region of the electron spectrum (Fig. 4.2) is seen to be rather complicated by the Hg^{197m} impurity. Fig. 4.3 shows the low energy region of the electron spectrum taken from a target irradiated at 40 MeV. While considerably reduced in intensity, Hg^{197m} conversion lines are still present. This spectrum was of use in obtaining α_K (180 keV), α_L (180 keV) and α_L (207 keV) (run 5 in Table 4.1).

The error assignments were somewhat arbitrary. The agreement of the Bi^{206}, Bi^{207} measurements with previous values (see Chapter II) using this arrangement indicated a probable error of $\pm$ 10% in α_K and α_L. This indeed is the uncertainty reported by Haverfield et al. (ref. [1] Chapter II) in their work with a similar system. When electron and/or gamma lines were incompletely resolved so that background subtraction was uncertain, or when full energy lines were poorly defined statistically, this error was increased to $\pm$ 20% (or to $\pm$ 50% in the case of α_L (452 keV) where both these effects contribute).

The means of the various runs along with their assumed

Figure 4.3

"Conversion electron spectrum of $Hg^{195,195m}$ in the energy region 30-200 keV as seen with the KEVEX 3 mm Si(Li) detector. Energies are in keV. The proton bombarding energy was 40 MeV."

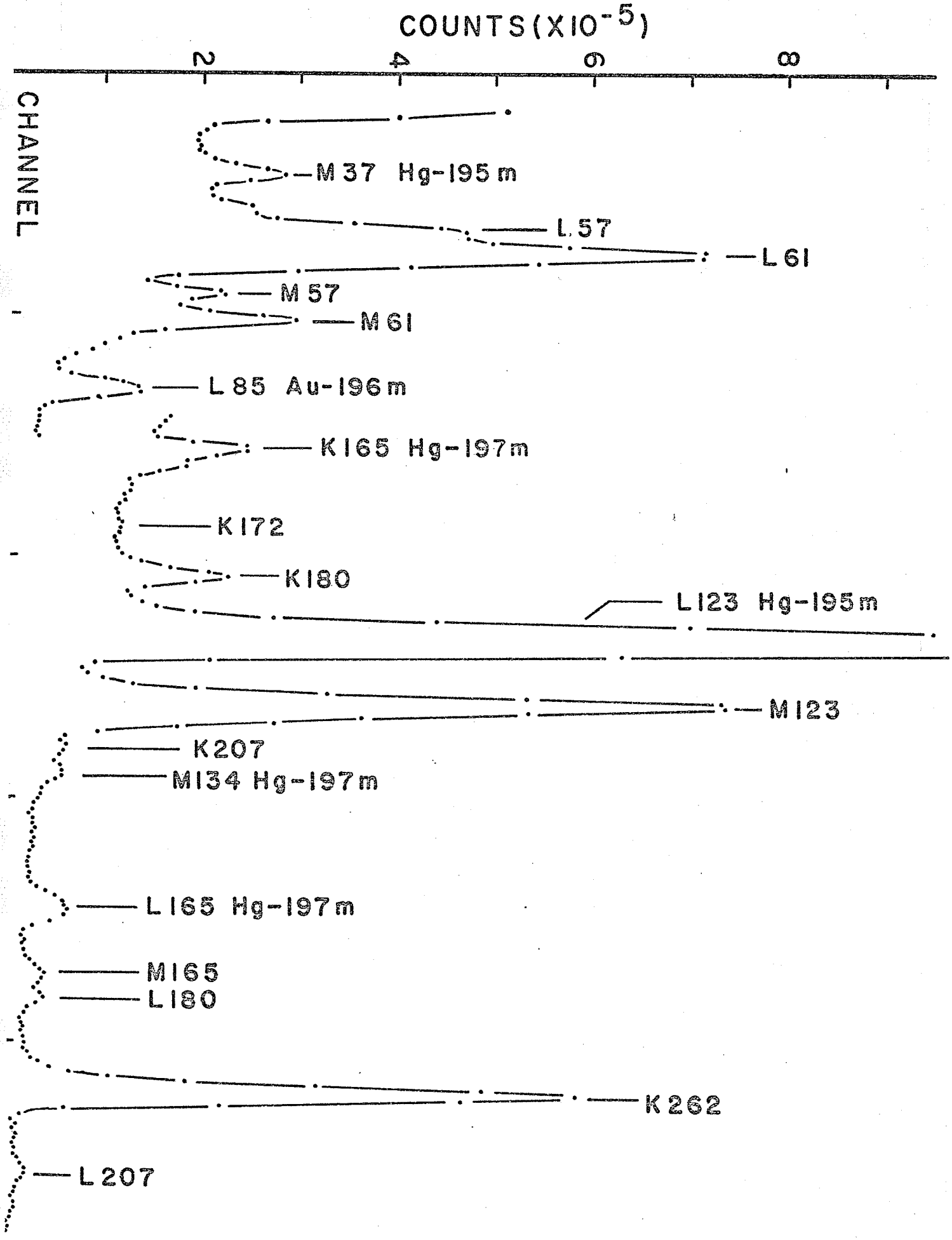
COUNTS (X10⁻⁵)
2
4
6
8
CHANNEL
M 37 Hg-195 m
L 57
L 61
M 57
M 61
L 85 Au-196 m
K 165 Hg-197m
K 172
K 180
L 123 Hg-195m
M 123
K 207
M 134 Hg-197m
L 165 Hg-197m
M 165
L 180
K 262
L 207

errors and the assigned multipolarities are summarized in Table 4.2. Comparison is also made in this table with the results of Frank[7], who used his gamma ray intensity data and the conversion electron data of Brunner et al.[6] and Joly et al.[8] to calculate internal conversion coefficients for a large number of transitions in Au^{195}. The agreement between the present work and that of Frank is poor.

In Figures 4.4 and 4.5 are presented graphically the α_K and α_L measurements. The theoretical values (solid lines) plotted on these graphs were obtained from the tabulated values of Hager and Seltzer[3].

The multipolarity assignments in column 5 of Table 4.2 are interpreted as follows: The assignment "M1 (E2)" indicates that the experimental point falls, within quoted error, on the theoretical curve for pure M1 transitions. Because of the rather large error, the possibility of E2 admixtures can of course never be ruled out. The assignment "M1, E2" (i.e. without parentheses) indicates a probable E2 admixture. Whenever the α_K and/or α_L measurements did not rule out the possibility of E3 (or M2, E3) transitions this is indicated by appending "E3?". The E2 assignment for the 207 keV transition is based on the measurement of Jung et al.[9]. The present measurement of α_L is consistent with their interpretation.

Before turning to the angular correlation results we can make use of some of the above conversion coefficients to

TABLE 4.2 MULTIPOLARITY ASSIGNMENTS

E_γ (keV)	PRESENT WORK α_K	PRESENT WORK α_L	FRANK α_K	FRANK α_L	ASSIGNMENT
9.5 hr					
180	0.96 ± 0.1	0.16 ± 0.03	0.85	0.19	M1, E2
207		0.10 ± 0.02			E2[9]
585	0.011 ± 0.001	0.0028 ± 0.0003	0.0047	0.0012	E1, M2
600	0.043 ± 0.004	0.0089 ± 0.002	0.018	0.003	M1(E2)
780	0.020 ± 0.002	0.0038 ± 0.0008	0.0096	0.0022	M1(E2)
821	0.021 ± 0.002	0.0038 ± 0.0004	0.009		M1(E2)
841(a)	0.010 ± 0.002	0.0019 ± 0.0002	0.004		M1, E2
932	0.0079 ± 0.0008		0.014		M1, E2
1022	0.0077 ± 0.0016		0.009		M1, E2
1111	0.0092 ± 0.001		0.005	0.001	M1(E2)
1172	0.0071 ± 0.0014		0.0047		M1(E2) E3?
40 hr					
173			>0.15		
262	0.29 ± 0.03	0.052 ± 0.0005	0.35	0.058	M1, E2
318	6.5 ± 1				M4
368	0.11 ± 0.01	0.021 ± 0.004	0.042	0.01	M1, E2
388(a)			0.024		
452		0.024 ± 0.01	0.024	0.0048	M1?
467		0.013 ± 0.02	0.023		M1(E2)
526	0.063 ± 0.006		0.04	0.007	M1(E2)
560	0.049 ± 0.005	0.0079 ± 0.0008			M1(E2)
575	0.04 ± 0.01		0.008		M1(E2) E3?
681		0.0052 ± 0.0005	0.015		M1(E2)

TABLE 4.2 (CONTINUED)

E_γ (keV)	PRESENT WORK α_K	PRESENT WORK α_L	FRANK α_K	FRANK α_L	ASSIGNMENT
698	0.092 ± 0.02				M2?
727	0.065 ± 0.012				M2?
898	0.036 ± 0.008				M2?
962	0.015 ± 0.002		0.0067		M1(E2)
1240		0.0013 ± 0.0002	0.0034		M1(E2)

(a) Unresolved doublet

(b) Jung and Svedberg, Ref. 9

Figure 4.4

"The experimental α_K values (points) as compared with the theory of Hager and Seltzer[3] (solid lines)."

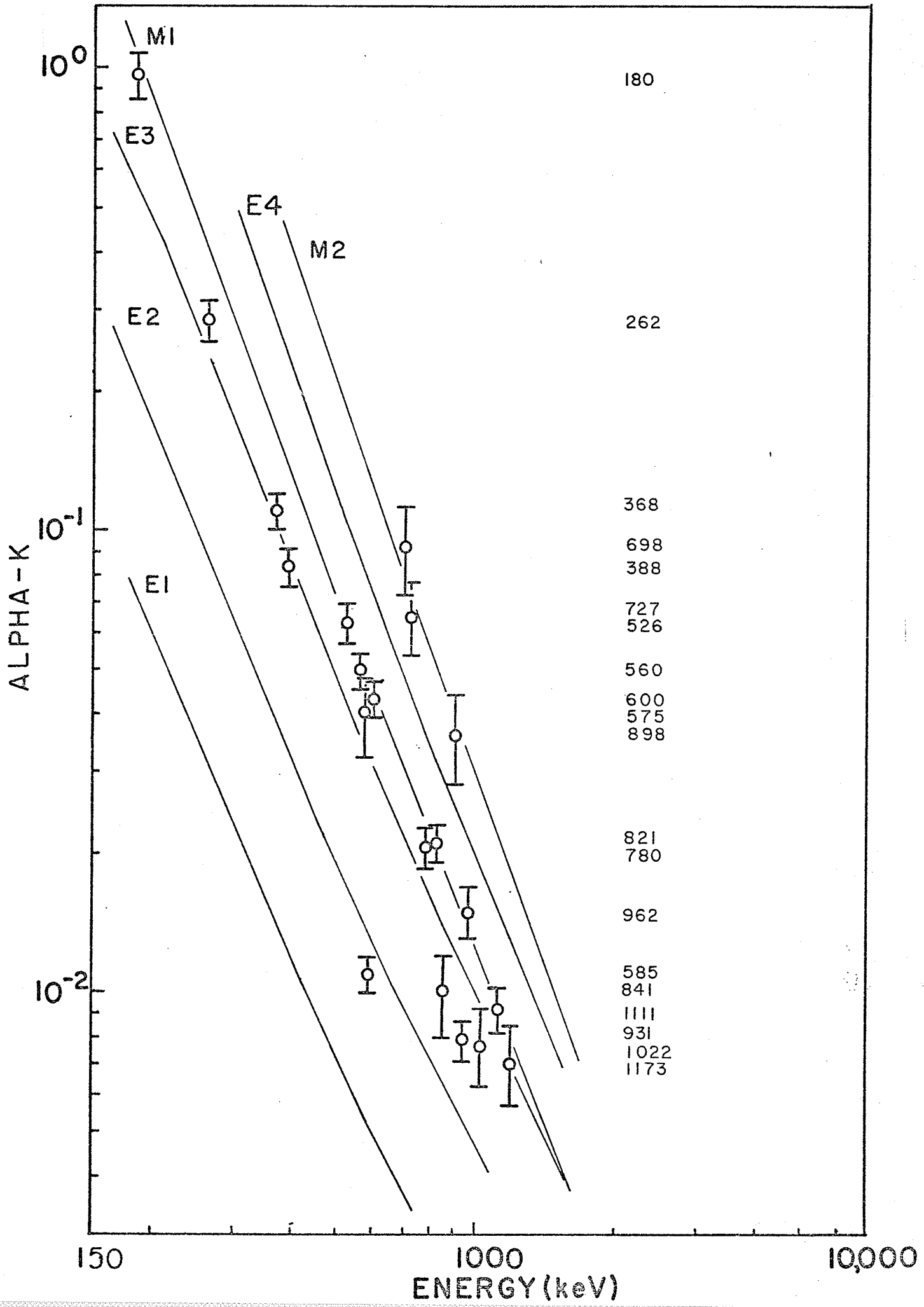
M1
E3
E4
M2
E2
E1
180
262
368
698
388
727
526
560
600
575
898
821
780
962
585
841
1111
931
1022
1173
10^0
10^{-1}
10^{-2}
ALPHA-K
150
1000
10,000
ENERGY (keV)

Figure 4.5

"The experimental α_L values (points) as compared with the theory of Hager and Seltzer[3] (solid lines)."

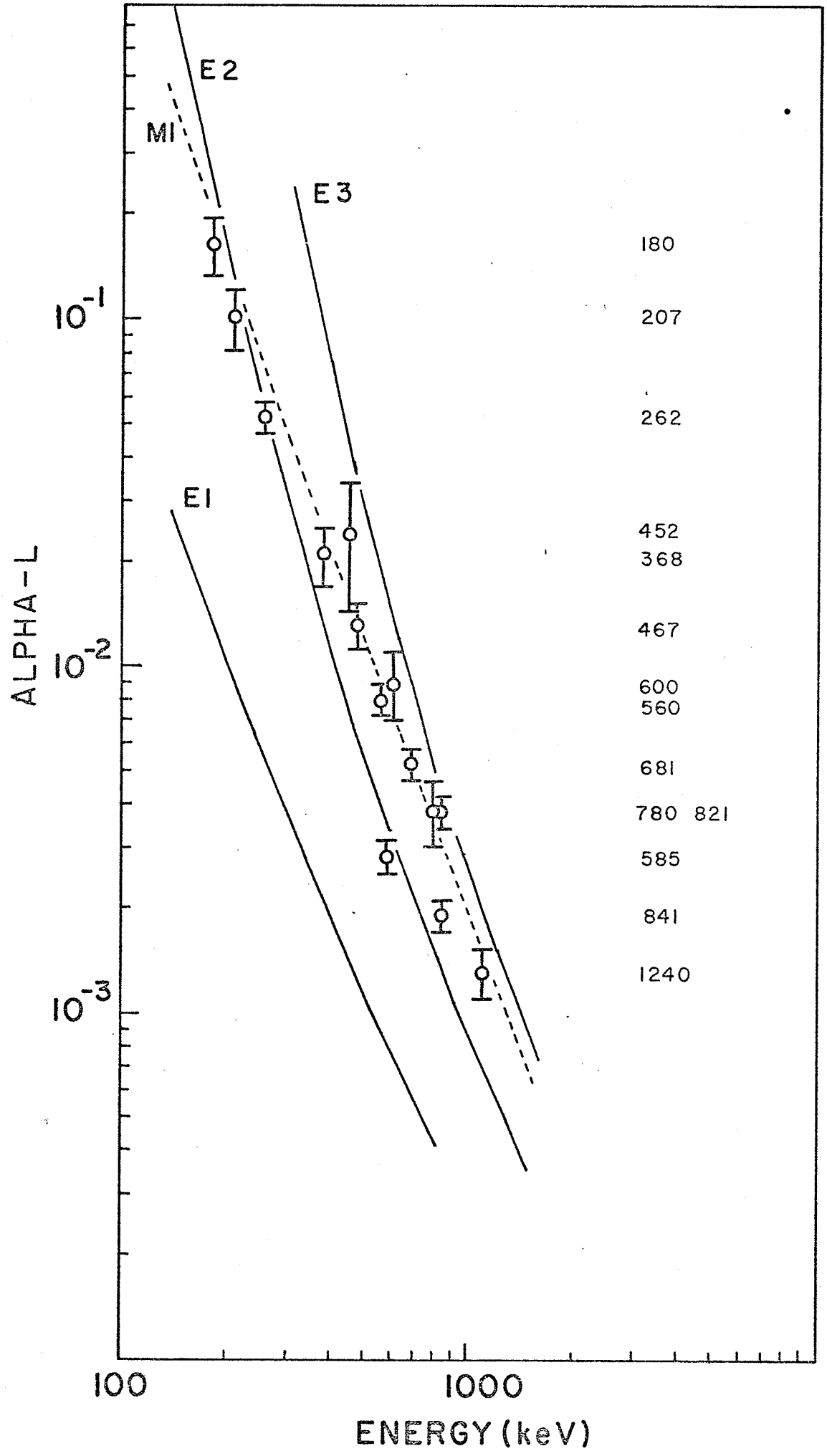
E2
M1
E3
E1
180
207
262
452
368
467
600
560
681
780
821
585
841
1240
10^{-1}
10^{-2}
10^{-3}
ALPHA-L
100
1000
ENERGY (keV)

estimate mixing ratios δ^2 for some transitions of interest. Recall that δ^2 is the ratio of the intensity of the 2^{L+1}-pole radiation to that of the 2^L-pole radiation in a mixed transition. If $\alpha_E{}^i$ is the experimental i-shell conversion coefficient, it is related to the theoretical i-shell conversion coefficients $\alpha_{Th}{}^i$ (L) and $\alpha_{Th}{}^i$ (L + 1) by

$$\alpha_E{}^i = \frac{1}{1+\delta^2}\ \alpha_{Th}{}^i\ (L) + \frac{\delta^2}{1+\delta^2}\ \alpha_{Th}{}^i\ (L+1)$$

Knowledge of the 3 α's in this equation permits the calculation of δ^2. In Table 4.3 the mixing ratios of some transitions are presented. The errors reflect the original error estimate in $\alpha_E{}^i$.

TABLE 4.3 MIXING RATIOS

ENERGY (keV)	δ^2	$Q = \delta^2/(1+\delta^2)$
180	$0.24\ ^{+0.20}_{-0.14}$	$0.19\ ^{+0.12}_{-0.10}$
262	$0.65\ ^{+0.3}_{-0.2}$	0.39 ± 0.1
585	0.065 ± 0.03	0.061 ± 0.03
600	< 0.11	< 0.09
931	$1.5\ ^{+1.3}_{-0.6}$	$0.6\ ^{+0.14}_{-0.13}$

The directional correlation measurements employed the instrumentation described in Chapter I section (v). A strong liquid source of $Hg^{195,195m}$ was prepared as follows: After vacuum sublimation of the mercury activity onto a 0.001" aluminum backing, the exposed, or active area of the backing

was cut away and dissolved in aqua regia. A few drops of this solution was transferred to a perspex tube (outer diameter 5 mm, inner diameter 3 mm). This source was then located centrally in the angular correlation apparatus of Fig. 1.10.

Only one directional correlation experiment was performed. It involved three cascades--the 585 keV-207 keV, 600 keV-180 keV, and 932 keV-180 keV. The NaI energy window (SCA 2 of Fig. 1.11) was set on the spectral region including the 207 and 180 keV photopeaks. The 585, 600, and 932 keV gamma rays were observed in the 35 cc Ge(Li) detector in coincidence with each of the three NaI detectors in the manner described in Chapter I.

In his choice of possible cascades to study by this technique the author was limited by the following considerations:

(1) Resolution of the NaI detectors. The relatively poor resolution of NaI crystals proved a hindrance when setting accurate energy windows. It was impossible, for example, to gate selectively on the 180 keV and 207 keV peaks since they were not resolved.

(2) Photopeak intensities. Many of the cascades in the decay of $Hg^{195,195m}$ which might give useful information about level spins involve gamma rays which are too weak to be studied in this way.

(3) Prior knowledge of spins and mixing ratios. A gamma-gamma directional correlation experiment can only give absolute

information about level spins if the spin of at least one level is known beforehand. Moreover, if the known spin is high, the number of spin combinations for the other two levels which are consistent with the experimental values of the correlation coefficients is often large. If in addition the mixing ratios of the gamma rays involved are not accurately known, the uncertainty in spin assignment is increased because theoretical correlation coefficients are very sensitive to these ratios. This consideration precluded the study of cascades involving the intense 560 keV line, which feeds a level of $J = 11/2^-$.

(4) Spin of intermediate state. Angular correlations of gamma rays in cascade with the 61 keV gamma ray will not yield information about the spin of the initial level, since the intermediate state (61 keV) has $J^\pi = \frac{1}{2}^+$. All such correlations are necessarily isotropic.

The above limitations effectively restricted study to the three cascades mentioned above. Even these cascades presented serious experimental difficulties. The intense 780 keV line produces compton backscatter radiation at about 190 keV. Since the NaI window is set on that energy region, the Ge(Li) spectrum in coincidence with the 180° NaI detector (NaI, No. 3 in Fig. 1.10) will show a spurious full energy peak at 780 keV-190 keV = 590 keV. This will interfere with the 585 and 600 keV

coincidences at that angle. This effect was eliminated by placing a 3.71 gm/cm^2 lead absorber in front of the Ge(Li) detector. The sensitivity of the detector to the 585, 600 and 932 keV radiations was not significantly affected, while backscatter radiation from its sensitive volume which would otherwise have reached the 180° NaI detector was absorbed.

To take full advantage of the source strength available, the experiment was done in two parts. The first part, comprising a counting time of 30 hours, was run with a source to NaI detector distance of 13.0 cm and a source to Ge(Li) detector distance of 9.2 cm. The singles counting rates at each angle were periodically monitored throughout this counting period. After 30 hours the source had decayed sufficiently to allow the source to NaI detector distance to be decreased to 10.5 cm. At the same time the three NaI detectors were permuted once cyclically --i.e. in Fig. 1.10 NaI No. 1 assumes the 180° position, No. 2 the 90° position and No. 3 the 135° position. This rearrangement would bring out any possible systematic error in the observed correlation pattern due to small differences in resolution of the NaI detectors. The counting time for the second run was 36 hours. The data from the two parts were compared after normalization to the singles rates at each angle and subtraction of random coincidences. (The latter contribution was estimated from the observed intensity of the 780 keV line at each angle whose presence can be attributed purely to accidentals.

The contribution was less than one per cent of the true coincidences.) The observed correlation patterns for the 585 keV-207 keV cascade for the two parts are shown in Fig. 4.6. Having regard to the statistical errors at each angle, the two runs can be taken as consistent. This was also the case with the other two cascades. The data from the two parts were therefore combined prior to the extraction of the coefficients A_2 and A_4. The solid line in Fig. 4.6 corresponds to these extracted values. The results, uncorrected for solid angle, are:

585-207 cascade	$A_2 = +0.06 \pm 0.016$
	$A_4 = -0.01 \pm 0.017$
600-180 cascade	$A_2 = +0.17 \pm 0.023$
	$A_4 = +0.002 \pm 0.025$
931-180 cascade	$A_2 = 0.22 \pm 0.05$
	$A_4 = 0.05 \pm 0.06$

For the source to detector distances used in this experiment the finite solid angle corrections are about 4% for A_2 and 15% for A_4. These corrections are clearly of little significance compared to the statistical errors in these quantities indicated above. The A_2 and A_4 values are used in the next section to confirm a number of parameters in the decay scheme.

(iii) Interpretation of Results

The spin of the ground state of Hg^{195} and of its metastable (40 hour) level at 176 keV have been shown to be 1/2 and 13/2 respectively by measurement of the nuclear isomer shift in the optical spectrum[11]. If one attributes the ground

Figure 4.6

"Directional correlation pattern for the 585-207 keV cascade in Au^{195}."

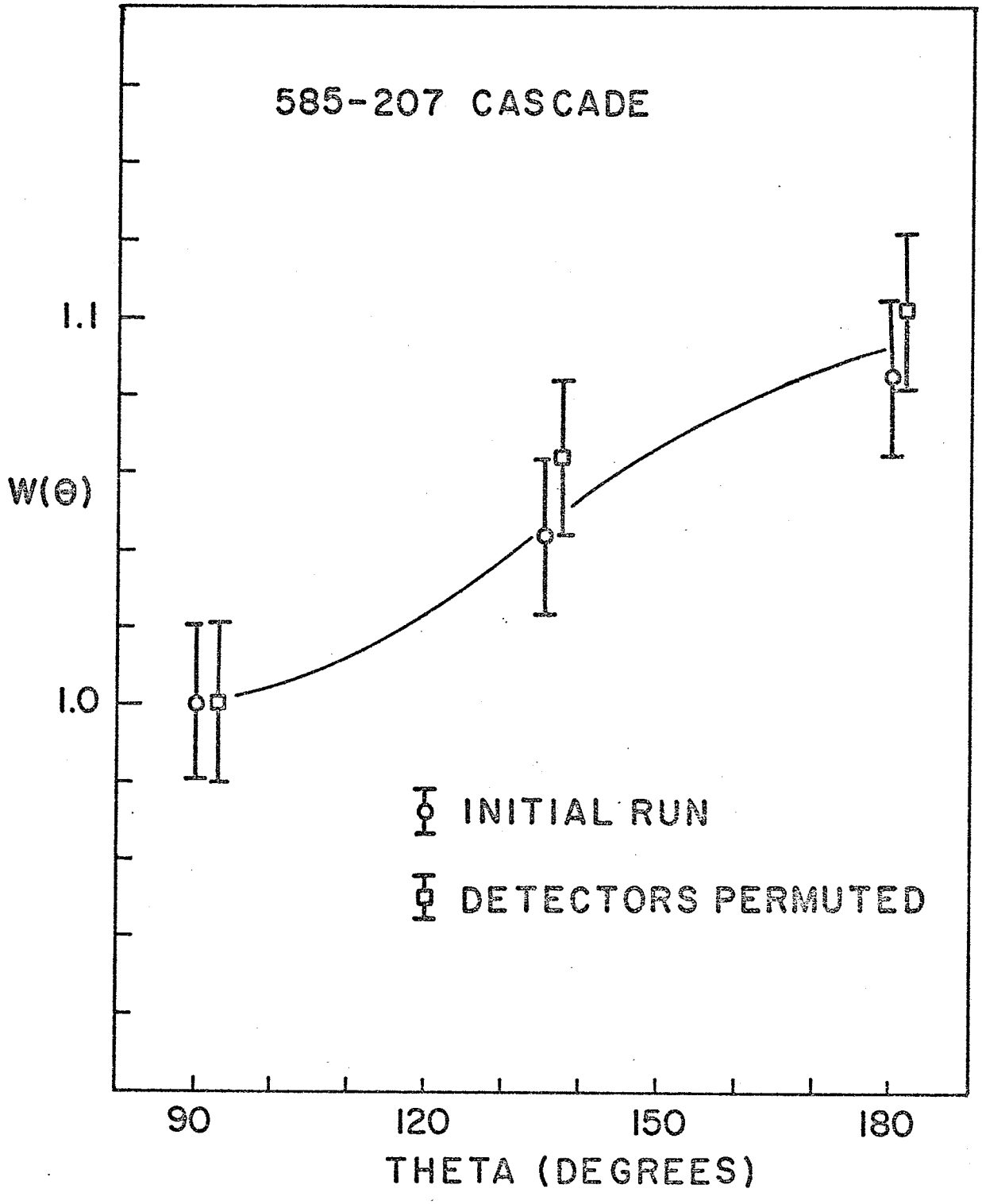
585-207 CASCADE
1.1
W(Θ)
1.0
INITIAL RUN
DETECTORS PERMUTED
90
120
150
180
THETA (DEGREES)

state spin as due to the single odd nucleon (neutron) occupying the 3 $p_{\frac{1}{2}}$ shell then the parity is negative. The accurately measured multipolarities of the gamma rays depopulating the isomeric state[9] then determine the parity of that state to be positive. The ground state spin of Au^{195} has been measured by the atomic beam magnetic resonance technique and found to be $3/2$[12]. The very plausible shell model proton configuration with this spin is $(2\ d_{3/2})^3$ thus indicating a positive parity. The existence of the 31 second isomeric state in Au^{195} at 318 keV excitation was first noted by Huber et al.[13]. This level de-excites by a cross-over ground state transition, multipolarity M4[6] and a 56.7 keV E3 transition to a 262 keV excited state.[6,9]* This suggests a $5/2^+$ assignment to the 262 keV level and an $11/2^-$ assignment to the 318 keV level. These assignments are further confirmed by comparison with the two neighbouring odd-A gold isotopes, Au^{193} and Au^{197}, which exhibit precisely the same structure. (see reference 1, Chapter III).

The first excited state in Au^{195} (at 61 keV) decays to ground by an M1, E2 transition[6] and so may have $J^\pi = \frac{1}{2}^+$, $3/2^+$ or $5/2^+$. However $J^\pi = \frac{1}{2}^+$ is most probable in view of the apparent E2 nature[6] of the 200.5 keV gamma ray which joins the 262 keV level with the 61 keV level. Again this latter

---

*See Fig. 3.1

assignment is consistent with the observed structure of the two neighbouring odd-A gold isotopes. Finally, the presence of a small E2 admixture[6,8] in the M1 transition between the 242 keV level and the 61 keV level probably indicates a $3/2^+$ character for the former.

In the spin and parity assignments to follow we shall take as a basic framework the J^π values for the ground state and first four excited states mentioned above, namely: ground state $3/2^+$, 61 keV level $1/2^+$, 242 keV level $3/2^+$, 262 keV level $5/2^+$, and 318 keV level $11/2^-$. This, it will be noted, is precisely the sequence observed in Au^{197} which is the best known of the odd-A gold isotopes. It will also be noted (see Table 4.2) that the conversion coefficient measurements performed in the present work confirm the M1, E2 character of the 180 keV and 262 keV transitions and the M4 character of the 318 keV transition and so are consistent with this framework.

Let us now restrict discussion to those levels which are in equilibrium with the $1/2^-$ Hg^{195} ground state. These levels comprise the right hand half of the level scheme of Fig. 4.9 and may be expected to have rather small angular momenta.

The 525 keV level:-

This level is depopulated by an E2 gamma ray[9] which feeds the $11/2^-$ level at 318 keV and so may have spin $7/2^-$ or $15/2^-$. The fact that the level is populated, at least

indirectly, from the Hg^{195} ground state, allows us to disregard the second possibility and take $J^{\pi} = 7/2^-$.

The 1083 keV level:-

This level de-excites to the 262 keV level ($5/2^+$) via an M1, E2 transition (821 keV) and to the 61 keV level ($\frac{1}{2}^+$) via an M1, E2 transition (1022 keV). Therefore $J^{\pi} = 3/2^+$. The multipolarity of the 841 keV de-excitation of this level is therefore M1 or M1, E2 as was mentioned in the previous section.

The 1111 keV level:-

The primary mode of de-excitation of this level is a 585 keV E1, M2 gamma ray to the 525 keV level ($7/2^-$). (Table 4.2) The possible spins are therefore $5/2^+$, $7/2^+$, $9/2^+$. However it will be shown in the next section that it is fed fairly strongly by electron capture from the $1/2^-$ ground state of Hg^{195}, so $J^{\pi} = 5/2^+$ is indicated.

The directional correlation result for the 585 keV-207 keV cascade, while consistent with $J^{\pi} = 5/2^+$, does not rule out the other two possibilities. However it does give an interesting confirmation of the presence of an M2 admixture in the 585 keV gamma ray indicated in the α_K and α_L measurements. We have (see section (i) of this chapter)

$$A_2 = A_2^{(1)} A_2^{(2)}$$

where the superscript (1) refers to the 585 keV photon and (2) to the 207 keV photon. Taking the tabulated value of $A_2^{(2)}$ for

a pure E2 transition between an initial state of spin 7/2 and a final state of spin 11/2,

$$A_2^{(2)} = -0.218$$

and the experimental value for A_2,

$$A2_{EXP} = +0.06 \pm 0.016$$

we obtain

$$A_2{}^{(1)}_{EXP} + -0.28 \pm 0.07$$

The theoretical values of $A_2^{(1)}$ are plotted as a function of Q in Fig. 4.7 for the three possible values of the spin of the 1111 keV level. In all three cases it is seen that the observed $A_2^{(1)}$ value requires a small M2 admixture. In particular, if we take the value indicated by the β-branching measurements, $J^\pi = 5/2^+$, we obtain

$$Q_{EXP} = 0.10 \pm 0.02 \text{ or}$$

$$\delta^2_{EXP} = 0.11 \pm 0.03$$

compared to the result from the conversion coefficient measurements of

$$\delta^2_{EXP} = 0.065 \pm 0.03 \quad \text{(table 4.3)}$$

Again, for $J^\pi = 5/2^+$ and Q = 0.10, the theoretical value of A4 is -0.0001, consistent with the measured value

$$A4_{EXP} = -0.01 \pm 0.017$$

The 842 keV level:-

Two relatively strong gamma rays de-excite this state. The 600 keV transition is M1(E2) and feeds the 242 keV level ($3/2^+$), and the 780 keV transition, also M1(E2) feeds the 61 keV

Figure 4.7

"Comparison of experimental and theoretical values of $A_2(1)$ for the 585-207 keV cascade. The dotted lines indicate the experimental uncertainty in the measured value of $A_2(1)$."

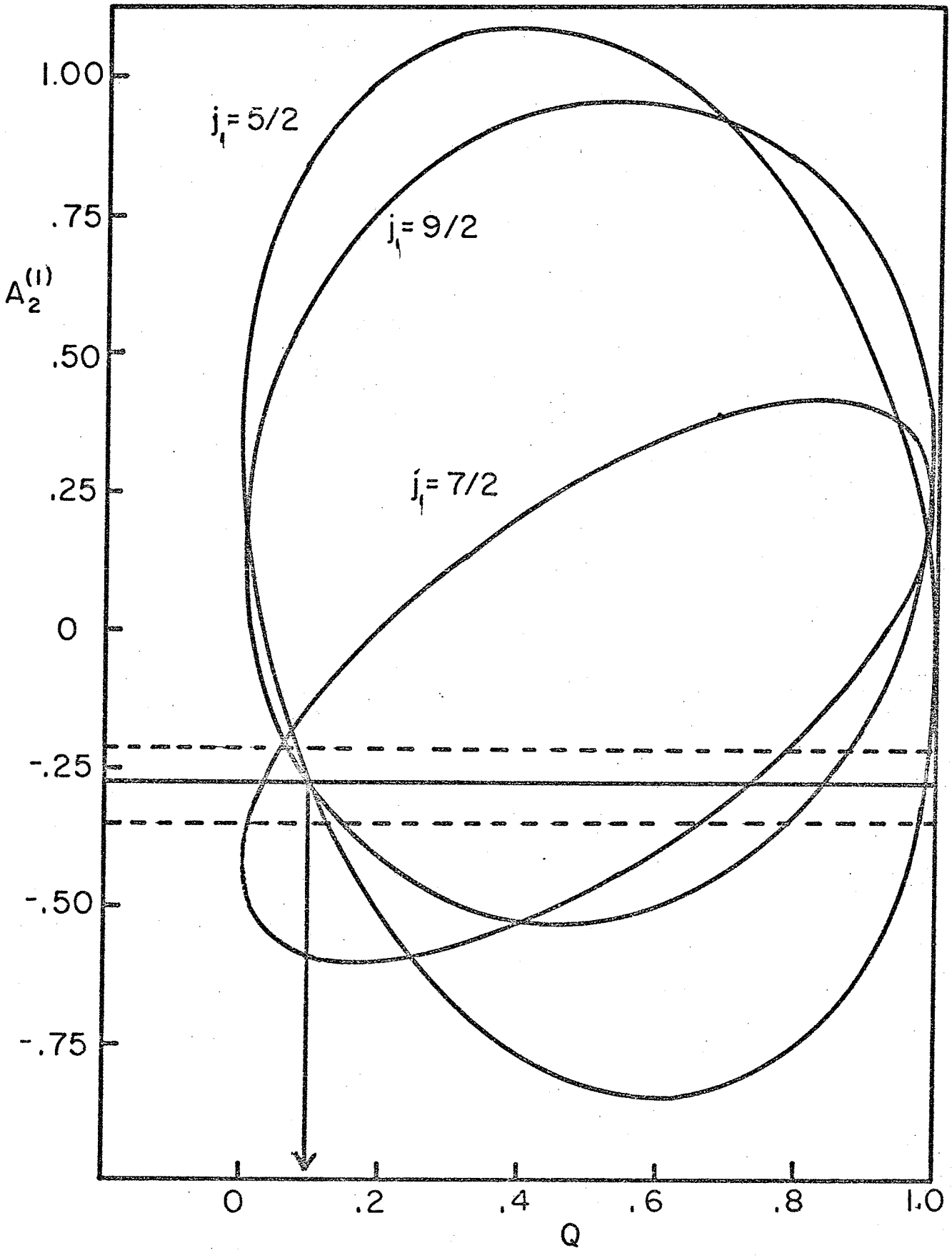
1.00
.75
.50
.25
0
-.25
-.50
-.75
$A_2^{(1)}$
$j_1 = 5/2$
$j_1 = 9/2$
$j_1 = 7/2$
0
.2
.4
.6
.8
1.0
Q

level ($1/2^+$) (see Table 4.2). Thus J^π is restricted to $1/2^+$ or $3/2^+$. The directional correlation measurements on the 600-180 keV cascade do not distinguish between the two possibilities, mainly because of the uncertainty in the mixing ratio of the 180 keV transition. The possibility of the 242 keV level being $1/2^+$ is eliminated for the correlation is not isotropic. This confirms previous assumptions.

Some information linking the sign of the mixing ratio for the 180 keV gamma ray with the spin of the 842 keV level can also be derived from the correlation work. Starting again from

$$A_2 = A_2^{(1)} A_2^{(2)}$$

where now (1) refers to the 600 keV transition, and (2) to the 180 keV transition, and taking the observed value of Q(180 keV) = $Q_{(2)}$ from Table 4.3, we have[5]

$$A_2^{(2)} = 1.00\ {}^{+0.0}_{-0.09} \qquad \delta_{(2)} < 0$$

$$\text{or } = -0.38\ {}^{+0.27}_{-0.20} \qquad \delta_{(2)} > 0$$

Hence using the measured value

$$A_{2EXP} = 0.17 \pm 0.023$$

we have

$$A_2^{(1)}{}_{EXP} = +0.17 \pm 0.03 \qquad \delta_{(2)} < 0$$

$$\text{or } = -0.5\ {}^{+0.2}_{-0.5} \qquad \delta_{(2)} > 0$$

These two values of $A_2^{(1)}{}_{EXP}$ are compared, in Fig. 4.8, with the theoretical values plotted as a function of $Q_{(1)}$ = Q(600 keV) for the two possible spin values of the 842 keV

Figure 4.8

"Comparison of experimental and theoretical values of $A_2(1)$ for the 600-180 keV cascade. The dotted lines indicate the experimental uncertainty in the measured value of $A_2(1)$."

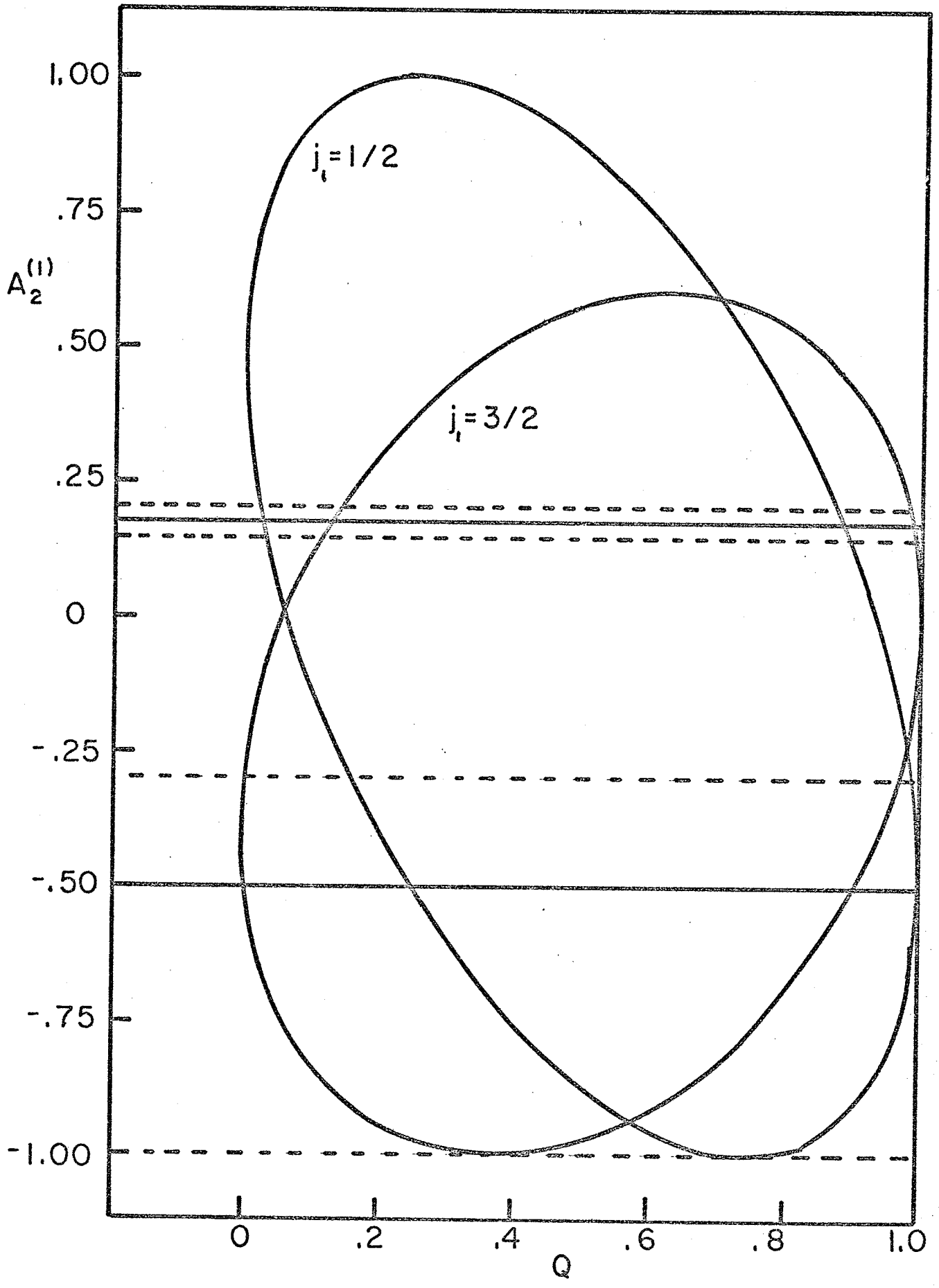
1.00
.75
$A_2^{(1)}$
.50
.25
0
-.25
-.50
-.75
-1.00
$j_1 = 1/2$
$j_1 = 3/2$
0
.2
.4
.6
.8
1.0
Q

level. Since experimentally $Q_{(1)} \leq 0.09$ (Table 4.3) we can conclude from this figure that if $\delta^{(2)} < 0$, $J^{\pi} = \frac{1}{2}^+$ and if $\delta^{(2)} > 0$, $J^{\pi} = \frac{3}{2}^+$. In either case $A4_{THEOR} = 0$, is consistent with experiment.

The 1173 keV level:-

Again referring to Table 4.2, the 1173 keV level is seen to de-excite via a 932 keV M1, E2 transition to the 242 keV level ($3/2^+$), a 1111 keV M1(E2) transition to the 61 keV level ($1/2^+$), and a 1173 keV M1(E2) transition to the ground state ($3/2^+$). The possible values of J^{π} are therefore $1/2^+$ and $3/2^+$. Once again the directional correlation measurements (on the 932-180 keV cascade) do not decide between these two alternatives. However, a similar analysis of the angular correlation data and measured Q values to the one just performed for the 842 keV level enables the following statements: If $\delta < 0$ $J^{\pi} = 1/2^+$

If $\delta > 0$ $J^{\pi} = 1/2^+$ or $3/2^+$

Since $\delta_{(2)} = \delta(180 \text{ keV})$ is a common parameter to both the analyses for the 842 keV and 1173 keV levels, we can make some additional remarks on the spins and parities of those levels, namely:

If $J^{\pi}(1173) = 3/2^+$ then $J^{\pi}(842) = 3/2^+$

If $J^{\pi}(842) = 3/2^+$ then $J^{\pi}(1173) = 1/2^+$ or $3/2^+$

If $J^{\pi}(842) = 1/2^+$ then $J(1173) = 1/2^+$

Next we shall consider briefly the "high spin" states--ie. those in equilibrium with the 40 hour isomeric state of

Hg^{195} with $J^{\pi} = 13/2^{+}$. These states are grouped on the left hand side of Fig. 4.9 In most cases unique spin assignments cannot be made to these levels unless one relies rather heavily on electron capture log ft values, estimates of which will be presented in the next section. Arguments based on log ft values are not particularly convincing because of the overlap of representative values for different degrees of forbiddenness. In this particular isotope, parity considerations assist in this interpretation as will be seen later.

One general conclusion can be drawn from the multipolarity assignments of Table 4.3, that with the possible exception of the 1605 keV level all the "high spin" states have negative parity. A spin and parity of $9/2^{-}$ may be unambiguously assigned to the 894 keV level on the basis of the multipolarities of the 368 keV transition (M1, E2 populating a $7/2^{-}$ state) and of the 575 keV transition (M1(E2) populating an $11/2^{-}$ state). The possible spins of the remaining levels consistent with the measured multipolarities are indicated on the decay scheme diagram of Fig. 4.9 of the next section.

(iv) Branching Ratios and the Final Decay Scheme

The only emitted radiations following the electron capture process (aside from neutrinos) are the atomic X-rays and Auger electrons which result from the re-adjustment of the orbital electrons after one of their number has been removed. While the study of these radiations will yield

information about the electron capture decay, such as ratios of capture rates from the K and L shells, one must resort to indirect means to measure the overall branching ratio from the parent nucleus to the various excited states of the daughter.

If I_γ is the intensity of emitted gamma rays in a nuclear transition, and α_T the total internal conversion coefficient, then we may define the total transition intensity as

$$I = I_\gamma (1 + \alpha_T)$$

Total internal conversion coefficients have been calculated or estimated for the transitions in Au^{195} with the aid of the α_K and α_L measurements presented in section (ii) of this chapter and the L-subshell ratios reported by Jung et al.[9] and by Brunner et al.[6]. The values of α_T and corresponding values of I are displayed in Table 4.4 for the transitions that follow the decay of the Hg^{195} ground state.

In the last column of the table, the transition intensities have been expressed as transitions per parent disintegration I/I_D. Here I_D is the total number of disintegrations of the parent based on the scale I_γ (780 kev) = 100 excluding direct electron capture decay to the ground state.

$$I_D = I(61 \text{ keV}) + I(262 \text{ keV}) + I(841 \text{ keV}) + I(1083 \text{ keV})$$
$$I(242 \text{ keV}) + I(1173 \text{ keV}) + I(1250 \text{ keV})$$

TABLE 4.4 TRANSITION INTENSITIES (9.5 hr)

E_γ (keV)	I_γ	α_T	I	I/I_D
61.4	84.7	12 (a)	1018	0.945
180.4	28.9	~1.2 (c)	63.8	0.0592
200.5	0.6	0.37 (b)	0.8	0.0007
207.2	29.7	0.33 (b)	39.6	0.0360
241.6	1.2	0.6 (c)	1.9	0.0018
261.7	25	0.34 (c)	33.3	0.0309
585.2	29.9	0.014(c)	30.3	0.0281
599.8	25.7	0.054(c)	27.0	0.0251
780.2	100	0.024(c)	102.4	0.0951
821.2	3.2	0.025(c)	3.3	0.0031
841.2	4.6(e) 3.1(f)	~0.01	4.6 3.1	0.0043 0.0029
911	0.7	(d)	0.7	0.0007
931.6	6.0	0.009(c)	6.0	0.0056
988	0.2	(d)	0.2	0.0002
1022	2.9	0.01 (c)	2.9	0.0027
1008	0.3	(d)	0.3	0.0003
1049	0.3	(d)	0.3	0.0003
1083	1.2	(d)	1.2	0.0011
1110.8	18.8	0.01 (c)	19.0	0.0176
1172.7	19.2	0.007(c)	19.3	0.0179
1250	0.2	(d)	0.2	0.0002

(a) After Jung et al.[9]

(b) After Brunner et al.[6]

(c) Present work

(d) Not measured

(e) De-exciting 842 keV state

(f) De-exciting 1083 keV state

From the appropriate numbers in column 4 of the table we find

$$I_D = 1018 + 33.3 + 4.6 + 1.2 + 1.9 + 19.3 + 0.2 = 1079$$

The electron capture branching ratio to a particular level can now be calculated as the difference between the total transitions out of the level and the total transitions in. The branching ratios and log ft values are given in Table 4.5.

TABLE 4.5 ELECTRON CAPTURE BRANCHING RATIOS (9.5 hr.)

LEVEL	BRANCHING RATIO	LOG ft(a)	LOG ft(b)
61 keV	0.769	6.4	6.3
242 keV	0.024	7.8	7.9
262 keV	~ 0		
525 keV	0.01	8	
842 keV	0.124	6.5	6.5
1083 keV	0.010	7.2	6.9
1111 keV	0.028	6.8	6.6
1173 keV	0.042	6.5	6.4
1250 keV	0.001	7.9	

(a) Present work

(b) Frank[7]

The log ft values in Table 4.5 were calculated as follows: First of all it was assumed that the branching ratio to the ground state was small compared to the combined branching

ratio to the excited states. Frank[7] places an upper limit of 14% on the ground state feed, based upon his gamma ray intensities and the data of Jung et al.[9] The electron capture branching ratio to the ground state of Pt^{195} from the decay of Au^{195} which involves the same spin and parity change as the decay in question is about 3%[15]. Secondly a total disintegration energy of Q_{EC} = 1500 keV was assumed (see Ref.[5] Chapter III). The K-capture branching ratio for each feed was then evaluated from the theoretical expressions for ratios of electron capture rates from the various subshells. If E_X represents the capture rate to some state of the daughter nuclide from the X'th atomic subshell, then

$$E_K = E \Big/ \left[1 + \frac{E_L}{E_K}\left(1 + \frac{E_M + \ldots}{E_L}\right)\right]$$

where $E = E_K + E_L + E_M + \ldots$

For allowed transitions, Wapstra et al.[14] give,

$$\frac{E_L}{E_K} = \frac{L_{L_I}}{L_K}\left(\frac{q_{L_I}}{q_K}\right)^2\left(1 + \frac{L_{L_{II}}}{L_{L_I}}\right)$$

where q_X is the difference between the total decay energy and the X-shell binding energy B_X

$$\text{i.e. } q_X = Q_{EC} - B_X$$

The quantities L_X are tabulated as a function of nuclear charge, as is $\frac{E_M + \ldots}{E_L}$ [14]

The equivalent expressions for first forbidden decays give

essentially the same numerical results.

Having thus obtained E_K, standard nomographs[14] were used to calculate the K-capture log ft values tabulated above.

A similar analysis was carried out for the levels in equilibrium with the 40 hour isomeric state of Hg^{195}. The transition intensities are shown in Table 4.6 and the corresponding electron capture branching ratio and log ft values in Table 4.7. Account must be taken of the fact that the isomeric state can decay by gamma emission as well as electron capture when computing partial half lives and log ft values. The branching ratio of electron capture to isomeric decay of 40 hour Hg^{195m} is easily calculated. Recall that the total number of disintegrations of the Hg^{195} ground state per hundred 780 keV gamma rays was

$$I_D(Hg^{195}) = 1079$$

We can obtain similarly, from Table 4.6, the number of disintegrations of Hg^{195m} per hundred 560 keV gamma rays

$$I_D(Hg^{195m}) = 671$$

These two numbers were compared by making use of a gamma ray singles spectrum accumulated eight days after target irradiation--i.e. ample time for the whole decay system to come to equilibrium with the 40 hour Hg^{195m} level. It was found, from this spectrum, that

$$\frac{I\gamma(780\ keV)}{I\gamma(560\ keV)} = 0.602$$

TABLE 4.6 TRANSITION INTENSITIES (40 hr)

E_γ (keV)	I_γ	α_T	I	I/I_D
172.5	0.7	0.6 (a)	1.1	0.0016
200.5	13.3	0.37(b)	18.2	0.0271
261.7	485	0.34(c)	650	0.969
279	(e)			
318	0.2	12.5 (c)	2.7	0.0040
368.4	4.9	0.14(c)	5.6	0.0083
386 }	13.4(g)	0.17(d)	15.7	0.0234
388 }	17.7(g)	0.05(a)	18.6	0.0277
452.2	2.5	0.11(d)	2.8	0.0041
466.8	3.7	0.10(c)	4.1	0.0061
526.1	6.7	0.07(c)	7.2	0.0107
560.4	100	0.06(c)	106	0.158
575	4.9	0.05(c)	5.1	0.0076
627	0.5	(e)	0.5	0.0008
665	0.7	(e)	0.7	0.0010
693	0.7	(e)	0.7	0.0010
698	1.0	0.11(f)	1.1	0.0016
681.1	2.9	0.04(c)	3.0	0.0045
727	0.7	0.09(f)	0.8	0.0012
752	0.3	(e)	0.3	0.0004
754	0.9	(e)	0.9	0.0013
853	3.8	(e)	3.8	0.0056
898	0.8	0.05(f)	0.8	0.0012

TABLE 4.6 (CONTINUED)

E_γ (keV)	I_γ	α_T	I	I/I_D
961.9	2.9	0.02(c)	3.0	0.0045
1028	1.6	(e)	1.6	0.0024
1240.1	7.5	0.01(c)	7.6	0.0113

(a) If pure E2

(b) After Brunner et al.[6]

(c) Present work

(d) If pure M1

(e) Not measured

(f) If pure M2

(g) After Frank[7]

TABLE 4.7 ELECTRON CAPTURE BRANCHING RATIOS (40 hr)

LEVEL	BRANCHING RATIO	LOG ft(a)	LOG ft(b)
318 keV	0.788	7.3	7.2
653 keV	~ 0		
706 keV	0.017	8.6	8.9
879 keV	0.137	7.4	7.5
894 keV	~ 0		
1280 keV	0.030	7.6	7.6
1346 keV	0.014	7.9	7.5
1405 keV	0.013	7.8	7.7
1559 keV	0.022	7.0	6.6
1605 keV	0.002	(c)	

(a) Present work

(b) Frank[7]

(c) L-capture only

Thus the number of disintegrations of the Hg^{195} ground state per hundred 580 keV gammas is

$$I_D\ (Hg^{195}) = 1079 \times 0.602 = 642$$

We can conclude that 49% of the Hg^{195m} decays go by isomeric transitions to the ground state, and 51% by electron capture to states in Au^{195}. This branching ratio is in agreement with that of Frank[7] and was used in the computation of the log ft values of Table 4.7.

Regarding the log ft values for electron capture from 40 hour Hg^{195m} it should be pointed out that a "first forbidden" character is very strongly indicated. It may be argued that these values do not rigorously exclude either allowed or second forbidden transitions. However, as was indicated earlier, the parities of the states fed by the Hg^{195m} level (with the possible exception of the 1605 keV state) are always negative. Therefore the electron capture transitions, beginning as they do on a state with $J^{\pi} = 13/2^{+}$ always involve a parity change, thus excluding an allowed or second forbidden character. Third forbidden transitions have log ft values of about 18 and are also clearly excluded. The spin selection rules for first forbidden transitions are

$$\Delta J = 0,\ 1,\ 2$$

so we are justified in setting a lower limit of 9/2 on the spins of the states in Au^{195} populated by electron capture from Hg^{195m}.

The final decay scheme indicated by the experiments and calculations outlined in this thesis is shown in Fig. 4.9. The basic level structure proposed by previous workers is confirmed as are the spins and parities of the levels at 61 keV, 262 keV and 318 keV reported in the literature. In addition, three new levels are proposed (excitation energy 653 keV, 1250 keV, and 1605 keV) and some 15 new gamma rays are placed. Unambiguous spins and parities have been assigned to the levels at 242 keV, 525 keV, 894 keV, 1083 keV and 1111 keV. The parities of most of the remaining levels have been fixed and fairly narrow ranges of possible spins have been suggested.

Figure 4.9

"Electron capture decay of $Hg^{195,195m}$."

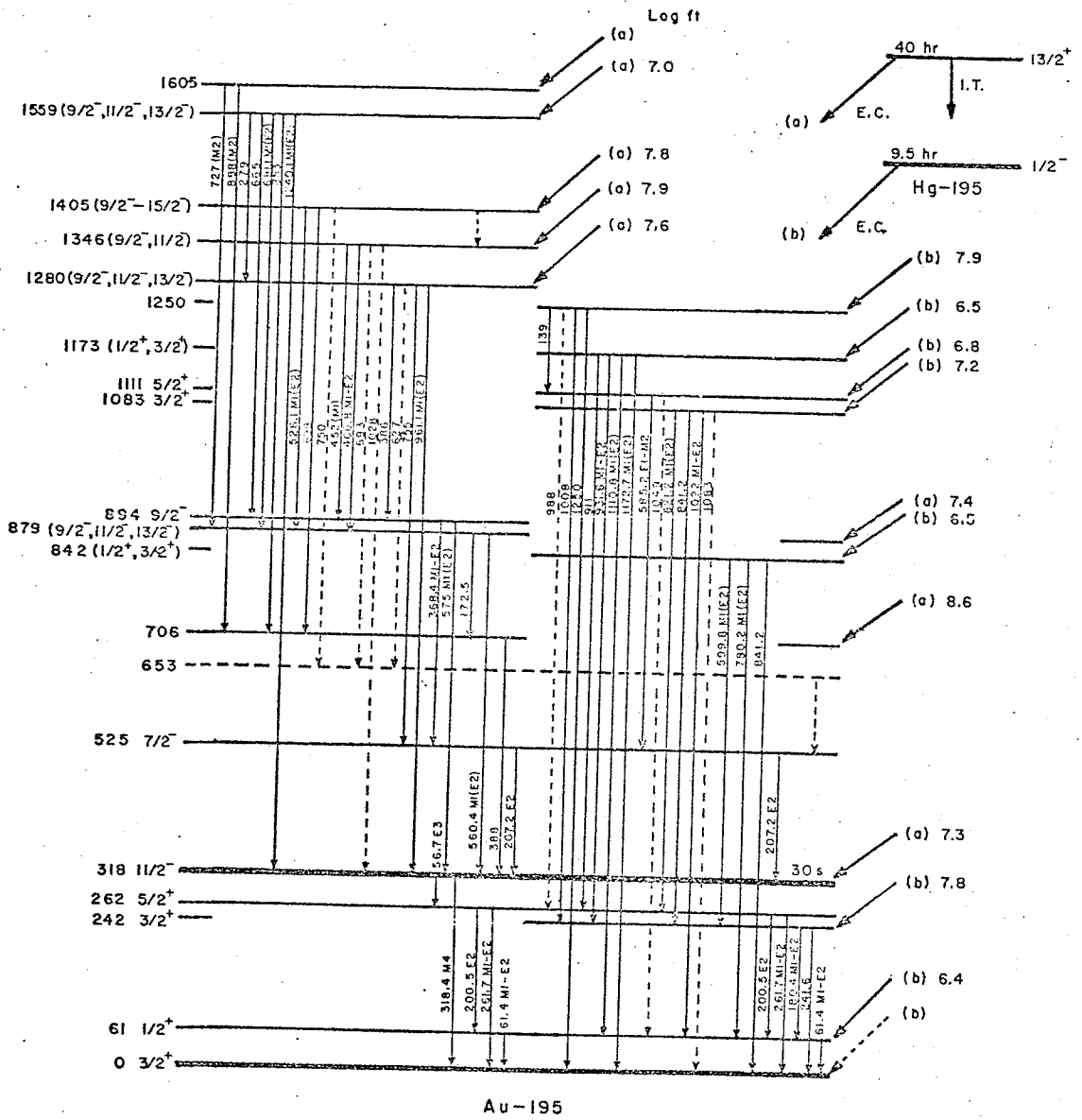
Log ft
(a)
(a) 7.0
1605
1559 (9/2⁻,11/2⁻,13/2⁻)
727 (M2)
(a) 7.8
(a) 7.9
(a) 7.6
1405 (9/2⁻–15/2⁻)
1346 (9/2⁻,11/2⁻)
1280 (9/2⁻,11/2⁻,13/2⁻)
1250
1173 (1/2⁺,3/2⁺)
1111 5/2⁺
1083 3/2⁺
894 9/2⁻
879 (9/2⁻,11/2⁻,13/2⁻)
842 (1/2⁺,3/2⁺)
706
653
525 7/2⁻
318 11/2⁻
262 5/2⁺
242 3/2⁺
61 1/2⁺
0 3/2⁺
139
988
1008
1220
911
1110.8 MI(E2)
1112.7 MI(E2)
585.5 E1-M2
1434
1439
842.2 MI(E2)
841.2
1032 MI-E2
1093
368.4 MI-E2
575 MI(E2)
172.5
999.8 MI(E2)
790.2 MI(E2)
841.2
207.2 E2
56.7 E3
560.4 MI(E2)
389
207.2 E2
318.4 M4
200.5 E2
261.7 MI-E2
61.4 MI-E2
200.5 E2
261.7 MI-E2
180.4 MI-E2
241.6
61.4 MI-E2
30 s
(a) 7.3
(b) 7.8
(b) 6.4
(b)
(b) 7.9
(b) 6.5
(b) 6.8
(b) 7.2
(a) 7.4
(b) 6.5
(a) 8.6
40 hr
13/2⁺
I.T.
(a) E.C.
9.5 hr
1/2⁻
Hg–195
(b) E.C.
Au–195

REFERENCES, CHAPTER IV

1. M. E. Rose, "Internal Conversion Coefficients" Amsterdam: North Holland Publishing Co., 1958.

2. L. A. Sliv and I. M. Band, "Coefficients of Internal Conversion of Gamma Radiation" Moscow-Leningrad: USSR Academy of Sciences, 1956 and 1958.

3. R. S. Hager and E. C. Seltzer, Nuclear Data A4, 1 (1968).

4. M. Ferentz and N. Rozenzweig, ANL-5324 (1955).

5. R. G. Arns and M. L. Weidenbeck, University of Michigan Engineering Research Institute, Technical Report 2375-3-T, 1958 (Unpublished).

6. J. Brunner, J. Halter, and P. Scherrer, Ark. Fys. 7, 335 (1958).

7. K. H. Frank, Z. Phys. 203, 71 (1967).

8. R. Joly, J. Brunner, J. Halter and O. Huber, Helv. Phys. Acta 28, 403 (1955).

9. B. Jung and J. Svedberg, Ark. Fys. 19, 447 (1961).

10. P. Reyes-Sutter and T. Suter, Arkiv Fysik 20, 415 (1961).

11. W. J. Tomlinson III, and H. H. Stroke, Phys. Rev. Lett. 8, 436 (1962).

12. I. Lindgren, Tables of Nuclear Spins and Moments, In Alpha, Beta, and Gamma Ray Spectroscopy, App. 4, K. Seigbahn, 1964.

13. O. Huber, R. Joly, P. Scherrer and N. F. Verster, Helv. Phys. Acta 25, 621 (1952).

14. A. H. Wapstra, G. J. Nijgh and R. van Lieshout, Nuclear Spectroscopy Tables, North-Holland Publishing Co., (1959).

15. J. R. Harris, G. M. Rothberg, and N. Benizerkoller, Phys. Rev. 138, 554 (1965).

CHAPTER V

DISCUSSION

Introduction

The nucleus Au^{195} probably lies within the region of spherical nuclei[1]. However the neutron number (N=116) is rather far from the nearest closed shell of N=126. Hence one would not expect to predict successfully characteristics of the low-lying excited states within the framework of the simple single particle model or the extended shell model with residual two-body forces. Rather it is likely that these excitations have a collective nature arising from the coordinated motion of many nucleons. A general theory of excitations in odd-A spherical nuclei has been developed by Kisslinger and Sorensen[2] and applied to nuclei similar to Au^{195}. In 1961 de-Shalit[3] proposed a very simple model to describe a restricted number of odd-A nuclei in which all the collective properties are attributed to the even-even core and are not specified in detail. The only assumption made is that the interaction between the core and the last odd nucleon is weak so that first order perturbation theory may be applied. It is possible, using this model, to express a large number of experimental quantities in terms of relatively few parameters and thereby examine the extent to which the properties of the odd-A nucleus are consistent with the weak coupling assumption.

Insofar as the model may be considered valid, a study of the excitations of an odd-A nucleus may give new information about the nature of collective excitations in neighbouring even-even muclei, since these nuclei should be very similar in structure to the core of the odd-A nucleus.

The isotope Au^{197} has been the most thoroughly studied of the odd-A gold nuclei, and the weak coupling model (or "core excitation" model) has been applied to it with considerable success[4,5,6]. The model of Kisslinger and Sorensen on the other hand fails to explain several essential features of that nucleus (such as the equality of B(E2) values for transitions to the ground state from three of the low-lying excited states.) It is reasonable to assume that the core excitation model will be equally successful when applied to Au^{195} which has, as we have seen, great similarities in level structure to Au^{197}. In this chapter we examine the applicability of the model to Au^{195} in the light of the present work and of previous experimental data. It should be pointed out at the outset that, while some conclusions can be drawn, the available data on Au^{195} falls far short of being sufficient for an adequate test of the model.

In section (i) the formalism of the core excitation model is developed. In section (ii) the energies, static moments, and decay rates for the first core excitation band in Au^{195} are discussed, and in section (iii) an attempt is made to extend the model to some states of higher excitation.

(i) The Core Excitation Model

As indicated in the introduction this model assumes a weak coupling between the last odd nucleon and the even-even core. The zeroth-order wave functions having definite total angular momentum are

$$|JM\rangle = \sum_{J_c j} A\,(J_c j)\; |J_c j\; JM\rangle \qquad (1)$$

The states $|J_c j\; JM\rangle$ constitute an orthonormal basis in which the Hamiltonian describing the core and particle, in the absence of an interaction between them, is diagonal. They are formed by vector coupling the single particle states $|jm\rangle$ representing the last odd nucleon in a jj-coupling orbital to the collective core states $|J_c M_c\rangle$. The coefficients $A(J_c j)$ are introduced to allow for the possibility of admixture of states with the same JM but arising from different core-particle configurations. If the model is to retain a simple intuitive meaning all but one of the terms in the summation of equation (1) should be small--i.e. one A should be close to unity and all the others zero or nearly so.

The shift in energy $\Delta E(J)$ of the state $|J\rangle$ (dropping the magnetic quantum number M for convenience) from its unperturbed zeroth-order energy can be calculated by noting that the interaction Hamiltonian between the nucleon and the core is a scalar, and hence may be expanded as a sum of scalar products of two tensor operators of rank k, $T^{(k)}(c)$ and

$T^{(k)}(p)$, which operate separately on the core and particle variables, respectively. Thus,

$$\Delta E(J) = \langle J| \sum_k (T^{(k)}(c) \cdot T^{(k)}(p))|J\rangle$$

$$= \sum_{J_c j J_c' j' k} (-)^{J_c + j' + J} A(J_c, j)\, A(J_c', j') \begin{Bmatrix} J_c' & j' & J \\ j & J_c & k \end{Bmatrix} \langle J_c' \| T^{(k)}(c) \| J_c \rangle \cdot \langle j' \| T^{(k)}(p) \| j \rangle \qquad (2)$$

Although the sum over k is extended from zero to ∞, the conditions imposed on k by the 6-j symbols limit it to only a few terms. For the monopole-monopole interaction (k=0) the 6-j symbol does not depend on J and vanishes if $J_c \neq J_c'$ and/or $j \neq j'$. If this term does not vanish the whole multiplet will be shifted by the same energy ΔE_0. If all the states $|J\rangle$ of the multiplet are "pure" states, i.e. if only one value of A for each state is different from zero and equal to 1, we can obtain from (2) the result

$$\sum_J (2J + 1)\, \Delta E_k(J) = 0 \quad \text{for } k \neq 0. \qquad (3)$$

For k = 0,

$$\Delta E_0 = \frac{\langle J_c \| T^{(0)}(c) \| J_c \rangle}{(2J_c+1)^{\frac{1}{2}}} \; \frac{\langle j \| T^{(0)}(p) \| j \rangle}{(2j+1)^{\frac{1}{2}}}$$

where we have used the algebraic expression for the 6-j symbol $\begin{Bmatrix} J_c & j & J \\ j & j_c & 0 \end{Bmatrix}$. It was pointed out by de-Shalit in his original paper[3] that under certain circumstances

$$\langle J_c \| T^{(0)}(c) \| J_c \rangle \propto (2J_c+1)^{\frac{1}{2}} \qquad (4)$$

so that E_0 would be independent of J_c. In such cases the separation between the "centers of mass" of two multiplets constructed on different core states J_c with the same single particle state j should be equal to the separation between the unperturbed multiplets. That is, the center of mass energy of a multiplet is defined by

$$E_{CM} = \frac{\sum_J (2J+1)\, E(J)}{\sum_J (2J+1)}$$

But $E(J) = E_0 + \sum_{k=1} \Delta E_k + \Delta E_0$

where E_0 is the zeroth-order energy of the multiplet. Therefore, from (3) we see that

$$E_{CM} = E_0 + \Delta E_0$$

Thus if ΔE_0 is independent of J_c,

$$E_{CM}(J_c') - E_{CM}(J_c) = E_0(J_c') - E_0(J_c)$$

If, further, the core states in the odd-A nucleus are identical with those in a neighbouring even-even nucleus, the multiplets' unperturbed energy separation ought to be identical with the separation between corresponding states in the even-even nucleus. This is the "center of gravity theorem" of Lawson and Uretzky[7]. It might be interesting to examine how (4) can arise, since the center of gravity theorem seems to be obeyed fairly closely in the case of Au^{197} when compared with Pt^{196}. In Appendix III it is shown that if the core state J_c is produced by particles

in one orbit only (the other shells being presumed closed and not contributing to the state) and if $T^{(0)}(c)$ is expandible as a sum of single particle operators, then (4) is satisfied. It is also satisfied if the J_c values arise from a collective motion superimposed on the same intrinsic structure provided $T^{(0)}(c)$ depends on the intrinsic structure only[3].

The interaction of the charge and current distribution of the nucleus with the electromagnetic field can be expanded in terms of multipole operators $\Omega^{(k)}$ (spherical tensors) and the emission rate corresponding to a given multipole operator is given by

$$T_{i\to f} = (2J_i+1)^{-1} E^{2k+1} \alpha_k |\langle f \| \Omega^{(k)} \| i \rangle|^2 \qquad (5)$$

where i and f stand for initial and final states, J_i is the angular momentum of the initial state, E is the transition energy, and α_k is a constant. To calculate $\langle f\|\Omega^{(k)}\| i\rangle$ the operator $\Omega^{(k)}$ is written as a sum of two tensor operators of the same rank k, operating separately on core and nucleon variables.

$$\Omega^{(k)} = \Omega^{(k)}(c) + \Omega^{(k)}(p)$$

The reduced transition amplitude is then

$$\langle f\|\Omega^{(k)}\| i\rangle = \sum_{J_c j J_c' j'} A(J_c j) A(J_c' j') \langle J_c' j' J' \| \Omega^{(k)}(c) + \Omega^{(k)}(p) \| J_c j J\rangle$$

$$= \sum_{J_c j J_c' j'} (-)^{j+J+k} A(J_c, j) A(J_c', j') [(2J+1)(2J'+1)]^{\frac{1}{2}}$$

$$\times \left[\begin{Bmatrix} J_c' & J_c & k \\ J & J' & j \end{Bmatrix} \langle J_c' \| \Omega^{(k)}(c) \| J_c \rangle \, \delta_{jj'} + (-)^{J'-J} \begin{Bmatrix} j' & j & k \\ J & J' & J_c \end{Bmatrix} \right.$$

$$\left. \times \langle j' \| \Omega^{(k)}(p) \| j \rangle \, \delta_{J_c J_c'} \right] \qquad (6)$$

where the "unprimed" and "primed" arguments denote initial and final states, respectively.

For the static electromagnetic moments the same expression for the reduced matrix element may be used except that we now set $J=J'$, everything else remaining the same. Thus the static moment is given by

$$\langle J\ M=J\,|\Omega^{(k)}_{0}|\ J\ M=J\rangle = \begin{pmatrix} J & k & J \\ -J & 0 & J \end{pmatrix} \langle J\|\Omega^{(k)}\|J\rangle \qquad (7)$$

the reduced matrix element being obtained from (6).

(ii) The 2^+ Core Excitation Multiplet

In Fig. 5.1 the low lying levels of Au^{195} are compared with those of the two neighbouring odd-A gold isotopes Au^{193} and Au^{197}. Also shown are the first excited states of the even-even nuclei Pt^{192}, Pt^{194}, and Pt^{196}. The choice of these latter nuclei for comparison with the "cores" of the gold nuclei is rather arbitrary. One might equally well choose even-A isotopes of Hg (obtained by adding a proton to the corresponding odd-A gold nucleus) or Os (which are the core nuclei for the one particle configuration conjugate to the $d_{\frac{3}{2}}^3$ one hole configuration of the odd-A gold isotopes). However, more experimental information is available in the case of the Pt isotopes, particularly Pt^{194}, so it is convenient to make comparisons with those nuclei. The single particle ground state proton configuration for the gold nuclei is, very probably,

$$(1\ h_{\frac{11}{2}})^{12}\ (2\ d_{\frac{3}{2}})^{3}\ (3\ s_{\frac{1}{2}})^{0}$$

Figure 5.1

Energy level systematics of odd-A gold isotopes

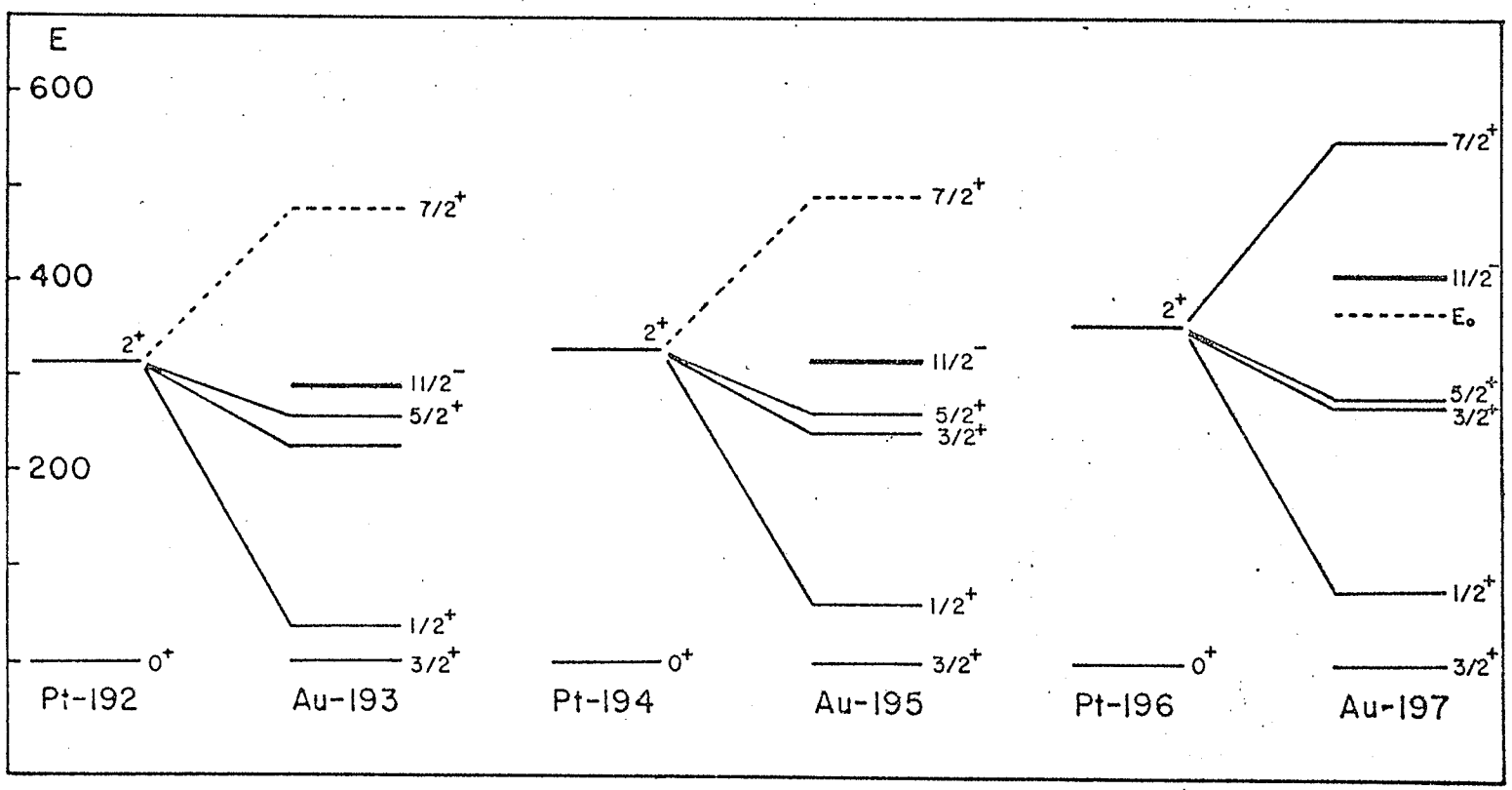
E
600
400
200
2+
7/2+
11/2−
5/2+
1/2+
0+
3/2+
Pt-192
Au-193
Pt-194
Au-195
Pt-196
Au-197
Eo

with three more protons being required to complete a major shell of Z = 82. The isomeric states $J^{\pi} = \frac{11}{2}^-$ can be generated quite plausibly on the single particle scheme by elevating a proton from the $h_{\frac{11}{2}}$ orbital to complete the d orbital leaving a hole with $J^{\pi} = \frac{11}{2}^-$. In a similar way we might account for the first excited state $J^{\pi} = \frac{1}{2}^+$ as the lowest energy state of the configuration

$$(1\ h_{\frac{11}{2}})^{12}\ (2\ d_{\frac{3}{2}})^{2}\ (3\ s_{\frac{1}{2}})^{1}$$

However the measured magnetic moment of this state in Au^{197} is $\mu(\frac{1}{2}^+) = 0.39$ nm[8] which falls well below the Schmidt value for a single $s_{\frac{1}{2}}$ proton and is extremely hard to explain on the basis of any single particle excitation. In the core excitation picture one assumes that the energy necessary to excite the first 2^+ state of the even-even core is smaller than that required to change the proton configuration. Then the $\frac{1}{2}^+$ excited state is interpreted as the first member of a quadruplet resulting from the coupling of the $d_{\frac{3}{2}}$ hole to the excited 2^+ core state. The single particle $\frac{1}{2}^+$ state must then be sought at higher excitation. The other members of the quadruplet have $J^{\pi} = \frac{3}{2}^+$, $\frac{5}{2}^+$ and $\frac{7}{2}^+$. Au^{197} (Fig. 5.1) is seen to fit very nicely into this scheme, even to the extent that the zeroth-order energy of the multiplet (E_0 = 365 keV) is very close to the energy of the first excited state in Pt^{196}. The anomalously low value of $\mu(\frac{1}{2}^+)$ has been shown to be completely consistent with the model.[4,5] Indeed an impressive amount of experimental

data on Au^{197} can be expressed consistently in terms of relatively few core excitation model parameters.[5]

Energy Levels of Au^{195}

Let us then concentrate on Au^{195} and attempt to treat it in a similar manner. The absence of a low lying $\frac{7}{2}^+$ state in the observed level spectrum need not greatly concern us. The $\frac{7}{2}^+$ state in Au^{197} is not populated in the electron capture decay of $Hg^{197,197m}$ and is observed only in coulomb excitation. Indeed electron capture from either of the parent states in Hg^{195} to a $\frac{7}{2}^+$ state in Au^{195} would involve a spin change of 3 and so be highly forbidden. If we assume the center of gravity theorem (section (i)) to hold, as seems to be the case for Au^{197}, the $\frac{7}{2}^+$ state should be at about 487 keV in Au^{195} and at about 475 keV in Au^{193} (see Fig. 5.1).

Following de-Shalit's method[5] we take the wave functions of the ground state and first three members of the 2^+ core excitation multiplet to be

$$|\tfrac{3}{2}\rangle_0 = A|0\,\tfrac{3}{2}\,\tfrac{3}{2}\rangle + \sqrt{1-A^2}\,|2\,\tfrac{3}{2}\,\tfrac{3}{2}\rangle$$

$$|\tfrac{1}{2}\rangle = |2\,\tfrac{3}{2}\,\tfrac{1}{2}\rangle$$

$$|\tfrac{3}{2}\rangle_1 = A\,|2\,\tfrac{3}{2}\,\tfrac{3}{2}\rangle - \sqrt{1-A^2}\,|0\,\tfrac{3}{2}\,\tfrac{3}{2}\rangle$$

$$|\tfrac{5}{2}\rangle = |2\,\tfrac{3}{2}\,\tfrac{5}{2}\rangle$$

We have allowed for mixing between the two $\frac{3}{2}^+$ states and have chosen the mixing parameter A such that all states are normalized and orthogonal.

The energy splittings for the multiplet, in the approximation A = 1, are given by (see section (i))

$$\Delta E(J) = \sum_{k=1}^{3} \Delta E_k(J)$$

where $$\Delta E_k(J) = \langle 2 \| T^{(k)}(c) \| 2 \rangle \langle \tfrac{3}{2} \| T^{(k)}(p) \| \tfrac{3}{2} \rangle \begin{Bmatrix} 2 & \frac{3}{2} & J \\ \frac{3}{2} & 2 & k \end{Bmatrix}$$

The sum is restricted to $k \leq 3$ by the triangulation conditions implicit in the 6j-symbol and the k=0 term has been absorbed into $\Delta E(J)$. If we replace the product of the reduced matrix elements by c_k we obtain

$$\Delta E(J) = \sum_{k=1}^{3} c_k \begin{Bmatrix} 2 & \frac{3}{2} & J \\ \frac{3}{2} & 2 & k \end{Bmatrix}$$

If we now assume that the unperturbed energy corresponds to the first excited state in Pt^{194} (E = 329 keV) we can use the three known energies of the quadruplet to calculate the c_k. The results are shown in Fig. 5.2 and are compared with the results of similar calculations for Au^{193} and Au^{197}. The dipole-dipole term (k = 1) seems to dominate, as has been noted previously.[5]

The Ground State and First Excited State

The most stringent tests of the core-excitation model involve electromagnetic transition probabilities and static moments. Unfortunately few such quantities have been measured to date for Au^{195}. Only one static moment--the dipole moment of the ground state[8] and one lifetime--that of the 61 keV level[9] have been determined experimentally. In Appendix IV the reduced M1 transition probability for the decay of the first excited state ($J^\pi = \frac{1}{2}^+$) and the magnetic moment $\mu(\frac{3}{2}^+)_0$ of the ground state are related to the g-factors g_c and g_p of the 2^+ core state

Figure 5.2

Weak coupling strengths, odd-A gold isotopes

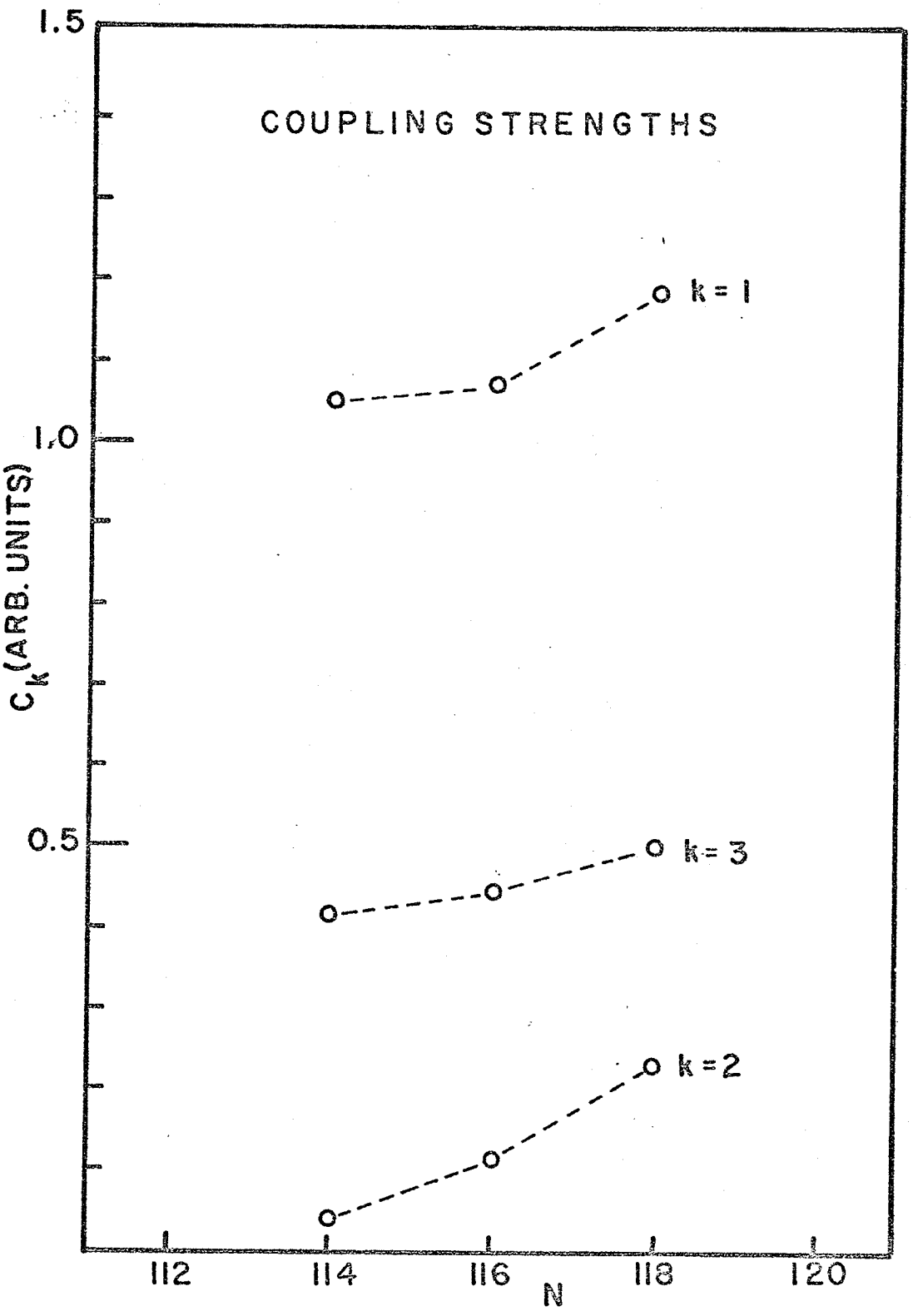
COUPLING STRENGTHS
1.5
1.0
0.5
C_k (ARB. UNITS)
k=1
k=3
k=2
112
114
116
118
120
N

and of the $d_{\frac{3}{2}}$ proton. The results are:

$$B(M1) \equiv \frac{T_{i\to f}\ (M1)}{\alpha_1\ E^3} = 3(1-A^2)(g_c - g_p)^2 \qquad (1)$$

$$\mu(\tfrac{3}{2}^+)_0 = \tfrac{3}{2}g_p + \tfrac{6}{5}(1-A^2)(g_c - g_p) \qquad (2)$$

The quantities on the left are known experimentally and the single particle estimate $g_p = 0.083$ may be assumed.[5] Solving for g_c we obtain

$$g_c = g_p + \frac{\frac{2}{5}B(M1)}{\mu(\frac{3}{2}^+)_0 - g_p} \qquad (3)$$

Experimentally, $\mu(\frac{3}{2}^+)_0 = \pm\ 0.15$ nm[8]

$$B(M1) = \frac{1}{\alpha_1 E^3}\ \frac{1}{1+\delta^2}\ \frac{0.693}{T_{\frac{1}{2}}(1+\alpha_T)} = 0.017 \pm 0.003$$

where $T_{\frac{1}{2}} = 3.9 \times 10^{-9}$ sec and δ^2 and α_T were calculated from the L-subshell measurements of Jung et al. (ref. 9 chapter IV). If E is in MeV

$$\alpha_1 = 4.2 \times 10^{12}\ \text{MeV}^{-3}\ \text{sec}^{-1}$$

The error in B(M1) reflects the uncertainty in α_T, δ^2 and $T_{\frac{1}{2}}$.

For $\mu(\frac{3}{2}^+)_0 = +\ 0.15$ nm, $g_c = +\ 0.36$ and $A^2 = +\ 0.93$

For $\mu(\frac{3}{2}^+)_0 = -\ 0.15$ nm, $g_c = +\ 0.058$ and $A^2 = -\ 18$

Clearly only the first set of values is acceptable within the framework of the model and a measurement of the sign of $\mu(\frac{3}{2}^+)_0$ would constitute a good test of the model's validity. The results for $\mu(\frac{3}{2}^+)_0 > 0$ are encouraging for the value of g_c is quite close to the measured value of the g-factor of the 329 keV 2^+ state in Pt^{194} [10,11]. Moreover $A^2 = 0.93$ is precisely that value of the mixing parameter which gives the best fit to the

core excitation model of available data on the Au^{197} nucleus. (It should be pointed out that the agreement may be partly fortuitous. The second term in equation (3) tends to infinity as A^2 tends to unity, so g_c is rather sensitive to the experimental value of $\mu(\frac{3}{2}^+)_0$.)

One striking consequence of the core excitation model, noted earlier, is that reduced E2 transition probabilities from the quadruplet states to the ground state should all be equal (except for de-excitations from the $\frac{3}{2}^+$ state where interference terms occur.) and should compare closely with corresponding B(E2) values in neighbouring even-even nuclei. This result follows very simply from equation (6) of section (i). The effect is seen very clearly in the Au^{197} nucleus and constitutes probably the most convincing evidence in favour of the model. The best we can do with the existing data on Au^{195} is to compare the B(E2) value for the $|\frac{1}{2}^+\rangle \longrightarrow |\frac{3}{2}^+\rangle_0$ transition with that for the de-excitation of the 329 keV state in Pt^{194}. We obtain for the former,

$$B(E2)[Au^{195}] = \frac{T_{i\to f}(E2)}{\alpha_2 E^5} = \frac{1}{\alpha_2 E^5}\,\frac{\delta^2}{1+\delta^2}\,\frac{0.693}{T_{\frac{1}{2}}(1+\alpha_T)}$$

$$= 0.27 \pm 0.06$$

while for the latter,

$$B(E2)[Pt^{194}] = 0.35^{12} \quad \text{(no error quoted)}$$

Here $\alpha_2 = 1.23 \times 10^{13}$ MeV^{-5} sec^{-1} if E is in MeV. Again the agreement is a good confirmation of the weak coupling hypothesis.

The lack of information on the half lives of the remaining members of the first core excitation multiplet in Au^{195} restricts further comparison of model and experiment to mixing and branching ratios--i.e. quantities independent of $T_{1/2}$. Consider the mixing ratio δ^2 for the transition $|\frac{3}{2}\rangle_1 \longrightarrow |\frac{1}{2}\rangle$. It is readily seen that

$$\delta^2 = E^2 \frac{a_2}{a_1} \left| \frac{\langle f \| \Omega^{(2)} \| i \rangle}{\langle f \| \Omega^{(1)} \| i \rangle} \right|^2$$ in the notation of equation (5) section (i). The reduced matrix elements for the transition are derived in Appendix IV. From equations (3) and (4) in the appendix,

$$\frac{\langle f \| \Omega^{(2)} \| i \rangle}{\langle f \| \Omega^{(1)} \| i \rangle} = \frac{1}{5\sqrt{6}} \left(\frac{\sqrt{7}\langle 2 \| \Omega^{(2)}(c) \| 2 \rangle + \sqrt{2}\langle \frac{3}{2} \| \Omega^{(2)}(p) \| \frac{3}{2} \rangle}{(g_c - g_p)} \right)$$

$$- \frac{1}{5}\sqrt{\frac{5}{3}} \frac{\sqrt{1-A^2}}{A} \frac{\langle 2 \| \Omega^{(2)}(c) \| 0 \rangle}{(g_c - g_p)} \qquad (4)$$

If the reduced matrix elements in this expression can be estimated, we can predict not only δ^2 but the sign of δ as well. This in turn will aid in removing the ambiguities in the interpretation of the angular correlation results of chapter IV. In obtaining this sign care must be taken that the definition of δ used in the interpretation of the experimental data is consistent with that used in the model. This has been emphasized by Biedenharn and Rose.[13] According to the definition of δ in chapter IV, for the <u>second</u> transition in a two gamma ray cascade,

$$\delta = \frac{\langle j \| L+1, \pi \| j_2 \rangle}{\langle j \| L, \pi \| j_2 \rangle} \qquad (5)$$

where j is the spin of the initial (intermediate) state and j_2 that of the final state. In equation (4) the roles of initial and final states are therefore reversed from equation (5). Hence we are more correctly interested in the sign of

$$\frac{\langle i\|\Omega^{(2)}\|f\rangle}{\langle i\|\Omega^{(1)}\|f\rangle}$$

The reduced matrix elements satisfy[14]

$$\langle i\|\Omega^{(k)}\|f\rangle(2J_f+1)^{\frac{1}{2}} = (-)^{J_i-J_f+k}\langle f\|\Omega^{(k)}\|i\rangle^*\ (2J_i+1)^{\frac{1}{2}}$$

Therefore $\frac{\langle i\|\Omega^{(2)}\|f\rangle}{\langle i\|\Omega^{(1)}\|f\rangle} = \frac{(-1)^2}{(-1)^1}\frac{\langle f\|\Omega^{(2)}\|i\rangle^*}{\langle f\|\Omega^{(1)}\|i\rangle^*} = -\frac{\langle f\|\Omega^{(2)}\|i\rangle}{\langle f\|\Omega^{(1)}\|i\rangle}$

using the reality of the reduced matrix elements. Thus we conclude that δ is positive (negative) if $\langle f\|\Omega^{(2)}\|i\rangle / \langle f\|\Omega^{(1)}\|i\rangle$ is negative (positive).

The matrix element $\langle\frac{3}{2}\|\Omega^{(2)}(p)\|\frac{3}{2}\rangle$ is related to the quadrupole moment of a single proton in a $d_{\frac{3}{2}}$ orbital by the defining equation

$$Q(\text{barns}) \equiv \sqrt{\frac{16\pi}{5}}\ \langle j=\tfrac{3}{2}m=\tfrac{3}{2}|\Omega^{(2)}_0(p)|j=\tfrac{3}{2}m=\tfrac{3}{2}\rangle = \frac{2}{5}\sqrt{\pi}\,\langle\tfrac{3}{2}\|\Omega^{(2)}(p)\|\tfrac{3}{2}\rangle$$

The single particle estimate[1] for a $d_{\frac{3}{2}}$ proton is

$$Q_{sp}(\text{barns}) = -\langle r^2\rangle\,\frac{2j-1}{2j+1} = -0.21$$

if we take $r = 1.25A^{1/3}$ fm as the average radius of the proton in its 2 $d_{\frac{3}{2}}$ shell.[5] In Au^{195} we are concerned with the configuration $d^3_{\frac{3}{2}}$ which is the conjugate hole configuration to that of a single $d_{\frac{3}{2}}$ proton. Since the static moment under consideration is of even order, we must reverse the sign of

the single particle estimate[15] thus obtaining

$$\langle \tfrac{3}{2} \| \Omega^{(2)}(p) \| \tfrac{3}{2} \rangle = +0.30$$

de-Shalit[5] has calculated the quadrupole moment of the 2+ core state in Au^{197} as 1.2 barns. If we take this to be the value for the Au^{195} core

$$\langle 2 \| \Omega^{(2)}(c) \| 2 \rangle \approx +1.6$$

Finally, from the B(E2) value obtained previously for the 2+→0+ core transition in Au^{195},

$$\langle 0 \| \Omega^{(2)}(c) \| 2 \rangle = \pm 1.16$$

Using these estimates and the values of g_c, g_p and A^2 already obtained,

$$\frac{\langle f \| \Omega^{(2)} \| i \rangle}{\langle f \| \Omega^{(1)} \| i \rangle} = 1.07 \text{ or } 1.66 \text{ depending}$$

on whether $A\langle 0 \| \Omega^{(2)}(c) \| 2 \rangle$ is positive or negative. In either case $\delta<0$ and, referring back to the angular correlation results of chapter IV we see that a spin of $\frac{1}{2}$ is indicated for the 842 keV level and also for the 1173 keV level. If the spin of these two levels is indeed $\frac{1}{2}$ rather than $\frac{3}{2}$ this would account for the observed absence of M1 branching from them to the 262 keV level ($J^\pi = \frac{5}{2}^+$) which would otherwise be expected on the basis of the model. Using the above figures, we calculate the mixing ratio to be

$$\delta^2 = 0.11 \text{ if } A\langle 0 \| \Omega^{(2)}(c) \| 2 \rangle > 0$$

$$0.26 \text{ if } A\langle 0 \| \Omega^{(2)}(c) \| 2 \rangle < 0$$

both of which are consistent with the experimental value in table 4.3.

Two modes of electric quadrupole de-excitation have been observed for the 262 keV state in Au^{195}, namely the 200.5 keV E2 transition to the 61 keV state and an E2 admixture in the 261.7 keV ground state transition. The branching ratio between these two modes is just

$$\frac{T(E2)^{(1)}}{T(E2)(2)} = Q^{(1)} \frac{I^{(1)}}{I(2)}$$

where superscripts (1) and (2) refer to the 261.7 and 200.5 keV transitions respectively, $Q = \delta^2/(1+\delta^2)$, and $I^{(i)}$ is the gamma ray intensity of the i'th transition. From the experimental values of these quantities (chapters III and IV)

$$\frac{T(E2)^{(1)}}{T(E2)(2)} = 19.5 \pm 5$$

while from equation (5) section (i) and equations (5) and (6) Appendix IV,

$$\frac{T(E2)^{(1)}}{T(E2)(2)} = \left(\frac{E^{(1)}}{E(2)}\right)^5 \left| \frac{\langle f \| \Omega^{(2)} \| i \rangle^{(1)}}{\langle f \| \Omega^{(2)} \| i \rangle (2)} \right|^2$$

$$= \left(\frac{E^{(1)}}{E(2)}\right)^5 \frac{50\left\{\frac{1}{\sqrt{5}} A\langle 0\|\Omega^{(2)}(c)\|2\rangle + \sqrt{1-A^2}\left[\frac{1}{5}\langle \tfrac{3}{2}\|\Omega^{(2)}(p)\|\tfrac{3}{2}\rangle - \frac{1}{\sqrt{14}}\langle 2\|\Omega^{(2)}(c)\|2\rangle\right]\right.}{\left\{\langle 2\|\Omega^{(2)}(c)\|2\rangle + \sqrt{\tfrac{7}{2}}\langle \tfrac{3}{2}\|\Omega^{(2)}(p)\|\tfrac{3}{2}\rangle\right\}^2}$$

Substituting the previous estimates for the reduced matrix elements into this expression,

$$\frac{T(E2)^{(1)}}{T(E2)(2)} = 24 \text{ if } A\langle 0\|\Omega^{(2)}(c)\|2\rangle > 0$$
$$= 69 \text{ if } A\langle 0\|\Omega^{(2)}(c)\|2\rangle < 0$$

The agreement with experiment is thus good for the positive value of $A\langle 0\|\Omega^{(2)}(c)\|2\rangle$ and quite poor for the negative value.

The calculations and comparisons discussed in this section are summarized in table 5.1.

TABLE 5.1 CORE EXCITATION MODEL CALCULATIONS

QUANTITY	CALC. VALUE Au^{195}	MEAS. VALUE Au^{195}	MEAS. VALUE Pt^{194}	CALC. VALUE Au^{197}	MEAS. VALUE Au^{197}
A^2	0.93			0.933	
g_c	0.36		0.2→0.3	0.64	
$B(E2)\left[2^+ \to 0^+\right]$		0.27 ± 0.06	0.35		0.22
$\delta^2\left[\lvert\frac{3}{2}\rangle_1 \to \lvert\frac{1}{2}\rangle\right]$	0.11	$0.24\ ^{+0.20}_{-0.14}$		0.05	0.33 ± 0.2
δ	< 0				
$T(E2)^{(1)}/T(E2)^{(2)}$	24	19.5 ± 5			

(iii) Other Core Excitation Multiplets in Au^{195}

In contrast to Au^{197}, levels in Au^{195} have been observed with energies extending well above the first core excitation multiplet (see Fig. 4.9). We shall examine in this section the extent to which the simple weak coupling picture is consistent with the properties of these levels.

First a brief word about the negative parity, high spin states populated by the 40 hour isomer Hg^{195m}. The $\frac{11}{2}^-$ state at 318 keV is probably a single hole excitation as indicated in section (ii) and so could be represented by the core excitation model wave function $\lvert 0, \frac{11}{2}\frac{11}{2}\rangle$. It is not unreasonable then to couple this $\frac{11}{2}^-$ hole state to the first 2^+ core state to produce wave functions of the type $\lvert 2\ \frac{11}{2}\ J\rangle$ having $J^\pi = \frac{7}{2}^-, \frac{9}{2}^-, \frac{11}{2}^-, \frac{13}{2}^-$ and $\frac{15}{2}^-$. This may well acount for the $\frac{7}{2}^-$ level at 525 keV and

for some of the other high spin states observed. Obviously more information is required on the spins before this idea can be persued much further. We can however predict the half life of the 525 keV level with the assumption that its wave function is indeed $|2\ \frac{11}{2}\ \frac{7}{2}\rangle$. This state de-excites via a single E2 transition (E_γ = 207 keV) to the $\frac{11}{2}^-$ state at 318 keV. Equations (5) and (6) of section (i) may be used to evaluate the transition rate. We obtain

$$T_{i\to f} = \frac{1}{2J_i+1}\, a_2\, E^5\, \frac{8}{5}\, |\langle 0 \| \Omega^{(2)}(c) \| 2\rangle|^2 = 12.6 \times 10^8 \text{ sec}$$

corresponding to a half life of

$$T_{\frac{1}{2}} = \frac{0.693}{T_{i\to f}(1+a_T)} = 4.0 \times 10^{-10} \text{ sec for } a_T = 0.33$$

A direct measurement of the half life of this state would thus be of interest.

The spins of the positive parity states at higher excitations are known somewhat better. They are shown in Fig. 5.3. (As was indicated in section (ii) the sign of δ(180 keV) calculated with the wave functions of the first core excitation multiplet taken in conjunction with the angular correlation data of chapter IV points to a spin of $\frac{1}{2}$ for both the 842 and 1173 keV levels). Also shown in the figure are the first two excited states of Pt^{194} having, it will be noticed, the same spin and parity. It is tempting to take the 842, 1083 and 1111 keV states as belonging to a second quadruplet built on the <u>second</u> 2^+ core state and to assume again that the missing

Figure 5.3

The positive parity states in Au^{195}

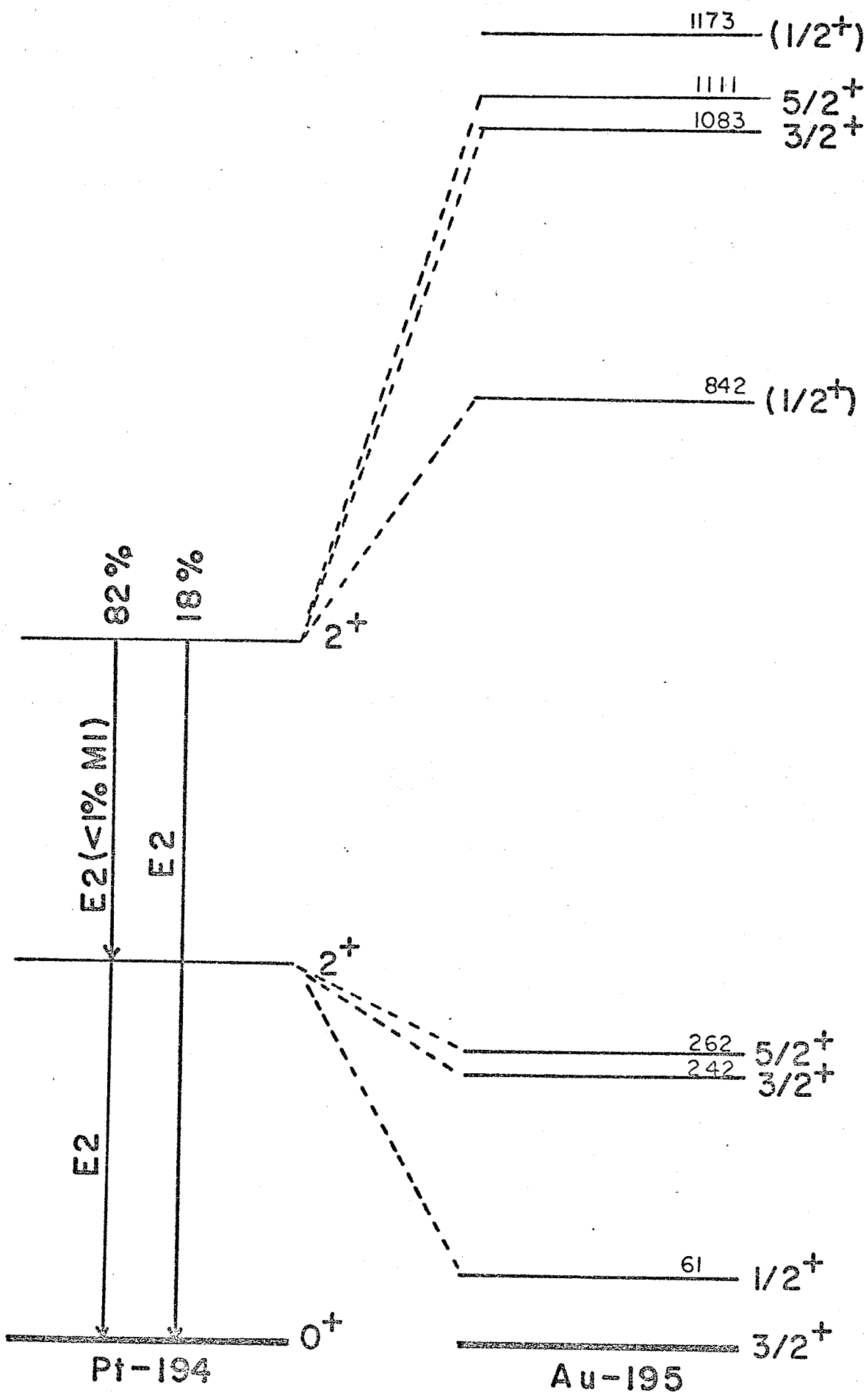
1173
(1/2+)
1111
5/2+
1083
3/2+
842
(1/2+)
82%
18%
2+
E2(<1% M1)
E2
2+
262
5/2+
242
3/2+
E2
61
1/2+
0+
3/2+
Pt-194
Au-195

$\frac{7}{2}^+$ member is not populated due to β-decay selection rules. It is evident however that insofar as Pt^{194} may be considered equivalent to the Au^{195} core the center of gravity theorem is failing rather badly for this multiplet. Staying within the framework of the simple weak coupling model we might account for this large shift in the center of gravity by allowing for substantial admixtures of other core-particle configurations in the wave functions of these levels. Another such configuration will in fact give rise to the level structure of Fig. 5.3. The 842 keV state might be attributed to the single particle proton configuration

$$(2\,d_{\frac{3}{2}})^2\ (3\,s_{\frac{1}{2}})^1$$

The 1083 and 1111 keV states could then be a doublet formed by coupling the $s_{\frac{1}{2}}$ proton with the <u>first</u> 2^+ core state. If we allow for arbitrary mixing between both these core particle configurations, a possible set of wave functions is:

842 keV state $B|0\ \frac{1}{2}\ \frac{1}{2}\rangle + \sqrt{1-B^2}\,|2^*\ \frac{3}{2}\ \frac{1}{2}\rangle$

1083 keV state $C|2\ \frac{1}{2}\ \frac{3}{2}\rangle + \sqrt{1-C^2}\,|2^*\ \frac{3}{2}\ \frac{3}{2}\rangle$

1111 keV state $D|2\ \frac{1}{2}\ \frac{5}{2}\rangle + \sqrt{1-D^2}\,|2^*\ \frac{3}{2}\ \frac{5}{2}\rangle$

1173 keV state $B|2^*\ \frac{3}{2}\ \frac{1}{2}\rangle - \sqrt{1-B^2}\,|0\ \ \frac{1}{2}\ \frac{1}{2}\rangle$

The asterisk denotes a state built on the second 2^+ core state.

No lifetime measurements exist for these four levels and most of the intense gamma rays depopulating them are predominantly M1. Hence the only good experimental data available with which to test the validity of the above wave

functions are M1 branching ratios. Consider then the 842 keV level. Three M1 decay channels are available--to the ground state and to the first two excited states at 61 keV and 242 keV. (M1 transitions to the 262 keV level ($J^\pi = \frac{5}{2}^+$) are of course forbidden.) Reduced M1 transition matrix elements are readily calculated with the above wave functions. (See the derivation of equation (7) in Appendix IV) The results are:

To the ground state (E_γ = 842 keV)

$$\langle f\|\Omega^{(1)}\|i\rangle = \sqrt{2(1-A^2)(1-B^2)}\left[\frac{1}{\sqrt{10}}\langle 2\|\Omega^{(1)}(c)\|2^*\rangle - \sqrt{3}\, g_p\right] \quad (1)$$

To the 61 keV state (E_γ = 780 keV)

$$\langle f\|\Omega^{(1)}\|i\rangle = \sqrt{(1-B^2)/5}\left[\langle 2\|\Omega^{(1)}(c)\|2^*\rangle - \sqrt{\frac{15}{2}}\, g_p\right] \quad (2)$$

To the 242 keV state (E_γ = 600 keV)

$$\langle f\|\Omega^{(1)}\|i\rangle = A\sqrt{2(1-B^2)}\left[\frac{1}{\sqrt{10}}\langle 2\|\Omega^{(1)}(c)\|2^*\rangle - \sqrt{3}\, g_p\right] \quad (3)$$

where $\langle 2\|\Omega^{(1)}(c)\|2^*\rangle$ is the reduced M1 transition matrix element connecting the two 2^+ core states. The M1 branching ratios from the 842 keV level are thus independent of B (provided $B \neq 1$) and the branching ratio between the ground state and the 242 keV state is a function of A^2 only

$$\frac{T(M1)(842\text{ keV})}{T(M1)(600\text{ keV})} = \left(\frac{842}{600}\right)^3 \frac{1-A^2}{A^2} = 0.21 \text{ for } A^2 = 0.93$$

Experimentally $\frac{T(M1)(842\text{ keV})}{T(M1)(600\text{ keV})} \leq 0.18$ (see chapter III)

The upper limit obtains only if the 842 keV transition is pure M1. The mixing ratio of this gamma ray could not be measured due to interference from another gamma ray of the same energy.

In order to calculate T(M1)(780 keV)/T(M1)(600 keV)

we must consider the matrix element $\langle 2\|\Omega^{(1)}(c)\|2^*\rangle$. It should in fact be quite small. If the first and second 2^+ core states are, respectively, one and two quadrupole phonon excitations, then $\langle 2\|\Omega^{(1)}(c)\|2^*\rangle \equiv 0$ because the magnetic dipole operator (a tensor of rank 1) cannot annihilate a quadrupole phonon. Classically, the nucleus in its excited state is performing quadrupole oscillations about a spherical equilibrium distribution and therefore will de-excite by emitting quadrupole radiation. Butt et al.[16] place an upper limit of 1% on any possible M1 admixture in the decay of the 622 keV state in Pt^{194} to the 329 keV state. This corresponds to an upper limit of 0.06 on the magnitude of the reduced matrix element. We shall therefore neglect $\langle 2\|\Omega^{(1)}(c)\|2^*\rangle$ in comparison to $\sqrt{\frac{15}{2}}\,g_p$ and $\sqrt{30}\,g_p$ (see equations (2) and (3) With this assumption,

$$\frac{T(M1)(780\text{ keV})}{T(M1)(600\text{ keV})} = \left(\frac{780}{600}\right)^3 \frac{1}{4A^2} = 0.59 \text{ for } A^2 = 0.93$$

Experimentally $\frac{T(M1)(780\text{ keV})}{T(M1)(600\text{ keV})} = 4.0 \pm 0.5$ (see chapter III)

The agreement with experiment is thus rather poor. The high branching ratio to the 61 keV state might be due to a small amount of mixing between the 61 and 842 keV states. The reduced M1 matrix element for the 780 keV transition would then involve the parameter $\langle \frac{1}{2}\|\Omega^{(1)}(p)\|\frac{1}{2}\rangle = 6.85$ (single particle value) which is much larger than the matrix elements we have been concerned with up to now. The branching ratio would then

be seriously affected even for small admixtures of this type. However the introduction of another mixing parameter precludes further quantitative comparison with experiment and so will not be dealt with here.

The 1173 keV state, to which we have assigned the wave function conjugate to that of the 842 keV state, also decays by strong M1 transitions to the lowest 3 states of Au^{195}. The predicted M1 branching ratios to these three states are essentially the same as for the 842 keV level (aside from the E^3 factor). The agreement with experiment is again quite poor. The results for both the 842 and 1173 keV levels are summarized in table 5.2.

TABLE 5.2 M1 BRANCHING RATIOS FROM 842 keV AND 1173 keV LEVELS

LEVEL	BRANCHING RATIO	CALCULATED VALUE	EXPERIMENTAL VALUE
842 keV	$\frac{T(M1)(842)}{T(M1)(600)}$	0.21	≤ 0.18
	$\frac{T(M1)(780)}{T(M1)(600)}$	0.59	4.0 ± 0.5
1173 keV	$\frac{T(M1)(1173)}{T(M1)(931)}$	0.15	8 ± 4
	$\frac{T(M1)(1111)}{T(M1)(931)}$	0.46	8 ± 4

(iv) Conclusions

The calculations and comparisons carried out in section (ii) indicate that, at least as far as the available data are concerned, the low lying excited states of Au^{195} can be described by the core excitation model. Considerably more

experimental data, particularly accurate half-life measurements, are required before the model can be tested adequately. Also needed is a search for a low lying $\frac{7}{2}^+$ state with excitation ~0.5 MeV since its existence is predicted by and is essential to the weak coupling hypothesis. The energies and spins of some states at higher excitation appear, at least qualitatively, to exhibit core-particle multiplet structure. However as shown in section (iii) the simple wave functions of the core excitation model do not explain adequately the gamma ray branching ratios from these states.

REFERENCES, CHAPTER V

1. M. A. Preston, Physics of the Nucleus, p. 155, Addison-Wesley (1963).

2. L. S. Kisslinger and R. A. Sorensen, Rev. Mod. Phys. 25, 853 (1963).

3. A. de-Shalit, Phys. Rev. 122, 1530 (1961).

4. A. Braunstein and A. de-Shalit, Phys. Lett. 1, 264 (1962).

5. A. de-Shalit, Phys. Lett. 15, 170 (1965).

6. J. M. McKinley and P. M. Rinard, Nucl. Phys. 79, 159 (1965).

7. R. D. Lawson and J. L. Uretsky, Phys. Rev. 108, 1300 (1957).

8. I. Lindgren, Table of Nuclear Spins and Moments, in Alpha, Beta, and Gamma Ray Spectroscopy, App. 4, edited by K. Siegbahn, 1964.

9. P. Reyes-Sutter and T. Suter, Arkiv Fysik 20, 187 (1961).

10. L. Kesthelyi, I. Berkes, I. Dezsi, and L. Pocs, Nucl. Phys. 71, 662 (1965).

11. H. Spehl, O. Klepper, and H. Rophe, Nucl. Phys. 63, 477 (1965).

12. P. H. Stelson and F. K. McGowan, Phys. Rev. 99, 112 (1955).

13. L. C. Biedenharn and M. E. Rose, Rev. Mod. Phys. 25, 729 (1953).

14. H. Fraunfelder and R. M. Steffen, Alpha, Beta, and Gamma Ray Spectroscopy, Ed. K. Siegbahn (1964).

15. A. de-Shalit and I. Talmi, Nuclear Shell Theory, p. 234, Academic Press, (1963).

16. D. K. Butt, and P. W. Nicholson, Nucl. Phys. 31, 460 (1962).

APPENDIX I

DE-EXCITATIONS OF THE 262 keV LEVEL IN Au^{195}

Both the 9.5 hour ground state and 40 hour isomeric state of Hg^{195} are populated by the (p, 3n) reaction on Au^{197}. If t is the elapsed time after irradiation, the population of the Hg^{195} ground state is given by

$$N = a_1 \left[e^{-\lambda_1 t} - e^{-\lambda_2 t}\right] + a_2 e^{-\lambda_2 t}$$

where λ_1 and λ_2 are the decay probabilities for the isomeric and ground states respectively and a_1 and a_2 are constants. Any gamma transition, γ_i, which follows only the electron capture decay of the Hg^{195} ground state will therefore have an intensity I_i which exhibits the same time dependence.

Thus $$I_i = K_i \left\{ a_1 (e^{-\lambda_1 t} - e^{-\lambda_2 t}) + a_2 e^{-\lambda_2 t} \right\} \qquad (1)$$

where K_i is a constant characteristic of the i'th gamma-ray. However the 40 hour isomeric state also has a substantial electron capture branching ratio direct to levels in Au^{195} and, as was pointed out in chapter III, the 262 keV level is populated substantially from both parent levels. If we let i = 1 refer to a particular gamma de-exciting the 262 keV level, its intensity (setting $K_1 = 1$) is given by

$$I_1 = a_1 (e^{-\lambda_1 t} - e^{-\lambda_2 t}) + a_2 e^{-\lambda_2 t} + a_3 e^{-\lambda_1 t} \qquad (2)$$

At $t = 0$, $I_1 = a_2 + a_3$ and the fraction of the intensity <u>at this time</u> due to population of the 262 keV level from the Hg^{195} ground state is just

$$R = \frac{a_2}{a_2 + a_3}$$

We can rewrite equation (2) as

$$I_1 = A_1 \, e^{-\lambda_1 t} + A_2 \, e^{-\lambda_2 t} \tag{3}$$

where

$$\left.\begin{aligned} A_1 &= a_1 + a_3 \\ A_2 &= a_2 - a_1 \end{aligned}\right\} \tag{4}$$

Let i = 2 refer to a gamma ray which follows the decay of the Hg^{195} ground state only (for example the 780 keV gamma ray). Then from (1)

$$I_2 = K_2 \, a_1 \, e^{-\lambda_1 t} + K_2 \, (a_2 - a_1) \, e^{-\lambda_2 t}$$

or

$$I_2 = B_1 \, e^{-\lambda_1 t} + B_2 \, e^{-\lambda_2 t} \tag{5}$$

where

$$\left.\begin{aligned} B_1 &= K_2 a_1 \\ B_2 &= K_2 (a_2 - a_1) \end{aligned}\right\} \tag{6}$$

Equations (4) and (6) can be solved to give

$$R = \frac{a_2}{a_2 + a_3} = \frac{1 + B_1/B_2}{1 + A_1/A_2}$$

The coefficients A_i and B_i i=1, 2 are obtained by a least squares fit of equations (3) and (5) to the experimentally measured line intensities I_1 and I_2 as a function of time. (λ_1 and λ_2 are of course known beforehand.) In fact, four timed runs were used for this purpose and t = 0 (which is of course arbitrary) was chosen to coincide with the first timed run. The calculations were performed or an IBM 360 computer and the results for the two known de-excitations of the 262 keV level are as follows.

I_1 = 262 keV I_2 = 780 keV R(t=0) = 0.140 $\pm$ 0.022

I_2 = 1111 keV R(t=0) = 0.138 $\pm$ 0.017

I_1 = 200 keV I_2 = 780 keV R(t=0) = 0.12 $\pm$ 0.15

As a check on the validity of the method R was also calculated for the 780 keV line. Since it follows the Hg^{195} ground state decay only we expect R = 1.000. The result of the computation was

I_1 = 780 keV I_2 = 1111 keV R(t=0) = 1.01 $\pm$ 0.20

These values of R are of course valid only for the first timed run and it is this spectrum which is used to calculate the normalized intensities shown in column 4 of table 3.2.

APPENDIX II

ANGULAR CORRELATION ANALYSIS

The method of analysis of angular correlation data presented here is due to D. H. White (reference 4, chapter I).

In the ideal geometry limit (point source and detectors subtending zero solid angle) the correlation function for two cascading gamma-rays may be written

$$W(\theta) = \sum_{n=0,2,\ldots}^{n_m} A_n P_n(\cos\theta)$$

where the P_n are Legendre polynomials. In the cascades considered in the present work $n_m \leq 4$ so, if A_0 is normalized to unity,

$$W(\theta) = 1 + A_2P_2(\cos\theta) + A_4P_4(\cos\theta)$$

A minimum of three coincidence measurements at three different angles are therefore sufficient to determine A_2 and A_4. The counting statistics, from an examination of the form of the Legendre polynomials, are usually optimum for the three angles $\theta = 90^\circ, 135^\circ, 180^\circ$. The coincidence counts at a given angle, correctly normalized to the singles rate at that angle and with background subtracted, can be written

$$C_\theta = \sum_{n=0,2,4} a_n P_n(\cos\theta) = \sum_n a_n P_{n\theta}$$

(The index θ denotes a discrete value of the angle) and inverting the matrix $P_{n\theta}$ we obtain

$$a_n = \sum_\theta P_{n\theta}^{-1}\, C_\theta$$

The experimental values of A_n are then given by

$$A_n = \frac{a_n}{a_0} \pm \frac{1}{a_0}\left\{ \sum_\theta C_\theta^{+} \left[P_{n\theta}^{-1} - P_{0\theta}^{-1}\left(\frac{a_n}{a_0}\right)\right]^2 \right\}^{\frac{1}{2}}$$

The quantity in braces is the statistical error. The expression C_θ^{+} refers to the normalized coincidence counts without background subtracted. After evaluating the matrix $P_{n\theta}^{-1}$, we obtain

$$A_2 = \frac{a_2}{a_0} \pm \frac{1}{105 a_0}\left[C_{90}^{+}\left(90 + 42\,\frac{a_2}{a_0}\right)^2 + C_{135}^{+}\left(40 - 56\,\frac{a_2}{a_0}\right)^2 + C_{180}^{+}\left(50 - 7\,\frac{a_2}{a_0}\right)^2 \right]^{\frac{1}{2}}$$

$$A_4 = \frac{a_4}{a_0} \pm \frac{1}{105 a_0}\left[C_{90}^{+}\left(48 - 42\,\frac{a_4}{a_0}\right)^2 + C_{135}^{+}\left(96 + 56\,\frac{a_4}{a_0}\right)^2 + C_{180}^{+}\left(48 - 7\,\frac{a_4}{a_0}\right)^2 \right]^{\frac{1}{2}}$$

where

$$a_0 = \frac{1}{105}\,(42\, C_{90} + 56\, C_{135} + 7\, C_{180})$$

$$a_2 = \frac{1}{105}\,(-90\, C_{90} + 40\, C_{135} + 50\, C_{180})$$

$$a_4 = \frac{1}{105}\,(48\, C_{90} - 96\, C_{135} + 48\, C_{180})$$

For the case of axially symmetric detectors (as used in these investigations) the measured values of A_n are attenuated by[1] $\frac{J_n[1]}{J_0[1]}\,\frac{J_n[2]}{J_0[2]}$ where the functions J_n depend upon the geometries of detectors 1 and 2 (i.e. the two detectors involved in the measurement of coincidences at a given angle). These quantities J_n/J_0 have been evaluated for several sizes of NaI and Ge(Li)

detectors. In this work the tabulations of Yates[2] were used for the NaI attenuation factor and those of Black et al.[3] for the Ge(Li) attenuation factor.

(Corrections for finite source size were not expected to be significant in the present work having regard to the small dimensions of sources used and so will not be discussed.) The correction term may be applied using the relation

$$A_n \text{ (corr.)} = A_n \text{ (meas.)} \Big/ \frac{J_n[1]}{J_0[1]} \; \frac{J_n[2]}{J_0[2]}$$

REFERENCES

1. M. E. Rose, Phys. Rev. 91, 610 (1953).

2. M. J. Yates, Perturbed Angular Correlations, in Alpha-, Beta-, and Gamma-Ray Spectroscopy P453, ed. K. Siegbahn, North Holland (1964).

3. J. L. Black and W. Gruhle, Nucl. Instr. and Meth. 46, 213 (1967).

APPENDIX III

EVALUATION OF $\langle J_c \| T^{(0)}(c) \| J_c \rangle$

Let $T^{(0)}(c)$ represent a scalar operator operating on the even-even core of an odd-A nucleus. According to the Wigner-Eckart theorem its diagonal matrix elements are given by

$$\langle J_c M_c | T^{(0)}(c) | J_c M_c \rangle = (-1)^{J_c - M_c} \begin{pmatrix} J_c & 0 & J_c \\ -M_c & 0 & M_c \end{pmatrix} \langle J_c \| T^{(0)}(c) \| J_c \rangle$$

$$= (2J_c+1)^{-\frac{1}{2}} \langle J_c \| T^{(0)}(c) \| J_c \rangle \qquad (1)$$

If the matrix element is independent of J_c we obtain equation (4) of chapter V, namely

$$\langle J_c \| T^{(0)}(c) \| J_c \rangle \sim (2J_c+1)^{\frac{1}{2}}$$

This is in fact the case if J_c arises from the coupling of the nucleons in one orbital only and if $T^{(0)}(c)$ may be expressed as a sum of single particle operators for the nucleons in the orbital, i.e.

$$|J_c M_c\rangle = |j_c^n \; J_c \; M_c\rangle \text{ , antisymmetric in the n nucleons.}$$

$$T^{(0)}(c) = \sum_{i=1}^{n} T_i^{(0)}(c)$$

n being the number of nucleons in the orbital, and j_c the angular momentum of the orbit in question. Since all the single particle operators $T_i^{(0)}(c)$ are equivalent and since the matrix element on the LHS of (1) involves the product of two antisymmetric wave functions, all the single particle operators contribute equally and we can write

$$\langle J_c M_c | T^{(0)}(c) | J_c M_c \rangle = n \langle j_c^n \; J_c \; M_c | T_n^{(0)}(c) | j^n \; J_c \; M_c \rangle \qquad (2)$$

We can now split off the n'th nucleon from the antisymmetrized wave function by making use of the coefficients of fractional parentage as defined by de Shalit and Talmi. (Nuclear Shell Theory, Academic Press, 1963, p. 273)

$$| j_c^n \; J_c \; M_c \rangle = \sum_{J_1} [j_c^{n-1} \; (J_1) \; j_{c_n} \; J_c | \} \; j_c^n \; J_c] | j_0^{n-1} J_1 j_{c_n} J_c \qquad (3)$$

where

$$| j_0^{n-1} \; J_1 \; j_{c_n} \; J_c M_c \rangle = \sum_{m_n M_1} (J_1 M_1 \; j_{c_n} \; m_n | J_c M_c) | j_c^{n-1} J_1 M_1 \rangle \; | j_{c_n} m_n \rangle \qquad (4)$$

Substitution of (3) into (2) yields

$$\langle J_c M_c | T^{(0)}(c) | J_c M_c \rangle$$

$$= n \sum_{J_1 J_1'} [j_c^{n-1} \; (J_1) j_{c_n} \; J_c | \} \; j_c^n \; J_c] [j_c^{n-1} (J_1') j_{c_n} \; J_c | \} \; j_c^n \; J_c]$$

$$\cdot \langle j_c^{n-1} \; J_1 \; j_{c_n} \; J_c M_c | T_n^{(0)}(c) | j_c^{n-1} \; J_1' \; j_{c_n} \; J_c M_c \rangle$$

If the expansion (4) is then substituted into this last equation, the orthogonality of the $| j_c^{n-1} \; J_1 M_1 \rangle$ introduces a $\delta_{J_1 J_1'} \cdot \delta_{M_1 M_1'}$ while the scalar nature of $T_n^{(0)}(c)$ introduces a $\delta_{m_n m_n'}$. The orthogonality properties of the coefficients of fractional parentage can then be used to obtain, finally,

$$\langle J_c M_c | T^{(0)}(c) | J_c M_c \rangle = n \langle j_{c_n} | T_n^{(0)}(c) | j_{c_n} \rangle$$

independent of J_c as required.

APPENDIX IV

SOME CORE EXCITATION MODEL CALCULATIONS FOR Au^{195}

To calculate the reduced M1 transition probability for the transition $|\tfrac{1}{2}\rangle \rightarrow |3/2\rangle_0$ we start with equation (5) on p. which becomes

$$\frac{T_{i\rightarrow f}}{\alpha_1 E^3} = \tfrac{1}{2} |\langle \tfrac{3}{2}\, 0 \| \Omega^{(1)} \| \tfrac{1}{2} \rangle|^2$$

where $$|\tfrac{3}{2}\rangle_0 = A\, |0\, \tfrac{3}{2}\, \tfrac{3}{2}\rangle + \sqrt{1-A^2}\; |2\, \tfrac{3}{2}\, \tfrac{3}{2}\rangle$$

$$|\tfrac{1}{2}\rangle = |2\, \tfrac{3}{2}\, \tfrac{1}{2}\rangle$$

Therefore

$$\langle \tfrac{3}{2}\, 0 \| \Omega^{(1)} \| \tfrac{1}{2}\rangle = A \langle 0\, \tfrac{3}{2}\, \tfrac{3}{2} \| \Omega^{(1)} \| 2\, \tfrac{3}{2}\, \tfrac{1}{2}\rangle + \sqrt{1-A^2}\, \langle 2\, \tfrac{3}{2}\, \tfrac{3}{2} \| \Omega^{(1)} \| 2\, \tfrac{3}{2}\, \tfrac{1}{2}\rangle$$

The first term is proportional to $\begin{Bmatrix} 0 & \frac{3}{2} & \frac{3}{2} \\ \frac{1}{2} & 2 & 1 \end{Bmatrix}$ as can be seen from equation (6) on p. 138 and hence vanishes identically. Also, from equation (6),

$$\langle 2\, \tfrac{3}{2}\, \tfrac{3}{2} \| \Omega^{(1)} \| 2\, \tfrac{3}{2}\, \tfrac{1}{2}\rangle = -2\sqrt{2} \left[\langle 2 \| \Omega^{(1)}(c) \| 2\rangle \begin{Bmatrix} 2 & \frac{3}{2} & \frac{3}{2} \\ \frac{1}{2} & 2 & 1 \end{Bmatrix} - \langle \tfrac{3}{2} \| \Omega^{(1)}(P) \| \tfrac{3}{2}\rangle \begin{Bmatrix} \frac{3}{2} & \frac{3}{2} & 2 \\ \frac{1}{2} & \frac{3}{2} & 1 \end{Bmatrix} \right]$$

The magnetic moment of a system in a state of angular momentum j is given by

$$\mu(j) = g\, j = \left[\frac{j}{(2j+1)(j+1)} \right]^{\frac{1}{2}} \langle j \| \Omega^{(1)} \| j \rangle$$

where g is the "g-factor" of the state. Thus

$$\langle 2 \| \Omega^{(1)}(c) \| 2 \rangle = \sqrt{30}\, g_c$$

$$\langle \tfrac{3}{2} \| \Omega^{(1)}(p) \| \tfrac{3}{2} \rangle = \sqrt{15}\, g_p$$

Using the identity $\begin{Bmatrix} \frac{3}{2} & \frac{3}{2} & 2 \\ \frac{1}{2} & \frac{3}{2} & 1 \end{Bmatrix} = \sqrt{2} \begin{Bmatrix} 2 & \frac{3}{2} & \frac{3}{2} \\ \frac{1}{2} & 2 & 1 \end{Bmatrix}$

we obtain

$$\langle 2\ \tfrac{3}{2}\ \tfrac{3}{2} \| \Omega^{(1)} \| 2\ \tfrac{3}{2}\ \tfrac{1}{2} \rangle = 4\sqrt{15} \begin{Bmatrix} 2 & \frac{3}{2} & \frac{3}{2} \\ \frac{1}{2} & 2 & 1 \end{Bmatrix} (g_p - g_c)$$

$$= -2\sqrt{\tfrac{3}{2}}\,(g_p - g_c)$$

Therefore $$\frac{T_{i\to f}(M1)}{\alpha_1 E^3} = 3(1-A^2)(g_c - g_p)^2 \qquad (1)$$

Consider now the magnetic moment of the ground state, $\mu(\frac{3}{2}^+)_0$. From equation (7) on p.139, $\mu(\frac{3}{2}^+)_0 = \langle \frac{3}{2}\ \frac{3}{2} | \Omega^{(1)}_0 | \frac{3}{2}\ \frac{3}{2} \rangle_0$

$$= \frac{2}{2\sqrt{15}} \langle \tfrac{3}{2} \| \Omega^{(1)} \| \tfrac{3}{2} \rangle_0$$

and the reduced matrix element is

$$A^2 \langle 0\ \tfrac{3}{2}\ \tfrac{3}{2} \| \Omega^{(1)} \| 0\ \tfrac{3}{2}\ \tfrac{3}{2} \rangle + A\sqrt{1-A^2} \Big[\langle 0\ \tfrac{3}{2}\ \tfrac{3}{2} \| \Omega^{(1)} \| 2\ \tfrac{3}{2}\ \tfrac{3}{2} \rangle + \langle 2\ \tfrac{3}{2}\ \tfrac{3}{2} \| \Omega^{(1)} \| 0\ \tfrac{3}{2}\ \tfrac{3}{2} \rangle$$

$$+ (1-A^2)\ \langle 2\ \tfrac{3}{2}\ \tfrac{3}{2} \| \Omega^{(1)} \| 2\ \tfrac{3}{2}\ \tfrac{3}{2} \rangle$$

The cross product terms are proportional to $\begin{Bmatrix} 0 & \frac{3}{2} & \frac{3}{2} \\ \frac{3}{2} & 2 & 1 \end{Bmatrix} = 0$

Also,

$$\langle 0\ \tfrac{3}{2}\ \tfrac{3}{2} \| \Omega^{(1)} \| 0\ \tfrac{3}{2}\ \tfrac{3}{2} \rangle = 4 \begin{Bmatrix} \frac{3}{2} & \frac{3}{2} & 1 \\ \frac{3}{2} & \frac{3}{2} & 0 \end{Bmatrix} \langle \tfrac{3}{2} \| \Omega^{(1)}(p) \| \tfrac{3}{2} \rangle$$

$$\langle 2\ \tfrac{3}{2}\ \tfrac{3}{2} \| \Omega^{(1)} \| 2\ \tfrac{3}{2}\ \tfrac{3}{2} \rangle = 4 \Big[\begin{Bmatrix} 2 & \frac{3}{2} & \frac{3}{2} \\ \frac{3}{2} & 2 & 1 \end{Bmatrix} \langle 2 \| \Omega^{(1)}(c) \| 2 \rangle$$

$$+ \begin{Bmatrix} \frac{3}{2} & \frac{3}{2} & 2 \\ \frac{3}{2} & \frac{3}{2} & 1 \end{Bmatrix} \langle \tfrac{3}{2} \| \Omega^{(1)}(p) \| \tfrac{3}{2} \rangle \Big]$$

Evaluating the 6j coefficients and replacing the reduced matrix elements by the corresponding g-factors we obtain, after some

algebra,

$$\mu(\tfrac{3}{2}^+)_0 = \tfrac{3}{2}\left[A^2 g_p + \tfrac{4}{5}(1-A^2)\, g_c + \tfrac{1}{5}(1-A^2)\, g_p\right]$$

which simplifies to

$$\mu(\tfrac{3}{2}^+)_0 = \tfrac{3}{2} g_p + \tfrac{6}{5}(1-A^2)(g_c - g_p) \qquad (2)$$

Let us next calculate reduced matrix elements for M1 and E2 transitions between the $\frac{3}{2}^+$ and $\frac{1}{2}^+$ members of the first core excitation multiplet. The wave functions are:

$$|i\rangle = |\tfrac{3}{2}\rangle_1 = A|2\ \tfrac{3}{2}\ \tfrac{3}{2}\rangle - \sqrt{1-A^2}\,|0\ \tfrac{3}{2}\ \tfrac{3}{2}\rangle$$

$$|f\rangle = |\tfrac{1}{2}\rangle = |2\ \tfrac{3}{2}\ \tfrac{1}{2}\rangle$$

For E2 transitions,

$$\langle f\|\Omega^{(2)}\|i\rangle = A\langle 2\ \tfrac{3}{2}\ \tfrac{1}{2}\|\Omega^{(2)}\|2\ \tfrac{3}{2}\ \tfrac{3}{2}\rangle - \sqrt{1-A^2}\langle 2\ \tfrac{3}{2}\ \tfrac{1}{2}\|\Omega^{(2)}\|0\ \tfrac{3}{2}\ \tfrac{3}{2}\rangle$$

$$= -2\sqrt{2}\, A\left[\begin{Bmatrix} 2 & 2 & 2 \\ \frac{3}{2} & \frac{1}{2} & \frac{3}{2} \end{Bmatrix}\langle 2\|\Omega^{(2)}(c)\|2\rangle - \begin{Bmatrix} \frac{3}{2} & \frac{3}{2} & 2 \\ \frac{3}{2} & \frac{1}{2} & 2 \end{Bmatrix}\langle \tfrac{3}{2}\|\Omega^{(2)}(p)\|\tfrac{3}{2}\rangle\right]$$

$$+ 2\sqrt{2}\sqrt{1-A^2}\begin{Bmatrix} 2 & 0 & 2 \\ \frac{3}{2} & \frac{1}{2} & \frac{3}{2} \end{Bmatrix}\langle 2\|\Omega^{(2)}(c)\|0\rangle$$

or,

$$\langle f\|\Omega^{(2)}\|i\rangle = -\tfrac{1}{5}A\left[\sqrt{7}\langle 2\|\Omega^{(2)}(c)\|2\rangle + \sqrt{2}\langle \tfrac{3}{2}\|\Omega^{(2)}(p)\|\tfrac{3}{2}\rangle\right] + \frac{\sqrt{10}}{5}\sqrt{1-A^2}\ \langle 2\|\Omega^{(2)}(c)\|0\rangle \qquad (3)$$

For M1 transitions,

$$\langle f\|\Omega^{(1)}\|i\rangle = A\langle 2\ \tfrac{3}{2}\ \tfrac{1}{2}\|\Omega^{(1)}\|2\ \tfrac{3}{2}\ \tfrac{3}{2}\rangle - \sqrt{1-A^2}\langle 2\ \tfrac{3}{2}\ \tfrac{1}{2}\|\Omega^{(1)}\|0\ \tfrac{3}{2}\ \tfrac{3}{2}\rangle$$

$$= 2\sqrt{2}\, A\left[\begin{Bmatrix} 2 & 2 & 1 \\ \frac{3}{2} & \frac{1}{2} & \frac{3}{2} \end{Bmatrix}\langle 2\|\Omega^{(1)}(c)\|2\rangle - \begin{Bmatrix} \frac{3}{2} & \frac{3}{2} & 1 \\ \frac{3}{2} & \frac{1}{2} & 2 \end{Bmatrix}\langle \tfrac{3}{2}\|\Omega^{(1)}(p)\|\tfrac{3}{2}\rangle\right]$$

or,

$$\langle f\|\Omega^{(1)}\|i\rangle = A\sqrt{6}\,(g_p - g_c) \qquad (4)$$

Equations (3) and (4) are used in the text to evaluate the

mixing ratio of the 180 keV transition.

Now we shall calculate reduced matrix elements for E2 transitions from the $\frac{5}{2}^+$ member of the first core excitation multiplet to the $\frac{1}{2}^+$ member and to the ground state. For the former,

$$|i\rangle = |2\ \tfrac{3}{2}\ \tfrac{5}{2}\rangle$$

$$|f\rangle = |2\ \tfrac{3}{2}\ \tfrac{1}{2}\rangle$$

Therefore

$$\langle f\|\Omega^{(2)}\|i\rangle = 2\sqrt{3}\left[\begin{Bmatrix} 2 & 2 & 2 \\ \frac{5}{2} & \frac{1}{2} & \frac{3}{2} \end{Bmatrix}\langle 2\|\Omega^{(2)}(c)\|2\rangle + \begin{Bmatrix} \frac{3}{2} & \frac{3}{2} & 2 \\ \frac{5}{2} & \frac{1}{2} & 2 \end{Bmatrix}\langle \tfrac{3}{2}\|\Omega^{(2)}(p)\|\tfrac{3}{2}\rangle\right]$$

or,

$$\langle f\|\Omega^{(2)}\|i\rangle = \frac{\sqrt{3}}{5}\left[\langle 2\|\Omega^{(2)}(c)\|2\rangle + \sqrt{\frac{7}{2}}\langle \tfrac{3}{2}\|\Omega^{(2)}(p)\|\tfrac{3}{2}\rangle\right] \qquad (5)$$

and, for the latter,

$$|i\rangle = |2\ \tfrac{3}{2}\ \tfrac{5}{2}\rangle$$

$$|f\rangle = A|0\ \tfrac{3}{2}\ \tfrac{3}{2}\rangle + \sqrt{1-A^2}\ |2\ \tfrac{3}{2}\ \tfrac{3}{2}\rangle$$

Therefore

$$\langle f\|\Omega^{(2)}\|i\rangle = A2\sqrt{6}\begin{Bmatrix} 0 & 2 & 2 \\ \frac{5}{2} & \frac{3}{2} & \frac{3}{2} \end{Bmatrix}\langle 0\|\Omega^{(2)}(c)\|2\rangle$$
$$+\sqrt{1-A^2}\ 2\sqrt{6}\left[\begin{Bmatrix} 2 & 2 & 2 \\ \frac{5}{2} & \frac{3}{2} & \frac{3}{2} \end{Bmatrix}\langle 2\|\Omega^{(2)}(c)\|2\rangle - \begin{Bmatrix} \frac{3}{2} & \frac{3}{2} & 2 \\ \frac{5}{2} & \frac{3}{2} & 2 \end{Bmatrix}\langle \tfrac{3}{2}\|\Omega^{(2)}(p)\|\tfrac{3}{2}\rangle\right]$$

or,

$$\langle f\|\Omega^{(2)}\|i\rangle = \sqrt{\frac{6}{5}}\,A\langle 0\|\Omega^{(2)}(c)\|2\rangle + \sqrt{6}\sqrt{1-A^2}\left[\frac{1}{5}\langle \tfrac{3}{2}\|\Omega^{(2)}(p)\|\tfrac{3}{2}\rangle - \frac{1}{\sqrt{14}}\langle 2\|\Omega^{(2)}(c)\|2\rangle\right] \qquad (6)$$

Finally we present a sample calculation of reduced M1 matrix elements involving the 842 keV state wave functions

(p. 154 in text). Consider the M1 reduced amplitude $\langle f \| \Omega^{(1)} \| i \rangle$ for the ground state decay.

$$|i\rangle = B|0\ \tfrac{1}{2}\ \tfrac{1}{2}\rangle + \sqrt{1-B^2}\,|2^*\ \tfrac{3}{2}\ \tfrac{1}{2}\rangle$$

$$|f\rangle = A|0\ \tfrac{3}{2}\ \tfrac{3}{2}\rangle + \sqrt{1-A^2}\,|2\ \ \tfrac{3}{2}\ \tfrac{3}{2}\rangle$$

The cross product terms in $\langle f \| \Omega^{(1)} \| i \rangle$ vanish identically from equation (6) p. 138. The term in AB is proportional to the matrix element $\langle \tfrac{3}{2} \| \Omega^{(1)}(p) \| \tfrac{1}{2} \rangle$ which must also vanish identically. This can be seen by noting that the single particle state is meant to designate a $d_{\frac{3}{2}}$ proton and hence is more fully written

$$|l\ s\ j\rangle = |2\ \tfrac{1}{2}\ \tfrac{3}{2}\rangle$$

Similarly $|\tfrac{1}{2}\rangle$ represents an $s_{\frac{1}{2}}$ proton and should be written

$$|l\ s\ j\rangle = |0\ \tfrac{1}{2}\ \tfrac{1}{2}\rangle$$

Thus $\langle \tfrac{3}{2} \| \Omega^{(1)}(p) \| \tfrac{1}{2} \rangle = \langle 2\ \tfrac{1}{2}\ \tfrac{3}{2} \| \Omega^{(1)}(p) \| 0\ \tfrac{1}{2}\ \tfrac{1}{2} \rangle$

The magnetic dipole operator for the proton, in units of the nuclear magneton, is just

$$\Omega^{(1)}(p) = \underline{l} + g_s\, \underline{s}$$

where g_s is the proton's gyromagnetic ratio. But $\langle l = 2\ \tfrac{1}{2}\ \tfrac{3}{2} \| \underline{l} \| l = 0\ \tfrac{1}{2}\ \tfrac{1}{2} \rangle \equiv 0$ since a vector operator cannot connect states differing by two units of angular momentum. The algebra of irreducible tensors likewise requires that $\langle 2\ \tfrac{1}{2}\ \tfrac{3}{2} \| \underline{s} \| 0\ \tfrac{1}{2}\ \tfrac{1}{2} \rangle \equiv 0$ (see de Shalit and Talmi, Nuclear Shell Theory, p. 134). The only non vanishing term in the matrix element is thus

$$2\sqrt{2}\sqrt{1-A^2}\sqrt{1-B^2}\left[-\begin{Bmatrix} 2 & 2 & 1 \\ \frac{1}{2} & \frac{3}{2} & \frac{3}{2} \end{Bmatrix}\langle 2\|\Omega^{(1)}(c)\|2^*\rangle + \begin{Bmatrix} \frac{3}{2} & \frac{3}{2} & 1 \\ \frac{1}{2} & \frac{3}{2} & 2 \end{Bmatrix}\langle \tfrac{3}{2}\|\Omega^{(1)}(p)\|\tfrac{3}{2}\rangle\right]$$

or,

$$\langle f\|\Omega^{(1)}\|i\rangle = \sqrt{2(1-A^2)(1-B^2)}\left[\frac{1}{\sqrt{10}}\langle 2\|\Omega^{(1)}(c)\|2^*\rangle - \sqrt{3}\, g_p\right] \quad (7)$$

Other M1 transition amplitudes are calculated similarly.